

**Use of Nanoscale Magnetic Ferrites as
Components of Plasmonic Sensors for SERS
Detection of Persistent Organic Pollutants**

by

© Stephanie M. V. Gallant

A Dissertation submitted to the School of Graduate Studies in partial fulfillment of
the requirements for the degree of

Doctor of Philosophy

Department of Chemistry

Memorial University of Newfoundland

December 2021

St. John's

Newfoundland

Abstract

This thesis studies the use of magnetic nanoparticles (NPs) as key-components of a new class of surface-enhanced Raman spectroscopy (SERS) sensors, with the overall goal being the development of sensors for environmental polyaromatic hydrocarbon (PAH) monitoring. As SERS relies on electromagnetic field enhancement, magnetic NPs are a core class of materials which are currently under-utilized in this field, with the vast majority of reports only using them as a moveable handle. As their contribution to SERS enhancement has been thus-far negated, this work aims to study them as the main plasmonic contributor of the surface.

A patterned magnetic surface was developed using an external field to create a heirarchical multilayer, where one version uses classic iron oxide NPs (IONPs), and another uses cobalt ferrite NPs (CFNPs). The patterned IONP surface has signal-to-noise ratios of 3 dB, exhibiting excellent signal and also longevity, as IONPs are capped with an inert layer. Analogous CFNPs are synthesized to understand how differing magnetic properties and geometries could change sensor performance. CFNPs are synthesized at different reaction scales, resulting in variation of magnetic parameters and particle geometries, which is correlated with differing performance of the surface once integrated into a sensor. The highest-performing CFNP sensor has signal-to-noise ratios (SNRs) of 4.5 dB, and additionally, the substrates are reusable.

As these first versions of magnetic NP surfaces prove very useful in plasmonic

applications, this work paves the way to further explore use of magnetic materials for sensing.

Acknowledgements

There are many people whose support, in many forms, allowed me to complete this long journey. Without them, I would simply not be where I am at this moment.

To my supervisor, Erika

Firstly, a big thank you for taking a chance on me as an undergraduate student with questionable grades, but a fiery curiosity. You've taught me that hard science and compassion don't have to be mutually exclusive, and that there is a bigger picture to every seemingly-small thing we do. You've allowed me the opportunity to become a passionate researcher and leader, and for this I will always be grateful.

To my parents, Andy and Lina: Immense and eternal thanks for all you've sacrificed and fostered throughout my life to help me achieve. From you, I've learned to be a planner, a helper, and to persist. You have never doubted my capabilities in any moment, even when I have myself. "Thank you" barely begins to cover the gravity of my gratefulness.

Especialmente para minha Mãe: obrigada por tudo, e por sempre acreditar em mim.

To all of my friends, new and old:

If you have lent an ear to my grad school complaints, enjoyed time with me outside of academia, encouraged me when I felt defeated, and celebrated my wins along the

way... I am so lucky to have you! You know who you are. I love you all forever.

Special shout-out to Silvana, Kathryn, and Juliana - my kindred chem ladies who always understand this wild grad school journey (and then some). Truly would have suffered through much worse without you.

To the chemistry faculty and staff, whom I have learned from and worked alongside since 2013: It has been a pleasure! Additional thanks to Mary, Ros, and Debbie for taking such great care of us with special efforts along the way.

Additional thanks: I would like to thank the funding sources which allowed me to complete this research, including the Natural Sciences and Engineering Research Council (NSERC), Canada Foundation for Innovation (CFI), and Memorial University's School of Graduate Studies (SGS). Additionally, I would like to thank Dr. Liqin Chen for his gift to the Department of Chemistry, whose scholarships allowed for more comfortable living for so many of us in recent years.

Table of Contents

| | |
|--|-------------|
| Abstract | ii |
| Acknowledgments | iv |
| List of Tables | xi |
| List of Figures | xxi |
| List of Abbreviations and Symbols | xxii |
| 1 Introduction | 1 |
| 1.1 Sensing: Motivation | 1 |
| 1.2 SERS in sensing | 4 |
| 1.2.1 Plasmonic materials | 5 |
| 1.2.2 SERS Challenges | 6 |
| 1.3 Nanostructures: Bottom-up and Top-down Fabrication Methods . . . | 7 |
| 1.3.1 Nanoparticles | 7 |
| 1.4 Magnetic nanoparticles and their applications | 9 |
| 1.5 Summary of the thesis | 12 |
| Co-authorship Statement | 31 |

| | | |
|----------|---|-----------|
| 2 | Hierarchical magnetic films for high-performing plasmonic sensors | 33 |
| 2.1 | Introduction | 34 |
| 2.2 | Experimental | 36 |
| 2.2.1 | Materials | 36 |
| 2.2.2 | Iron Oxide Nanoparticle Synthesis | 36 |
| 2.2.3 | Substrate Fabrication Method | 37 |
| 2.2.4 | Characterization | 40 |
| 2.2.5 | Substrate Testing Method | 40 |
| 2.3 | Results and Discussion | 41 |
| 2.3.1 | Determining Properties of Synthesized Nanoparticles | 41 |
| 2.3.2 | Sensor Design Focused on Magnetic Films | 44 |
| 2.4 | Conclusions | 49 |
| 2.5 | Acknowledgement | 49 |
| 3 | Substrate with Magnetic Layer for SERS, Methods for their Preparation and Uses Thereof | 56 |
| 3.1 | Description | 57 |
| 3.1.1 | Cross-reference to related applications | 57 |
| 3.1.2 | Background | 57 |
| 3.1.3 | Summary | 59 |
| 3.2 | Brief Description of the Drawings | 60 |
| 3.3 | Detailed Description | 62 |
| 3.3.1 | Definitions | 62 |
| 3.3.2 | SERS Substrates and Methods for the Preparation Thereof | 64 |
| 3.3.3 | Uses and Methods for Detecting an Analyte | 71 |
| 3.4 | Examples | 78 |

| | | |
|----------|--|------------|
| 3.4.1 | Example 1: General preparation of SERS substrates with organosilane capacitated ferrimagnetic iron nanoparticles (FeNPs) | 78 |
| 3.4.2 | Example 2: General preparation of SERS substrates with uncapped ferrimagnetic cobalt iron oxide nanoparticles (CoFeNPs) | 82 |
| 3.4.3 | Example 3: Detection of organic compounds using SERS substrates | 84 |
| 3.5 | Claims | 90 |
| 4 | Powerful electromagnetic field enhancement via complex cobalt ferrite surfaces for plasmonic sensing | 95 |
| 4.1 | Abstract | 95 |
| 4.2 | Communication | 96 |
| 4.3 | Acknowledgement | 103 |
| 4.4 | Conflicts of interest | 103 |
| 5 | Scaling the synthesis of cobalt ferrite nanoparticles resulting in differing properties: a SERS study | 107 |
| 5.1 | Introduction | 108 |
| 5.2 | Experimental | 109 |
| 5.2.1 | Materials | 109 |
| 5.2.2 | Nanoparticle Synthesis | 110 |
| 5.2.3 | Characterization | 111 |
| 5.2.4 | Substrate Fabrication Method | 111 |
| 5.2.5 | Substrate Testing Method | 112 |
| 5.2.6 | Substrate Washing Method | 112 |

| | | |
|----------|--|------------|
| 5.3 | Results | 113 |
| 5.3.1 | Characterization of Particles | 113 |
| 5.3.2 | Altering synthesis parameters beyond scale | 126 |
| 5.3.3 | Sensor design | 126 |
| 5.3.4 | Sensor performance | 126 |
| 5.3.5 | Magnetic field application during spectral acquisition | 130 |
| 5.4 | Conclusions | 134 |
| 5.5 | Acknowledgement | 135 |
| 6 | Conclusions and Future Directions | 141 |
| 6.1 | Conclusions of reported works | 141 |
| 6.2 | Future directions | 142 |
| A | Supplementary information for Hierarchical magnetic films for high- | |
| | performing plasmonic sensors | 145 |
| A.1 | Energy-dispersive X-ray (EDX) data | 145 |
| A.2 | Sizing via Dynamic Light Scattering (DLS) | 146 |
| A.3 | Atomic Force Microscopy data | 146 |
| A.4 | Supplementary Raman data | 147 |
| A.5 | Signal-to-Noise (SNR) Calculations | 148 |
| A.6 | Produced Water sampling | 149 |
| A.7 | Gas Chromatography-Mass Spectrometry (GC-MS) procedure | 150 |
| A.7.1 | Organic Extraction of Produced Water | 150 |
| A.7.2 | Dispersive Liquid-Liquid Microextraction (DLLME) | 151 |
| A.7.3 | GC-MS Analysis | 151 |
| A.8 | GCMS results | 151 |

| | | |
|----------|---|------------|
| B | MPTMS Capping Experiments | 160 |
| C | Supplementary information for Powerful electromagnetic field enhancement via complex cobalt ferrite surfaces for plasmonic sensing | 165 |
| C.1 | Archival use and Reusability | 165 |
| C.2 | Experimental Details | 168 |
| C.2.1 | Materials | 168 |
| C.2.2 | Nanoparticle Synthesis | 168 |
| C.2.3 | Characterization | 169 |
| C.2.4 | Substrate Fabrication Method | 169 |
| C.2.5 | Substrate Testing Method | 170 |
| C.2.6 | Area of Surface Measured via Raman Spectroscopy | 170 |

List of Tables

| | | |
|-----|--|-----|
| 5.1 | Comparison of CFNP products produced in different reaction scales, as studied via SEM. Shapes include spheres (S), octahedra (O), and disks (D). The smallest particles are nanospheres (NS), which are present in all samples. | 114 |
| 5.2 | Raman modes of CFNPs synthesized at different reaction scales, showing shifting of peak position which trend with scale. | 115 |
| 5.3 | The (400) and (440) peaks for this cubic structure were used to calculate distance, d , and lattice parameter, a , for the various scaled CF products. As the NP synthesis is scaled down, d and a both increase, which may be due to metal ion occupancy changes in the crystal, as Fe_3^+ has a larger radius than that of Co^{2+} | 118 |
| 5.4 | Magnetic parameters for each CFNP synthesis, showing changes in saturation, coercivity, remanence, and squareness as the reaction is scaled. | 122 |
| A.1 | GC-MS data for produced water, sampled from an offshore oil platform. | 152 |

List of Figures

| | | |
|-----|---|----|
| 1.1 | Some PAH parent structures: (a) naphthalene, (b) phenanthrene, (c) anthracene, (d) pyrene, (e) chrysene. | 2 |
| 1.2 | An illustration showing top-down and bottom-up approaches to nanofabrication. | 8 |
| 1.3 | Simplified schematic of an inverse spinel crystal structure, showing the tetrahedral and octahedral metal sites, along with the oxygen occupancy. | 10 |
| 2.1 | A novel plasmonic surface utilizing patterned multi-layers of magnetic nanoparticles as the forefront enhancement material for SERS | 34 |
| 2.2 | Photos of (a) bulk NPs showing their dark brown-black colour, easily distinguishable from red hematite, (b) Suspension of NPs, (c) NPs being collected with a magnet. (d) Near-finished substrate, with the solvent evaporating from the last NP layer addition, resting on the magnet used for patterning. | 37 |

| | | |
|-----|---|----|
| 2.3 | Schematic showing components of the working substrate. Starting with (a) roughly sputtered gold on glass in, this layer is then annealed (b) to allow for a more uniform layer. Once the gold is prepared, (c) magnetic NPs in solution are added with a magnet below the glass to control the particles, resulting in patterning of the dried layers which follow the magnetic field lines of the external magnet. (d) Successive layers are built up, and additions are repeated until a sufficient number of layers have been added. | 38 |
| 2.4 | Stitched optical microscope images taken at 20x across the patterned surface, showing the NP pattern that formed under the influence of an external magnetic field and remains once the field is removed. (Multiple scale bars digitally removed and replaced with single set.) | 39 |
| 2.5 | SEM images of (a-c) as-synthesized iron oxide NPs and (d-f) APTES-capped NPs. As seen in (a), (b), (d) and (e), the particle sizes and shapes are consistent across each sample. The higher magnification in (c) and (f) show a size range of 30-60 nm for both capped and uncapped NPs. | 41 |
| 2.6 | X-ray diffraction patterns for (a) as-synthesized iron oxide NPs and (b) APTES-capped NPs confirm the expected cubic inverse spinel crystal structure. A comparison of (a) and (b) shows that the silane coating does not alter the structure of the NPs. | 42 |

| | | |
|-----|--|----|
| 2.7 | Raman spectra highlighting the importance of the composite substrate including hierarchically patterned NPs, through a series of control experiments. The 5 nm annealed gold layer in (a), as well as that same layer exposed to 1 ppm of analyte (b), show significant fluorescence in their spectra. Spectra (c-e) all show nanoparticle peaks dominating for each case: unpatterned nanoparticles on a blank glass surface (c), patterned nanoparticles on glass (no gold) exposed to analyte (d), and non-patterned NPs on top of annealed gold exposed to analyte (e). Spectrum (f) shows a successful and strong enhancement of analyte on the working substrate, with magnetically patterned NP multi-layers on top of annealed gold. | 44 |
| 2.8 | Magnetic character shown via VSM hysteresis loops for (a) as-synthesized plain NPs and (b) APTES-capped NPs. Capped NPs show a slight drop in saturation magnetization from the plain NPs, but both exhibit comparable magnetic coercivity and remanence (inset). | 45 |
| 3.1 | Schematic of an exemplary embodiment of a SERS substrate of the present application in use with a Raman spectrometer. | 73 |
| 3.2 | Schematic of an exemplary embodiment of a method for detecting an analyte in a sample of the present application comprising submerging at least a portion of a SERS substrate of the present application in the sample. | 74 |
| 3.3 | Schematic of an exemplary embodiment of a method for detecting an analyte in a sample of the present application comprising depositing at least a portion of the sample onto a SERS substrate of the present application. | 75 |

| | | |
|-----|--|----|
| 3.4 | Raman spectra of a substrate with increasing layers of iron oxide nanoparticles deposited thereon (from top to bottom: 60, 80, 100, 120, 140, 160, 180, 200, 220 and 240 μL of iron oxide nanoparticle suspension added) according to embodiments of the present application. | 82 |
| 3.5 | SERS spectra obtained of a 1 ppm phenanthrene solution from five different spots of a SERS substrate that it was deposited on according to an embodiment of the present application. | 85 |
| 3.6 | SERS spectra obtained using a SERS substrate according to an embodiment of the present application pre-exposure (***) and post-exposure (****) to offshore oil produced water in comparison to a blank (*) and exposure to a 1 ppm phenanthrene solution (**). | 86 |
| 3.7 | SERS spectra of two SERS substrates prepared according to embodiments of the present application using 160 μL (*) and 140 pL iron oxide nanoparticles (***) exposed to 1 ppm phenanthrene, compared to a Raman spectrum of bulk (solid) phenanthrene (****). | 87 |
| 3.8 | SERS spectra obtained using a SERS substrate according to an embodiment of the present application pre-exposure and post-exposure (*) to a 1 ppm phenanthrene solution. | 89 |
| 3.9 | SERS spectra obtained of a 1 ppm phenanthrene solution from four different spots of a SERS substrate that it was deposited on according to an embodiment of the present application. | 89 |
| 4.1 | Nanoscale cobalt ferrite crystals, as synthesized via coprecipitation. The one-pot method at this reaction scale results in a mixture of particle shapes: nanospheres with a diameter around 45 nm, octahedra ranging from 100-500 nm, and a small number of disks around 100-300 nm. | 96 |

| | | |
|-----|--|-----|
| 4.2 | Diffraction patterns of cobalt ferrite nanoparticles synthesised by coprecipitation, showing the expected inverse spinel profile. Asterisks denote minor hematite ($\alpha\text{-Fe}_2\text{O}_3$) impurity. | 98 |
| 4.3 | VSM curve for cobalt ferrite nanoparticles. The cobalt ferrites have a H_C value of 2 kOe, meaning the NPs behave as permanent magnets. | 99 |
| 4.4 | Stitched optical images at x5 of the fabricated substrate surface, showing the magnetic patterning of the cobalt ferrite layers. | 99 |
| 4.5 | Raman enhancement of 1 ppm phenanthrene on substrate surface with patterned NP layers. Spectrum (a) shows the modes of solid phenanthrene crystals. In the exposed spectrum (c), the broad peak at 460 cm^{-1} can be attributed to the strong T_{1g} mode of cobalt ferrite also present in (b), showing Raman modes of the substrate itself before exposure to analyte, while the remainder of peaks in (c) are the result of analyte enhancement on the surface. ¹⁴ The spectra are offset for clarity but are all on the same scale. | 100 |
| 4.6 | Raman enhancement of 1 ppb of phenanthrene on patterned CF surface. For areas of surface where sensing is a challenge (a), an external magnetic field applied during acquisition greatly boosts the signal of the analyte (b). | 102 |
| 5.1 | Scanning electron microscope images of as-synthesized (post-annealing) cobalt ferrite crystals. (a-b) show crystals from a 100%-scale reaction performed at the standard $90\text{ }^\circ\text{C}$, while (c-d) show crystals for the same scale where the reaction was performed at $45\text{ }^\circ\text{C}$. (e-f) show crystals from a 25%-scale reaction, and (g-h) show crystals from a 12%-scale reaction, both synthesized at $90\text{ }^\circ\text{C}$ | 115 |

| | | |
|-----|---|-----|
| 5.2 | Proposed growth mechanism for the observed CFNP morphologies. Octahedra form as the stable (111) face grows from a disk, which result from the agglomeration and combining of nanospheres. | 116 |
| 5.3 | X-ray diffraction peaks for CF products. (a) 100%-scale synthesized at 90 °C (b) 100%-scale synthesized at 45 °C (c) 25%-scale (d) 12%-scale. α markers denote peaks corresponding to hematite impurities. | 117 |
| 5.4 | Part (A): Raman spectra of bulk CF crystals (a) 100%-scale synthesized at 90 °C (b) 100%-scale synthesized at 45 °C (c) 25%-scale (d) 12%-scale. Part (B): Ratios of Raman peak areas for ν_4 and ν_6 compared with ν_7 (roughly 470 cm^{-1} , 620 cm^{-1} , and 670 cm^{-1} , respectively) as synthesis reaction scale changes. Peak area values are averaged over triplicate data-sets, with peaks fit to a Gaussian. | 119 |
| 5.5 | Raman peak analysis for CFNPs showing shifting of peaks with decreasing reaction scale. The E_g mode (A) remains largely the same throughout the scales, with a net difference of 3 cm^{-1} . The T_{2g} mode (B) shifts to a higher wavenumber as reaction scale is decreased, while the two A_{1g} modes (C) shift to lower wavenumbers as scale is decreased. | 120 |
| 5.6 | (A): Raman spectra of CF crystals before (precursor product) and after annealing for 100%-scale at 45 °C and 25%-scale. (B): Corresponding XRD data for products before and after annealing. | 121 |
| 5.7 | Magnetic hysteresis curves for CF crystals synthesized at 100%-scale at both 90 °C and 45 °C, 25%-scale, and 12%-scale. The saturation values for each sample are listed in the inset. | 123 |

| | | |
|------|---|-----|
| 5.8 | Simulated VSM curves for an inverse spinel (NiFe_2O_4) with nanoscale particle size, showing resultant curves for single-domain particles (top) versus multi-domain (bottom). Reprinted from <i>Journal of Magnetism and Magnetic Materials</i> , R. H. Kodama, “Magnetic Nanopartifcles”, 200, 359-372, (1999), with permission from Elsevier. | 124 |
| 5.9 | Separation of Au film and CFNPs, showing how each behave under testing conditions of the working sensor. Annealed Au is shown as a blank and exposed layer, while the same is done for CFNPs (both patterned and a non-patterned equivalent), all of which display glass fluorescence or NP signal and no visible enhancement of the loaded 1 ppm phenanthrene. When all components are combined (top spectrum), enhancement of the analyte is successful (spectrum scaled down 0.5x) | 127 |
| 5.10 | SERS spectra collected from various locations across a substrate, exposed to 1 ppm of phenanthrene. Signal is consistent and strong at all points on the surface, with no preferential location. | 128 |
| 5.11 | Optical images stitched together, showing the patterning across the surface of a finished substrate. Sensing differences at locations (a) or (b) are negligible, indicating there is no preferential spot for spectral acquisition. | 128 |
| 5.12 | SERS performance of substrates made with the various scales of CFNPs, exposed to phenanthrene. Both the 1 ppm (left) and 1 ppb (right) tests show differences in SERS enhancement between the various synthesis products, where the 100%-scale crystals provide the best enhancing environment for each concentration of PAH tested. | 129 |

| | | |
|------|--|-----|
| 5.13 | Raman spectra showing the effects of applying a magnetic field during spectral acquisition. The bottom spectrum shows un-assisted SERS enhancement of 1 ppb phenanthrene on a sensor made with 100%-scale CFNPs, while the top spectrum shows enhancement from the same substrate with a magnet applied to the underside of the sensing substrate during collection. | 131 |
| 5.14 | When comparing resulting SNRs against magnetic characteristics M_R , M_S , and H_C of the CFNP particles, no trends in the data are apparent. Given the associated error bars for each calculated SNR value, it is clear that more data is required before anything conclusive could be said. | 132 |
| 5.15 | Comparison of freshly-exposed CFNP substrate (1 ppm phenanthrene; top) to the same surface checked one year later (2nd from top), showing surface activity which compares to a fresh exposure. The second last spectrum shows the one-year-later exposed substrate after washing with toluene (x3), showing removal of all detectable analyte. | 133 |
| A.1 | EDX spectroscopy confirms removal of counter ions and the presence of iron oxides. | 145 |
| A.2 | Atomic force micrographs of the surface of a freshly-deposited ~ 5 nm gold layer (left), created via magnetron sputtering, and a gold layer after annealing (right). The surface is initially largely smooth (the large spikes are noise associated with Au deposits 50-100 nm in height). After annealing, in preparation for use in the sensor design, the sputtered gold layer has become roughened. | 146 |
| A.3 | Spectra acquired after each successive nanoparticle layer addition of $20 \mu\text{L}$, showing fluorescence being quenched with sufficient layers. . . | 147 |

| | | |
|-----|--|-----|
| A.4 | Spectra acquired when focused within the nanoparticle multi-layer (top) allows for excellent enhancement of the analyte, while focusing on the reflective gold surface (bottom) largely results in fluorescence with very few enhancement peaks. | 147 |
| A.5 | Spectra acquired from different surface locations on patterned substrates show reproducible Raman signals and intensities from the exposed analyte | 148 |
| A.6 | The spectrum in (a) shows the Raman modes for ferrimagnetic $\text{Fe}_3\text{O}_4/\gamma\text{-Fe}_2\text{O}_3$, as per a freshly patterned substrate. Spectrum (b) shows the same surface after 4 years of slow oxidizing under ambient storage conditions, after being freshly exposed to analyte. The iron oxide form has changed to an oxy-hydroxide, $\gamma\text{-FeO(OH)}$, and these are the only modes visible in the spectrum. No analyte peaks are detectable. | 149 |
| B.1 | Substrate 8-2 made with patterned IONP@MPTMS exhibits significant enhancement of 1 ppm phenanthrene. | 161 |
| B.2 | Substrate 8-2 (different sensing spot from above figure) again displaying significant enhancement of 1 ppm phenanthrene. | 161 |
| B.3 | Comparison of sensors made with MPTMS-coated IONPs compared to the APTES-coated equivalent. Major peaks of phenanthrene on the surfaces remain consistent, exhibiting strong enhancement throughout. | 162 |
| B.4 | Sequential laser exposures (15 second acquisition, followed by 30 s and 15 s again) results in changes of the IONP@MPTMS sensing surface, exposed to 1 ppm phenanthrene. | 162 |
| B.5 | Sequential laser exposures (45 second acquisition, followed by 90 s and 45 s again) results in changes of the IONP@MPTMS sensing surface, exposed to 1 ppm phenanthrene. | 163 |

| | | |
|-----|---|-----|
| B.6 | Scanning across the patterned surface (middle to edge) shows comparable enhancement at all locations. | 163 |
| B.7 | Increasing laser exposure time before spectrum acquisition results in increasing amounts of activity on the surface, seemingly as a result of laser power. The square gaps in the 120 s spectrum (purple, top) are due to photon saturation of the detector. | 164 |
| B.8 | Increasing the laser exposure time results in irreversible changes of the surface, exposed to 1 ppm of phenanthrene. | 164 |
| C.1 | Raman spectra were collected from a 1-year stored substrate, comparing with the original spectrum aquired from the same surface when freshly exposed (top two lines). As there was comparable enhancement in both, this indicates that the substrate can be relied on for long periods of time for archival usage. Regarding potential reusability, ethanol and toluene were used as washing solvents to remove all presence of analyte. While all use of ethanol was unsuccessful, toluene in an active spray onto the surface successfully removed all analyte, making the substrate reusable for at least one cycle. | 167 |
| C.2 | Overlay of laser spot size (red dashed oval) on an optical micrograph of the SERS surface, showing the area encompassed when collecting Raman data. | 171 |

List of Abbreviations and Symbols

| | |
|-----------|--|
| CFNP | Cobalt ferrite nanoparticle |
| EF | Enhancement factor |
| EM | Electromagnetic |
| IONP | Iron oxide nanoparticle |
| IR; FT-IR | Infrared spectroscopy; Fourier-transform infrared spectroscopy |
| LOD | Limit of detection |
| MW | Molecular weight |
| NFNP | Nickel ferrite nanoparticle |
| NP | Nanoparticle |
| PAH | Polycyclic aromatic hydrocarbon |
| POP | Persistent organic pollutant |
| PW | Produced water |
| SEM | Scanning electron microscopy |
| SERS | Surface enhanced Raman spectroscopy |
| SNR | Signal-to-noise ratio |
| XRD | X-ray diffraction |

Chapter 1

Introduction

1.1 Sensing: Motivation

From initial drilling to functional burning, all oil & gas activities result in significant quantities of hydrocarbons being released into our oceans and the atmosphere. The impacts of such oil-based pollution are of great concern to both marine and terrestrial environments, resulting in negative outcomes for a variety of organisms. Acute impacts of large spills and other polluting events are often quite evident, leading to immediate mortality and visible spillage.¹ On the contrary, the persistently slow-acting nature of dilute, but highly stable, compounds are less obvious.

One large class of such compounds are polycyclic aromatic hydrocarbons (PAHs), which comprise of multi-ringed, conjugated carbon-based structures. These hydrophobic hydrocarbons are readily found in our environment,² where the most significant amounts can be directly attributed to human activity (pyrogenic and petrogenic sources).^{1,3-5} Lower molecular weight (MW) PAHs (2-3 rings; Figure 1.1 (a-c)) are more associated with processing of petroleum materials, while higher MW PAHs (4+ rings; Figure 1.1 (d & e)) are mostly derived from combustion.⁶

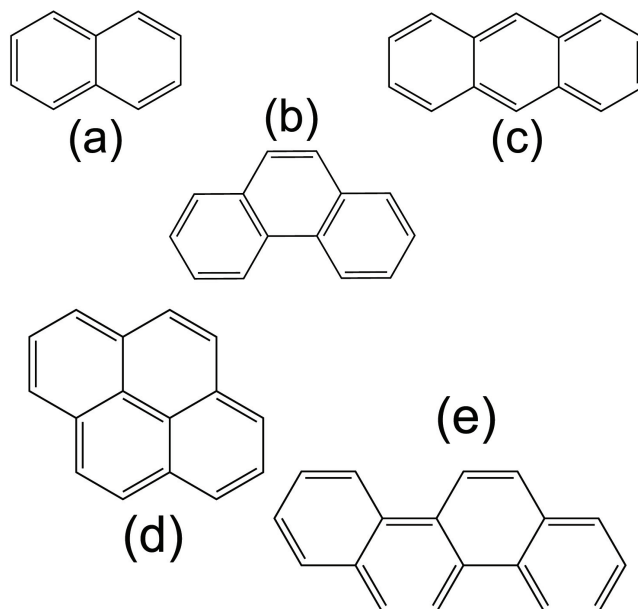


Figure 1.1: Some PAH parent structures: (a) naphthalene, (b) phenanthrene, (c) anthracene, (d) pyrene, (e) chrysene.

Like many persistent organic pollutants (POPs), PAHs are highly stable in many environments. While solid phases have the greatest longevity,⁷ liquid and gas phase PAHs are also persistent and can additionally undergo long-range transport.⁴ The surface chemistries of PAHs allow for a number of derivative structures to be formed, changing their phase availability or stability, where the resulting product depends on availability of other molecules in the area. For example, presence of O₃ or OH-radicals result in derivative PAHs that are more polar than the parent molecule, and are therefore more water soluble.⁷

POPs in general are important to monitor, as they pose significant risks to humans and wildlife, especially marine organisms. PAHs, particularly those of high molecular weight,¹ are of great concern to health as they are known mutagens, leading to various cancers and birth defects, along with organ damage and neurological complications.^{4,5,7,8}

One major source of PAHs in marine waters is produced water (PW), the largest

waste stream from the oil & gas industry.⁹⁻¹¹ PW is any water in contact with oil during extraction processes, and as a result, has a complex composition made up of various hydrocarbons, heavy metals, and other toxic compounds.^{12,13} Estimated volumes of PW outputs are upwards of 41 billion L/day globally, with a ratio of 3 units of PW for every 1 unit of usable oil.¹⁰ Treatments for dealing with PW look to separate suspended solids, dissolved solids, inorganic ions, and dissolved organics.¹⁴ They achieve this by use of centrifuging, coagulation, and filtration, often each with multi-step procedures. While PW should be sufficiently treated by such methods before being streamed back into open waters, as to reduce ecological impacts, current regulatory standards are not rigorous enough. While regulations do exist regarding disposal or reuse (eg. as a source of drinking water) of PW in many countries, the definitions of "treatment" are not uniform, and often minimally only include non-polar organics as something requiring treatment.^{13,15} Additionally, there is currently no governing body in Canada for monitoring of the treatments which are required, where instead oil & gas companies themselves are responsible for this process and "meeting" whichever regulations exist per country.^{11,13,16}

The concern of such large volumes of PW (and therefore PAHs) being dumped into highly mobile waters is not only the immediate effects on the local environment, but also the long-term effects on marine wildlife, eventually impacting humans directly. Fish and other organisms may accumulate small amounts of PAHs into their system over a given period of time,⁵ but this is still of serious concern as these hydrophobic molecules are bioaccumulative, and consequently bio-magnify up the food chain.^{4,17} When humans consume aquatic organisms that have spent significant time in POP-laden waters, the accumulated molecules are subsequently absorbed, where only some amount will be metabolized out of our systems.⁵

Prior to dealing with the sequestration or treatment of PAHs in the environment,

the initial challenge is detection within complex matrices. PAHs are often reported in total amounts along with individual molecule concentrations, due to the fact that the whole of this class is of concern.¹¹ While methods like mass spectrometry are effective in elucidating PAHs within complex matrices,^{15,18} it involves detailed extractions, complex workup, pre-determined solvent systems, and comes with high operating costs.¹⁹ Alternate analytical methods, particularly those based in spectroscopy instead of chromatography, offer more simplistic, faster, and cheaper sampling/analysis.

1.2 SERS in sensing

A powerful spectroscopic analytical method is surface-enhanced Raman spectroscopy, commonly known as SERS, which is a specialized type of Raman spectroscopy.

Raman is a method similar to infrared spectroscopy (IR; FT-IR), where light is used to investigate materials and their bond vibrations. While IR involves absorption of incident light, Raman studies light which is scattered. The scattered light collected is that which is inelastically scattered, and the subsequent difference in energy between incident and collected light gives us information on bonds present (ie. the Raman active modes). As we are only interested in inelastically scattered light for Raman, the scattered light which has not changed in energy from the source (elastic) is not collected.

This light with changed energy only makes up a small fraction of that which is scattered, at around one in a million photons being inelastically scattered.²⁰ Due to the Raman effect being inherently weak, therefore presenting challenges in practical use, specialized subtypes of Raman spectroscopy subsequently have been developed. The goal of these new methodical approaches is typically to amplify the signal, such that more photons with shifted energy are created and/or collected. These methods

include: resonance Raman,²¹ stimulated Raman spectroscopy (SRS),²² coherent anti-Stokes Raman scattering (CARS),²³ surface-enhanced Raman spectroscopy (SERS),²⁴ and tip-enhanced Raman spectroscopy (TERS).²⁵ Of all the Raman-based methods in practice, SERS is the most widely explored with the largest body of research.^{26,27}

1.2.1 Plasmonic materials

Traditional SERS utilizes a nanoscale-roughened metal surface where free electrons on the surface of these metals help to amplify the local electromagnetic (EM) field. The electrons oscillate when stimulated by the laser of the Raman system, which directly leads to the required electromagnetic enhancement.²⁸⁻³⁰ These groups of electrons in oscillation are called a "plasmon", used to quantify this surface EM field activity, where the research field studying the phenomenon is plasmonics.²⁹

This oscillation, and resultant increase in EM field strength locally, helps create a larger Raman cross-section for the analytes than they would have in traditional Raman alone.^{31,32} Though a variety of materials are now used to stimulate this effect, traditionally textured Au and Ag surfaces have been used.^{33,34}

Other pure metals beyond Au and Ag have been studied within a SERS/plasmonics context, such as Cu,³⁵ Pt,³⁶ or Al,³⁷ along with combinations of pure metals.^{25,34} As well, metal oxides (such as TiO₂,³⁴ Fe₃O₄,³⁸ SnO,^{39,40} In₂O₃^{39,41,42}), graphene,⁴³ and non-oxide metallic semiconductors (InGaAs,³⁷ GaN,⁴² SiC⁴²) have been of great interest in recent years as plasmonic materials, where their optoelectronic properties are advantageous in plasmonic applications.^{29,42} Combinations of these materials, along with modifications like doping,^{37,41} may allow for EM field enhancement as an optoelectronic component.

SERS holds many advantages over other sensing methods, both in the preparation of samples and in the collection of data. SERS surfaces can be designed for a target

analyte, offering not only selectivity within complex systems, but sensitive and fast sensing.⁴⁴ Additionally, aqueous samples can be readily and effectively analyzed via SERS/Raman,^{45,46} while in IR, the overwhelmingly dominant OH-stretch of water will prevent any analyte spectrum from being obtained.

1.2.2 SERS Challenges

As environmental or biological systems are indeed complex with many molecules in any given sample, it is important to be able to detect any analytes of interest with precision and accuracy. A complex matrix is a challenge with any analytical method,^{8,47} and this is no different for practical use of SERS. Though surfaces and plasmonic materials can certainly be tailored for specific uses to great effect, as previously cited, the challenge lies in determining what methods and materials will best achieve this.

SERS finds a variety of uses in biological and biochemical sensing, where the challenge is to detect specific toxins,^{48–50} proteins,^{49,51} biomarkers,^{27,52,53} or bacteria/viruses,^{54–56} among other analytes. Matrices in SERS biosensing can include things like blood serum,^{27,46,53,57} saliva,^{27,58} spinal fluid,^{52,59} or even foodstuffs.^{48,50,60} These matrices, especially those involved in biological metabolism, often contain hundreds to thousands of compounds in a sample.⁶¹ Likewise, environmental matrices can contain thousands of compounds within one sample,⁶² such as the previously discussed example of produced water, along with soil^{63–65} and air⁶⁶ samples.

Even when emulating a sensing scenario in-lab with a simplified analogue for any system, SERS sensing can be challenging. While SERS allows for an enhanced signal, the use of a new surface typically creates a spectral fingerprint that differs to some degree from the traditional Raman spectrum.^{67,68} As the molecule of interest adheres to the specialized SERS surface, this adsorption effectively alters the symmetry of the molecule.⁶⁸ This specific orientation may allow some modes to present more domi-

nantly than they would in a standard Raman spectrum of the same material, and at the same time, some modes present in standard Raman may be minor or not visible in the SERS spectrum.

1.3 Nanostructures: Bottom-up and Top-down Fabrication Methods

Both in SERS and beyond, structuring on the nanoscale can allow for powerful performance in optoelectronic useage. There are a number of methods by which nanostructures can be fabricated, fitting into two main approaches: bottom-up and top-down methods.^{45,69} Bottom-up fabrication focuses on assembling nanoscale materials to form some bigger structure, while top-down methods begin with bulk amounts of material which are reduced to nanoscale details (Figure 1.2). Examples of bottom-up assembly methods include atomic layer deposition (ALD),⁷⁰ chemical vapour deposition (CVD),⁷¹ and molecular self-assembly.⁷²⁻⁷⁴ Top-down methods can include use of thermal oxidation,⁷¹ photo-sensitive etching,⁴⁵ or plasma etching⁷⁵ to lithographically pattern on a surface.

For sensing, top-down structured metamaterials are very popular but their fabrication is often complex and not scalable, limiting their practicality.⁷⁶ Working with free NPs can allow for a bottom-up approach to be used, as the nanoscale particles can be synthesized for specific needs (size, shapes, etc.) and then arranged, allowing for faster, cheaper, and more versatile fabrication.

1.3.1 Nanoparticles

In addition to the tailored plasmonic properties of nanostructures,⁷⁷ nanoparticles also provide a number of advantages in sensing, including high surface area,⁷⁸⁻⁸⁰ along with

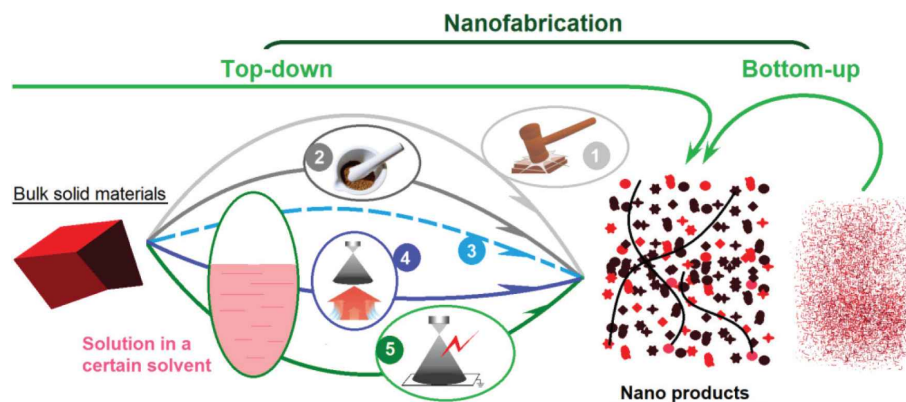


Figure 1.2: An illustration showing top-down and bottom-up approaches to nanofabrication. Image used without modification with permission from Atlantic Press (licensed under CC-BY-NC 4.0). H. Lv *et al.*, *Nanofabrication of Janus Fibers through Side-by-Side Electrospinning - A Mini Review*, Mater. Highlights, 2 (1-2), 2021.

more practical control within nanoscale device design.

For the specific case of SERS sensing, nanostructures are highly effective for creating surfaces with plasmonic "hot spots", areas of highly increased local EM activity.^{26,27,49,81} A high incidence of hot spots increases likelihood of enhancement at any given location on the surface. Plasmonic materials such as nanostars,^{27,82} octahedra,⁸³⁻⁸⁵ or pyramids⁸⁶⁻⁸⁸ have been used to take advantage of geometries that have greater field enhancement on angular or pointed areas of their surface.

There is substantial literature on nanoparticle preparation, with a number of different methods that one can use for synthesis. Methods for creation of NPs may include, but are not limited to, hydrothermal sythesis,^{89,90} sol-gel,^{91,92} spray pyrolysis,^{93,94} pH-mediated coprecipitation,⁹⁵⁻⁹⁸ or solvothermal decomposition.⁹⁹ Of these syntheses, coprecipitation is the method with the largest body of research, due to its simplicity and effectiveness in product yields. It is important to note that this method is both referred to as "precipitation" and "coprecipitation", and though the latter may seem to imply multiple products being formed, in actuality it results in one type of solid NP product.

Each method has strengths depending on what product one is aiming to create, where the most common desire is a particular size (or size distribution) of particles.¹⁰⁰ However, regardless of synthesis targets, control of all variables is both highly important and highly challenging when working with NP formation. Even simple scaling up of procedures can result in changes in product morphology, composition, or shapes, as there is a complex balance of kinetics versus thermodynamics at play.^{101,102}

NPs themselves can be comprised of many different materials, including pure metals,¹⁰³ metal oxides,^{104,105} polymers,¹⁰⁶ or mixtures.^{107–109} Depending on the sensitivity or stability of the products, the NPs may additionally be capped with some inert layer like organosilanes,^{110,111} citrate,^{33,52} or organic polymers.^{112–114}

One particularly interesting composite sub-type is that of core-shell particles, typically comprised of one nanoparticle "core" with another material as the outer coating or "shell". One of the most popular types of core-shell NP combinations is that of gold with iron oxide NPs (IONPs), specifically magnetic forms. These typically have a Fe_3O_4 or $\gamma\text{-Fe}_2\text{O}_3$ core with a gold shell,^{115,116} but there are some examples of the inverse arrangement.^{117,118} These core shell materials have many practical uses in biomedicine, imaging, as well as sensing and optics.

1.4 Magnetic nanoparticles and their applications

IONP/gold core-shell NPs have found important usage in the medical field, primarily as a crucial material in medical imaging⁸⁰ and drug-delivery.⁹¹ The so-called "magnetic handle" inner core-shell makes physical manipulation and control of the NPs in space perfect for targeted drug delivery, and similarly, the magnetism of the core makes it useful for magnetic resonance imaging (MRI). As the magnetic character of IONPs is one of their most useful attributes, this also goes for other types of magnetic

NPs.

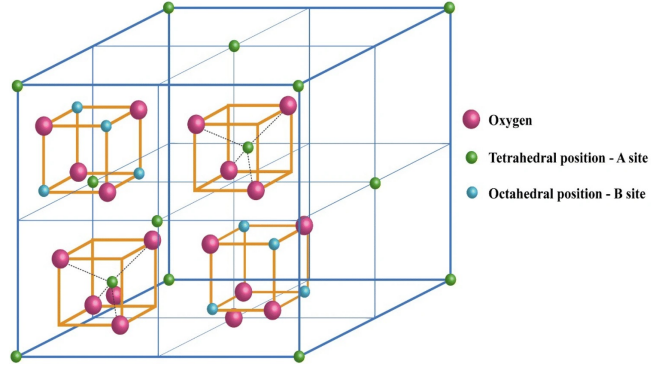


Figure 1.3: Simplified schematic of an inverse spinel crystal structure, showing the tetrahedral and octahedral metal sites, along with the oxygen occupancy. *Reprinted by permission from Springer Nature GmbH: Springer Nature, Applied Physics A, Estimating the ionicity of an inverse spinel ferrite and the cation distribution of La-doped NiFe_2O_4 nanocrystals for gas sensing properties, S. Deepapriya, S. Lakshmi Devi, P. Annie Vinosha, John D. Rodney, C. Justin Raj, J. Ermine Jose, S. Jerome Das, Copyright 2019.*

Magnetic iron oxides like Fe_3O_4 have an inverse spinel crystal structure (Figure 1.3),¹¹³ and there are two different geometries for the metal ions: a tetrahedral site (T_d) and an octahedral site (O_h). These sites contain 3+ and 2+ valence states of iron, and as such, Fe_3O_4 can also be written as $\text{Fe}^{2+}\text{Fe}_2^{3+}\text{O}_4$. The O_h sites contain both Fe^{2+} and Fe^{3+} , while the T_d sites only contain Fe^{3+} ; regardless of geometry, not all octahedral and tetrahedral holes are occupied. The magnetic spins of the 3+ O_h and 3+ T_d sites align parallel with equal and opposite magnitudes (therefore cancelling each other), but the 2+ sites remain with their own alignment, making the overall structure ferrimagnetic in nature.¹¹³

There exist other magnetic ferrites with the same crystal type, where the 2+ iron ion is swapped for another metal ion with a 2+ valence state, such as Co^{2+} ^{119,120} or Ni^{2+} .^{121,122} While the crystal structure itself remains the same with these ion swaps, new lattice parameters result in small length changes in the structure. New electron configurations result in slight changes in magnitude of the magnetic characteristics as

well.¹²³

While iron oxides have been well-studied in the literature, both in a characterization context and for practical applications, these metal-swapped ferrite analogues have not been as well investigated.¹²⁴ Cobalt and nickel ferrite (CFNPs and NFNPs, respectively) boast altered magnetic and optoelectronic properties that make them potentially more advantageous choices than IONPs for certain applications, which have led to them becoming of interest in recent years.

Particularly in the context of the plasmonic sensing materials previously discussed, IONPs, CFNPs, and NFNPs have not been explored as inherently SERS-active materials. There are no SERS studies including CFNPs and NFNPs, and those which apply IONPs in a SERS context^{19,125,126} are almost exclusively using them as a handle for the “main” plasmonic contributor of gold (or silver), as discussed regarding core-shell particle designs. Scaramuzza *et al.*²⁶ saw increased SERS signal with an applied magnetic field, but they attribute this to aggregation of mixed iron-silver NPs and not to direct influence of the magnetic field on the plasmonic response. Therefore, this is another example of using magnetic fields to move spheres, not to directly impact the plasmonic field.

Taking magnetism in this context one step further, very few studies look at the impacts of applying a magnetic field onto the sensing surface during spectral acquisition, with aims to increase the overall EM field strength as a result. One of the few studies which addresses a direct link between plasmonic behaviour, magnetic materials, and applied fields is work from Podolak *et al.*,¹²⁷ where they noted a shift in the surface plasmon resonance (SPR) peak with both increasing thickness of an iron oxide layer and application of a magnetic field. More recent work also shows a response of the plasmonic field to applied magnetic fields.¹²⁸

1.5 Summary of the thesis

My work is the first to acknowledge and explore the role of magnetic materials in SERS activity. This thesis looks into the practical synthesis of IONPs and CFNPs, changes in CFNP crystals with synthesis scaling, and then designing and implementing these NPs into practical plasmonic devices for future environmental sensing.

In Chapter 2, the properties of IONPs synthesized by precipitation are characterized, and initial designs of a new type of SERS sensor are investigated. This sensor uses magnetic NPs at the forefront of the sensing platform, which has not been reported previously, and makes use of a complex patterned multilayer of NPs made via an external magnetic field. LOD and complex matrix tests show very high performance of this surface as a SERS sensor.

Chapter 3 provides the details of the novel SERS sensor design are reported in a legal context, as prepared for the corresponding provisional patent application.

In Chapter 4, CFNPs are synthesized by precipitation and characterized, where a mixed crystal geometry is reported. These new products are then integrated into a new iteration of the sensor design found in Chapter 2, where its performance as a SERS surface is found to be exceptional in both enhancement and reproducibility.

Chapter 5 further explores the use of CFNPs as a strong SERS material, as well as studying changes in the resultant crystal product when the scale of the synthesis is altered. As the scale changes, different geometries form on the nanoscale. These products correlate with altered performance as plasmonic surfaces, due to changes in morphology and magnetic response.

Bibliography

- [1] Yeo, B. G.; Takada, H.; Hosoda, J.; Kondo, A.; Yamashita, R.; Saha, M.; Maes, T. Polycyclic Aromatic Hydrocarbons (PAHs) and Hopanes in Plastic Resin Pellets as Markers of Oil Pollution via International Pellet Watch Monitoring. *Arch. Environ. Contam. Toxicol.* **2017**, *73*, 196–206.
- [2] Ke, C. L.; Gu, Y. G.; Liu, Q.; Li, L. D.; Huang, H. H.; Cai, N.; Sun, Z. W. Polycyclic aromatic hydrocarbons (PAHs) in wild marine organisms from South China Sea: Occurrence, sources, and human health implications. *Mar. Pollut. Bull.* **2017**, *117*, 507–511.
- [3] Shahsavari, E.; Schwarz, A.; Aburto-Medina, A.; Ball, A. S. Biological Degradation of Polycyclic Aromatic Compounds (PAHs) in Soil: a Current Perspective. *Curr. Pollut. Reports* **2019**, *5*, 84–92.
- [4] Ontiveros-Cuadras, J. F.; Ruiz-Fernández, A. C.; Sanchez-Cabeza, J. A.; Sericano, J.; Pérez-Bernal, L. H.; Páez-Osuna, F.; Dunbar, R. B.; Mucciarone, D. A. Recent history of persistent organic pollutants (PAHs, PCBs, PBDEs) in sediments from a large tropical lake. *J. Hazard. Mater.* **2019**, *368*, 264–273.
- [5] Farrington, J. W. Need to update human health risk assessment protocols for polycyclic aromatic hydrocarbons in seafood after oil spills. *Mar. Pollut. Bull.* **2020**, *150*, 110744.
- [6] Li, Q.; Kartikowati, C. W.; Horie, S.; Ogi, T.; Iwaki, T.; Okuyama, K. Correlation between particle size/domain structure and magnetic properties of highly crystalline Fe₃O₄ nanoparticles. *Sci. Rep.* **2017**, *7*, 1–4.
- [7] Boström, C.-E.; Gerde, P.; Hanberg, A.; Jernström, B.; Johansson, C.; Kyrklund, T.; Rannug, A.; Törnqvist, M.; Victorin, K.; Westerholm, R. Cancer risk

assessment, indicators, and guidelines for polycyclic aromatic hydrocarbons in the ambient air. *Environ. Health Perspect.* **2002**, *110*, 451–488.

- [8] Nováková, Z.; Novák, J.; Kitanovski, Z.; Kukučka, P.; Smutná, M.; Wietzoreck, M.; Lammel, G.; Hilscherová, K. Toxic potentials of particulate and gaseous air pollutant mixtures and the role of PAHs and their derivatives. *Environ. Int.* **2020**, *139*, 105634.
- [9] Al-Ghouti, M. A.; Al-Kaabi, M. A.; Ashfaq, M. Y.; Da'na, D. A. Produced water characteristics, treatment and reuse: A review. *J. Water Process Eng.* **2019**, *28*, 222–239.
- [10] Alammar, A.; Park, S. H.; Williams, C. J.; Derby, B.; Szekely, G. Oil-in-water separation with graphene-based nanocomposite membranes for produced water treatment. *J. Memb. Sci.* **2020**, *603*, 118007.
- [11] Lee, K.; Neff, J. *Prod. Water*; Springer: 233 Spring Street, New York, USA, 2011; p 601.
- [12] Scanlon, B. R.; Reedy, R. C.; Xu, P.; Engle, M.; Nicot, J. P.; Yoxtheimer, D.; Yang, Q.; Ikonnikova, S. Can we beneficially reuse produced water from oil and gas extraction in the U.S.? *Sci. Total Environ.* **2020**, *717*, 137085.
- [13] Jiménez, S.; Micó, M. M.; Arnaldos, M.; Medina, F.; Contreras, S. State of the art of produced water treatment. *Chemosphere* **2018**, *192*, 186–208.
- [14] Lin, L.; Jiang, W.; Chen, L.; Xu, P.; Wang, H. Treatment of produced water with photocatalysis: Recent advances, affecting factors and future research prospects. *Catalysts* **2020**, *10*, 924.

- [15] McLaughlin, M. C.; Borch, T.; McDevitt, B.; Warner, N. R.; Blotvogel, J. Water quality assessment downstream of oil and gas produced water discharges intended for beneficial reuse in arid regions. *Sci. Total Environ.* **2020**, *713*, 136607.
- [16] Røe Utvik, T. I. Chemical characterisation of produced water from four offshore oil production platforms in the North Sea. *Chemosphere* **1999**, *39*, 2593–2606.
- [17] Petrovic, M.; Sremacki, M.; Radonic, J.; Mihajlovic, I.; Obrovski, B.; Vojinovic Miloradov, M. Health risk assessment of PAHs, PCBs and OCPs in atmospheric air of municipal solid waste landfill in Novi Sad, Serbia. *Sci. Total Environ.* **2018**, *644*, 1201–1206.
- [18] Jiménez, S.; Andreozzi, M.; Micó, M. M.; Álvarez, M. G.; Contreras, S. Produced water treatment by advanced oxidation processes. *Sci. Total Environ.* **2019**, *666*, 12–21.
- [19] Du, J.; Jing, C. Preparation of Thiol Modified Fe₃O₄@Ag Magnetic SERS Probe for PAHs Detection and Identification. *J. Phys. Chem. C* **2011**, *115*, 17829–17835.
- [20] Rodriguez-Lorenzo, L.; Alvarez-Puebla, R. *Nanosensors Chem. Biol. Appl.*; 2014; pp 197–230.
- [21] Zobeiri, H.; Xu, S.; Yue, Y.; Zhang, Q.; Xie, Y.; Wang, X. Effect of temperature on Raman intensity of nm-thick WS₂: Combined effects of resonance Raman, optical properties, and interface optical interference. *Nanoscale* **2020**, *12*, 6064–6078.
- [22] Hu, F.; Shi, L.; Min, W. Biological imaging of chemical bonds by stimulated Raman scattering microscopy. *Nat. Methods* **2019**, *16*, 830–842.

- [23] Virga, A.; Ferrante, C.; Batignani, G.; De Fazio, D.; Nunn, A. D.; Ferrari, A. C.; Cerullo, G.; Scopigno, T. Coherent anti-Stokes Raman spectroscopy of single and multi-layer graphene. *Nat. Commun.* **2019**, *10*, 1–9.
- [24] Hussein, M. A.; El-Said, W. A.; Abu-Zied, B. M.; Choi, J. W. Nanosheet composed of gold nanoparticle/graphene/epoxy resin based on ultrasonic fabrication for flexible dopamine biosensor using surface-enhanced Raman spectroscopy. *Nano Converg.* **2020**, *7*.
- [25] Su, H. S.; Feng, H. S.; Zhao, Q. Q.; Zhang, X. G.; Sun, J. J.; He, Y.; Huang, S. C.; Huang, T. X.; Zhong, J. H.; Wu, D. Y.; Ren, B. Probing the Local Generation and Diffusion of Active Oxygen Species on a Pd/Au Bimetallic Surface by Tip-Enhanced Raman Spectroscopy. *J. Am. Chem. Soc.* **2020**, *142*, 1341–1347.
- [26] Scaramuzza, S.; Polizzi, S.; Amendola, V. Magnetic tuning of SERS hot spots in polymer-coated magnetic-plasmonic iron-silver nanoparticles. *Nanoscale Adv.* **2019**, *1*, 2681–2689.
- [27] Szlag, V. M.; Rodriguez, R. S.; He, J.; Hudson-Smith, N.; Kang, H.; Le, N.; Reineke, T. M.; Haynes, C. L. Molecular Affinity Agents for Intrinsic Surface-Enhanced Raman Scattering (SERS) Sensors. *ACS Appl. Mater. Interfaces* **2018**, *10*, 31825–31844.
- [28] Ko, H.; Singamaneni, S.; Tsukruk, V. V. Nanostructured surfaces and assemblies as SERS media. *Small* **2008**, *4*, 1576–1599.
- [29] Naik, G. V.; Shalaev, V. M.; Boltasseva, A. Alternative plasmonic materials: Beyond gold and silver. *Adv. Mater.* **2013**, *25*, 3264–3294.

- [30] Daniels, J. K.; Chumanov, G. Nanoparticle–Mirror Sandwich Substrates for Surface-Enhanced Raman Scattering. *J. Phys. Chem. B* **2005**, *109*, 17936–17942.
- [31] Shen, J.; Zhu, Y.; Yang, X.; Zong, J.; Li, C. Multifunctional Fe₃O₄@Ag/SiO₂/Au core-shell microspheres as a novel SERS-activity label via long-range plasmon coupling. *Langmuir* **2013**, *29*, 690–695.
- [32] Lee, H. K.; Lee, Y. H.; Koh, C. S. L.; Phan-Quang, G. C.; Han, X.; Lay, C. L.; Sim, H. Y. F.; Kao, Y. C.; An, Q.; Ling, X. Y. Designing surface-enhanced Raman scattering (SERS) platforms beyond hotspot engineering: Emerging opportunities in analyte manipulations and hybrid materials. *Chem. Soc. Rev.* **2019**, *48*, 731–756.
- [33] Mertens, J.; Kleemann, M. E.; Chikkaraddy, R.; Narang, P.; Baumberg, J. J. How Light Is Emitted by Plasmonic Metals. *Nano Lett.* **2017**, *17*, 2568–2574.
- [34] Jiao, A.; Cui, Q.; Li, S.; Li, H.; Xu, L.; Tian, Y.; Ma, H.; Zhang, M.; Liu, X.; Chen, M. Aligned TiO₂ nanorod arrays decorated with closely interconnected Au/Ag nanoparticles: near-infrared SERS active sensor for monitoring of antibiotic molecules in water. *Sensors Actuators B Chem.* **2021**, *350*, 130848.
- [35] Ruan, C.; Luo, W.; Wang, W.; Gu, B. Surface-enhanced Raman spectroscopy for uranium detection and analysis in environmental samples. *Anal. Chim. Acta* **2007**, *605*, 80–86.
- [36] Wei, Z.; Endo-Kimura, M.; Wang, K.; Colbeau-Justin, C.; Kowalska, E. Influence of semiconductor morphology on photocatalytic activity of plasmonic photocatalysts: Titanate nanowires and octahedral anatase nanoparticles. *Nanomaterials* **2019**, *9*, 1–18.

- [37] Hsieh, W. T.; Wu, P. C.; Khurgin, J. B.; Tsai, D. P.; Liu, N.; Sun, G. Comparative Analysis of Metals and Alternative Infrared Plasmonic Materials. *ACS Photonics* **2018**, *5*, 2541–2548.
- [38] Lee, N.; Schuck, P. J.; Nico, P. S.; Gilbert, B. Surface Enhanced Raman Spectroscopy of Organic Molecules on Magnetite (Fe_3O_4) Nanoparticles. *J. Phys. Chem. Lett.* **2015**, 970–974.
- [39] Boltasseva, A.; Atwater, H. Low-Loss Plasmonic Metamaterials. *Science*. **2011**, *331*, 290–292.
- [40] Yu, Y.; Zhang, G. In *Updat. Adv. Lithogr.*; Hosaka, S., Ed.; InTech, 2013; Chapter Colloidal, pp 3–34.
- [41] Runnerstrom, E. L.; Bergerud, A.; Agrawal, A.; Johns, R. W.; Dahlman, C. J.; Singh, A.; Selbach, S. M.; Milliron, D. J. Defect Engineering in Plasmonic Metal Oxide Nanocrystals. *Nano Lett.* **2016**, *16*, 3390–3398.
- [42] West, P. R.; Ishii, S.; Naik, G. V.; Emani, N. K.; Shalaev, V. M.; Boltasseva, A. Searching for better plasmonic materials. *Laser Photonics Rev.* **2010**, *4*, 795–808.
- [43] Liu, Y.; Cheng, R.; Liao, L.; Zhou, H.; Bai, J.; Liu, G.; Liu, L.; Huang, Y.; Duan, X. Plasmon resonance enhanced multicolour photodetection by graphene. *Nat. Commun.* **2011**, *2*, 579.
- [44] Li, P.; Ge, M.; Cao, C.; Lin, D.; Yang, L. High-affinity $\text{Fe}_3\text{O}_4/\text{Au}$ probe with synergetic effect of surface plasmon resonance and charge transfer enabling improved SERS sensing of dopamine in biofluids. *Analyst* **2019**, 4526–4533.

- [45] Zhao, M.; Shaikh, S.; Kang, R.; Markiewicz-Keszycka, M. Investigation of Raman Spectroscopy (with Fiber Optic Probe) and Chemometric Data Analysis for the Determination of Mineral Content in Aqueous Infant Formula. *Foods* **2020**, *9*, 968.
- [46] Chen, J.; Yang, Y.; Lin, B.; Wei, X.; Lin, Z.; Hong, G. Calcium Alginate Gel Beads Containing Gold Nanobipyramids for Surface-Enhanced Raman Scattering Detection in Aqueous Samples. *ACS Appl. Nano Mater.* **2021**,
- [47] Pardehkhorrām, R.; Alshawawreh, F.; Gonçalves, V. R.; Lee, N. A.; Tilley, R. D.; Gooding, J. J. Functionalized Gold Nanorod Probes: A Sophisticated Design of SERS Immunoassay for Biodetection in Complex Media. *Anal. Chem.* **2021**, *93*, 12954–12965.
- [48] Wang, Y.; Ravindranath, S.; Irudayaraj, J. Separation and detection of multiple pathogens in a food matrix by magnetic SERS nanoprobe. *Anal. Bioanal. Chem.* **2011**, *399*, 1271–1278.
- [49] Chung, T.; Lee, Y.; Ahn, M. S.; Lee, W.; Bae, S. I.; Hwang, C. S. H.; Jeong, K. H. Nanoislands as plasmonic materials. *Nanoscale* **2019**, *11*, 8651–8664.
- [50] Hassan, M. M.; Zareef, M.; Xu, Y.; Li, H.; Chen, Q. SERS based sensor for mycotoxins detection: Challenges and improvements. *Food Chem.* **2021**, *344*, 128652.
- [51] Ivleva, N. P.; Wagner, M.; Szkola, A.; Horn, H.; Niessner, R.; Haisch, C. Label-free in situ SERS imaging of biofilms. *J. Phys. Chem. B* **2010**, *114*, 10184–10194.

- [52] Maurer, V.; Frank, C.; Porsiel, J. C.; Zellmer, S.; Garnweitner, G.; Stosch, R. Step-by-step monitoring of a magnetic and SERS-active immunosensor assembly for purification and detection of tau protein. *J. Biophotonics* **2020**, *13*, 1–10.
- [53] Song, C. Y.; Yang, Y. J.; Yang, B. Y.; Sun, Y. Z.; Zhao, Y. P.; Wang, L. H. An ultrasensitive SERS sensor for simultaneous detection of multiple cancer-related miRNAs. *Nanoscale* **2016**, *8*, 17365–17373.
- [54] Wang, C.; Wang, C.; Wang, X.; Wang, K.; Zhu, Y.; Rong, Z.; Wang, W.; Xiao, R.; Wang, S. Magnetic SERS Strip for Sensitive and Simultaneous Detection of Respiratory Viruses. *ACS Appl. Mater. Interfaces* **2019**, *11*, 19495–19505.
- [55] Dardir, K.; Wang, H.; Martin, B. E.; Atzampou, M.; Brooke, C. B.; Fabris, L. SERS Nanoprobe for Intracellular Monitoring of Viral Mutations. *J. Phys. Chem. C* **2020**, *124*, 3211–3217.
- [56] Sun, Y.; Xu, L.; Zhang, F.; Song, Z.; Hu, Y.; Ji, Y.; Shen, J.; Li, B.; Lu, H.; Yang, H. A promising magnetic SERS immunosensor for sensitive detection of avian influenza virus. *Biosens. Bioelectron.* **2017**, *89*, 906–912.
- [57] Tran, V.; Walkenfort, B.; König, M.; Salehi, M.; Schlücker, S. Rapid, Quantitative, and Ultrasensitive Point-of-Care Testing: A Portable SERS Reader for Lateral Flow Assays in Clinical Chemistry. *Angew. Chemie - Int. Ed.* **2019**, *58*, 442–446.
- [58] Stefancu, A.; Badarinza, M.; Moisoiu, V.; Iancu, S. D.; Serban, O.; Leopold, N.; Fodor, D. SERS-based liquid biopsy of saliva and serum from patients with Sjögren’s syndrome. *Anal. Bioanal. Chem.* **2019**, *411*, 5877–5883.

- [59] Wallace, G. Q.; Delignat-Lavaud, B.; Zhao, X.; Trudeau, L. É.; Masson, J. F. A blueprint for performing SERS measurements in tissue with plasmonic nanofibers. *J. Chem. Phys.* **2020**, *153*.
- [60] Wei, C.; Li, M.; Zhao, X. Surface-enhanced raman scattering (SERS) with silver nano substrates synthesized by microwave for rapid detection of foodborne pathogens. *Front. Microbiol.* **2018**, *9*, 1–9.
- [61] Cook, D. W.; Rutan, S. C. Chemometrics for the analysis of chromatographic data in metabolomics investigations. *J. Chemom.* **2014**, *28*, 681–687.
- [62] The Challenge of Micropollutants. *Sci. Technol.* **2006**, *313*, 1072–1077.
- [63] Zhang, C. H.; Zhu, J.; Li, J. J.; Zhao, J. W. Small and Sharp Triangular Silver Nanoplates Synthesized Utilizing Tiny Triangular Nuclei and Their Excellent SERS Activity for Selective Detection of Thiram Residue in Soil. *ACS Appl. Mater. Interfaces* **2017**, *9*, 17387–17398.
- [64] He, Y.; Xiao, S.; Dong, T.; Nie, P. Gold nanoparticles with different particle sizes for the quantitative determination of chlorpyrifos residues in soil by SERS. *Int. J. Mol. Sci.* **2019**, *20*, 2817.
- [65] Gong, T.; Huang, Y.; Wei, Z.; Huang, W.; Wei, X.; Zhang, X. Magnetic assembled 3D SERS substrate for sensitive detection of pesticide residue in soil. *Nanotechnology* **2020**, *31*, 205501.
- [66] Phan-Quang, G. C.; Lee, H. K.; Teng, H. W.; Koh, C. S. L.; Yim, B. Q.; Tan, E. K. M.; Tok, W. L.; Phang, I. Y.; Ling, X. Y. Plasmonic Hotspots in Air: An Omnidirectional Three-Dimensional Platform for Stand-Off In-Air SERS Sensing of Airborne Species. *Angew. Chemie - Int. Ed.* **2018**, *57*, 5792–5796.

- [67] Aroca, R. F.; Clavijo, R. E.; Halls, M. D.; Schlegel, H. B. Surface-enhanced raman spectra of phthalimide. Interpretation of the SERS spectra of the surface complex formed on silver islands and colloids. *J. Phys. Chem. A* **2000**, *104*, 9500–9505.
- [68] Panicker, C. Y.; Varghese, H. T.; Philip, D.; Nogueira, H. I. FT-IR, FT-Raman and SERS spectra of pyridine-3-sulfonic acid. *Spectrochim. Acta - Part A Mol. Biomol. Spectrosc.* **2006**, *64*, 744–747.
- [69] Lv, H.; Yu, D.-G.; Wang, M.; Ning, T. Nanofabrication of Janus Fibers through Side-by-Side Electrospinning - A Mini Review. *Mater. Highlights* **2021**, *2*, 18.
- [70] Cai, H.; Meng, Q.; Zhao, H.; Li, M.; Dai, Y.; Lin, Y.; Ding, H.; Pan, N.; Tian, Y.; Luo, Y.; Wang, X. High-Throughput Fabrication of Ultradense Annular Nanogap Arrays for Plasmon-Enhanced Spectroscopy. *ACS Appl. Mater. Interfaces* **2018**, *10*, 20189–20195.
- [71] Bao, Z.; Sun, J.; Zhao, X.; Li, Z.; Cui, S.; Meng, Q.; Zhang, Y.; Wang, T.; Jiang, Y. Top-down nanofabrication of silicon nanoribbon field effect transistor (Si-NR FET) for carcinoembryonic antigen detection. *Int. J. Nanomedicine* **2017**, *12*, 4623–4631.
- [72] Wang, P. Y.; Shields, C. W.; Zhao, T.; Jami, H.; López, G. P.; Kingshott, P. Rapid Self-Assembly of Shaped Microtiles into Large, Close-Packed Crystalline Monolayers on Solid Surfaces. *Small* **2016**, *12*, 1309–1314.
- [73] Greybush, N. J.; Saboktakin, M.; Ye, X.; Giovampaola, C. D.; Oh, S. J.; Berry, N. E.; Engheta, N.; Murray, C. B.; Kagan, C. R. Plasmon-Enhanced Upconversion Luminescence in Single Nanophosphor Å Nanorod Heterodimers Formed through. *ACS Nano* **2014**, *8*, 9482–9491.

- [74] Chen, G.; Gibson, K. J.; Liu, D.; Rees, H. C.; Lee, J. H.; Xia, W.; Lin, R.; Xin, H. L.; Gang, O.; Weizmann, Y. Regioselective surface encoding of nanoparticles for programmable self-assembly. *Nat. Mater.* **2019**, *18*, 169–174.
- [75] Bardea, A.; Yoffe, A. Magneto – Lithography , a Simple and Inexpensive Method for High Throughput , Surface Patterning. *IEEE Trans. Nanotechnol.* **2017**, *16*, 439–444.
- [76] Yoon, G.; Kim, I.; Rho, J. Challenges in fabrication towards realization of practical metamaterials. *Microelectron. Eng.* **2016**, *163*, 7–20.
- [77] Lim, J.; Majetich, S. A. Composite magnetic-plasmonic nanoparticles for biomedicine: Manipulation and imaging. *Nano Today* **2013**, *8*, 98–113.
- [78] Rebodos, R. L.; Vikesland, P. J. Effects of oxidation on the magnetization of nanoparticulate magnetite. *Langmuir* **2010**, *26*, 16745–16753.
- [79] Fahmy, H. M.; Abd El-Daim, T. M.; Ali, O. A.; Hassan, A. A.; Mohammed, F. F.; Fathy, M. M. Surface modifications affect iron oxide nanoparticles’ biodistribution after multiple-dose administration in rats. *J. Biochem. Mol. Toxicol.* **2021**, *35*, 1–10.
- [80] Ajinkya, N.; Yu, X.; Kaithal, P.; Luo, H.; Somani, P.; Ramakrishna, S. Magnetic iron oxide nanoparticle (IONP) synthesis to applications: Present and future. *Materials (Basel)*. **2020**, *13*, 1–35.
- [81] Cong, S.; Yuan, Y.; Chen, Z.; Hou, J.; Yang, M.; Su, Y.; Zhang, Y.; Li, L.; Li, Q.; Geng, F.; Zhao, Z. Noble metal-comparable SERS enhancement from semiconducting metal oxides by making oxygen vacancies. *Nat. Commun.* **2015**, *6*, 1–7.

- [82] Esenturk, E. N.; Hight Walker, A. R. Gold nanostar @ iron oxide core-shell nanostructures: Synthesis, characterization, and demonstrated surface-enhanced Raman scattering properties. *J. Nanoparticle Res.* **2013**, *15*, 1364.
- [83] Lu, Y.; Zhang, H.; Wu, F.; Liu, H.; Fang, J. Size-tunable uniform gold octahedra: fast synthesis, characterization, and plasmonic properties. *RSC Adv.* **2017**, *7*, 18601–18608.
- [84] Khairullina, E.; Mosina, K.; Choueiri, R. M.; Paradis, A. P.; Petruk, A. A.; Sciaini, G.; Krivoschapkina, E.; Lee, A.; Ahmed, A.; Klinkova, A. An aligned octahedral core in a nanocage: Synthesis, plasmonic, and catalytic properties. *Nanoscale* **2019**, *11*, 3378–3385.
- [85] Lee, M. G.; Moon, C. W.; Park, H.; Sohn, W.; Kang, S. B.; Lee, S.; Choi, K. J.; Jang, H. W. Dominance of Plasmonic Resonant Energy Transfer over Direct Electron Transfer in Substantially Enhanced Water Oxidation Activity of BiVO_4 by Shape-Controlled Au Nanoparticles. *Small* **2017**, *13*, 1–11.
- [86] Jia, Z. X.; Shuai, Y.; Zhang, J. H.; Tan, H. P. 2-Dimensional Microlens Based on Uniformed Plasmonic Pyramid Arrays. *Plasmonics* **2018**, *13*, 1483–1490.
- [87] Rigó, I.; Veres, M.; Pápa, Z.; Himics, L.; Öcsi, R.; Hakkell, O.; Fürjes, P. Plasmonic enhancement in gold coated inverse pyramid substrates with entrapped gold nanoparticles. *J. Quant. Spectrosc. Radiat. Transf.* **2020**, *253*.
- [88] Zheng, P.; Kasani, S.; Wu, N. Converting plasmonic light scattering to confined light absorption and creating plexcitons by coupling a gold nano-pyramid array onto a silica-gold film. *Nanoscale Horizons* **2019**, *4*, 495–515.
- [89] Kigozi, M.; Ezealigo, B. N.; Onwualu, A. P.; Dzade, N. Y. *Chem. Depos. Nanocrystalline Met. Oxide Thin Film.*; 2021; pp 489–508.

- [90] Dunne, P. W.; Munn, A. S.; Starkey, C. L.; Huddle, T. A.; Lester, E. H. Continuous-flow hydrothermal synthesis for the production of inorganic nanomaterials. *Philos. Trans. R. Soc. A Math. Phys. Eng. Sci.* **2015**, *373*.
- [91] Abd Elrahman, A. A.; Mansour, F. R. Targeted magnetic iron oxide nanoparticles: Preparation, functionalization and biomedical application. *J. Drug Deliv. Sci. Technol.* **2019**, *52*, 702–712.
- [92] Esposito, S. "Traditional" sol-gel chemistry as a powerful tool for the preparation of supported metal and metal oxide catalysts. *Materials (Basel)*. **2019**, *12*, 1–25.
- [93] Stodt, M. F.; Liu, C.; Li, S.; Mädler, L.; Fritsching, U.; Kiefer, J. Phase-selective laser-induced breakdown spectroscopy in flame spray pyrolysis for iron oxide nanoparticle synthesis. *Proc. Combust. Inst.* **2021**, *38*, 1711–1718.
- [94] Meierhofer, F.; Fritsching, U. Synthesis of Metal Oxide Nanoparticles in Flame Sprays: Review on Process Technology, Modeling, and Diagnostics. *Energy and Fuels* **2021**, *35*, 5495–5537.
- [95] Besenhard, M. O.; LaGrow, A. P.; Hodzic, A.; Kriechbaum, M.; Panariello, L.; Bais, G.; Loizou, K.; Damilos, S.; Margarida Cruz, M.; Thanh, N. T. K.; Gavriilidis, A. Co-precipitation synthesis of stable iron oxide nanoparticles with NaOH: New insights and continuous production via flow chemistry. *Chem. Eng. J.* **2020**, *399*, 125740.
- [96] Patiño-Ruiz, D. A.; Meramo-Hurtado, S. I.; González-Delgado, Á. D.; Herrera, A. Environmental Sustainability Evaluation of Iron Oxide Nanoparticles Synthesized via Green Synthesis and the Coprecipitation Method: A Comparative Life Cycle Assessment Study. *ACS Omega* **2021**, *6*, 12410–12423.

- [97] Noqta, O. A.; Sodipo, B. K.; Aziz, A. A. One-pot synthesis of highly magnetic and stable citrate coated superparamagnetic iron oxide nanoparticles by modified coprecipitation method. *Funct. Compos. Struct.* **2020**, *2*, 045005.
- [98] Shilova, O. A.; Panova, G.; Nikolaev, A.; Kovalenko, A.; Sinelnikov, A.; Kopytsa, G.; Baranchikov, A.; Udalova, O.; Artemyeva, A.; Korniyuchin, D.; Anikina, L.; Zhuravleva, A.; Vertebnyi, V.; Dubovitskaya, V.; Khamova, T. Aqueous Chemical Co-Precipitation of Iron Oxide Magnetic Nanoparticles for Use in Agricultural Technologies. *Lett. Appl. NanoBioScience* **2020**, *10*, 2215–2239.
- [99] Solano, E.; Frontera, C.; Puig, T.; Obradors, X.; Ricart, S.; Ros, J. Neutron and X-ray diffraction study of ferrite nanocrystals obtained by microwave-assisted growth. A structural comparison with the thermal synthetic route. *J. Appl. Crystallogr.* **2014**, *47*, 414–420.
- [100] Dehsari, H. S.; Ribeiro, A. H.; Ersöz, B.; Tremel, W.; Jakob, G.; Asadi, K. Effect of precursor concentration on size evolution of iron oxide nanoparticles. *CrystEngComm* **2017**, *19*, 6694–6702.
- [101] Mourdikoudis, S.; Liz-marza, L. M. Oleylamine in Nanoparticle Synthesis. *Chem. Mater.* **2013**, *25*, 1465–1476.
- [102] Yuan, X.; Zhang, B.; Luo, Z.; Yao, Q.; Leong, D. T.; Yan, N. Balancing the Rate of Cluster Growth and Etching for Gram-Scale Synthesis of Thiolate-Protected Au Nanoclusters with Atomic Precision. *Angew. Chemie* **2014**, *126*, 4711–4715.
- [103] Matricardi, C.; Hanske, C.; Garcia-Pomar, J. L.; Langer, J.; Mihi, A.; Liz-Marzán, L. M. Gold Nanoparticle Plasmonic Superlattices as Surface Enhanced Raman Spectroscopy Substrates. *ACS Nano* **2018**, *12*, 8531–8539.

- [104] Zallouz, S.; Réty, B.; Vidal, L.; Le Meins, J. M.; Matei Ghimbeu, C. Co_3O_4 Nanoparticles Embedded in Mesoporous Carbon for Supercapacitor Applications. *ACS Appl. Nano Mater.* **2021**, *4*, 5022–5037.
- [105] Cho, C. H.; Choe, Y. S.; Oh, J. Y.; Lee, T. I. Self-Assembled 2D Networks of Metal Oxide Nanomaterials Enabling Sub-ppm Level Breathalyzers. *ACS Sensors* **2021**, *6*, 3195–3203.
- [106] Zhang, X.; Do, M. D.; Dean, K.; Hoobin, P.; Burgar, I. M. Wheat-gluten-based natural polymer nanoparticle composites. *Biomacromolecules* **2007**, *8*, 345–353.
- [107] Gao, Z.; Shao, S.; Gao, W.; Tang, D.; Tang, D.; Zou, S.; Kim, M. J.; Xia, X. Morphology-Invariant Metallic Nanoparticles with Tunable Plasmonic Properties. *ACS Nano* **2021**, *15*, 2428–2438.
- [108] Collins, S. S.; Searles, E. K.; Tauzin, L. J.; Lou, M.; Bursi, L.; Liu, Y.; Song, J.; Flatebo, C.; Baiyasi, R.; Cai, Y. Y.; Foerster, B.; Lian, T.; Nordlander, P.; Link, S.; Landes, C. F. Plasmon Energy Transfer in Hybrid Nanoantennas. *ACS Nano* **2021**, *15*, 9522–9530.
- [109] Martins, N. C.; Fateixa, S.; Fernandes, T.; Nogueira, H. I.; Trindade, T. Inkjet Printing of Ag and Polystyrene Nanoparticle Emulsions for the One-Step Fabrication of Hydrophobic Paper-Based Surface-Enhanced Raman Scattering Substrates. *ACS Appl. Nano Mater.* **2021**, *4*, 4484–4495.
- [110] Kang, H. J.; Ali, R. F.; Paul, M. T.; Radford, M. J.; Andreu, I.; Lee, A. W.; Gates, B. D. Tunable functionalization of silica coated iron oxide nanoparticles achieved through a silanol-alcohol condensation reaction. *Chem. Commun.* **2019**, *55*, 10452–10455.

- [111] Nguyen, T. T.; Lau-truong, S.; Mammeri, F. Star-Shaped $\text{Fe}_{3-x}\text{O}_4$ -Au Core-Shell Nanoparticles : From Synthesis to SERS Application. *Nanomaterials* **2020**, *10*, 1–13.
- [112] Kim, D. J.; Park, S. G.; Kim, D. H.; Kim, S. H. SERS-Active-Charged Microgels for Size- and Charge-Selective Molecular Analysis of Complex Biological Samples. *Small* **2018**, *14*, 1–10.
- [113] Gloag, L.; Mehdipour, M.; Chen, D.; Tilley, R. D.; Gooding, J. J. Advances in the Application of Magnetic Nanoparticles for Sensing. *Adv. Mater.* **2019**, *31*, 1–26.
- [114] Liu, S.; Mei, J.; Zhang, C.; Zhang, J.; Shi, R. Synthesis and magnetic properties of shuriken-like nickel nanoparticles. *J. Mater. Sci. Technol.* **2018**, *34*, 836–841.
- [115] Fouad, D. M.; El-Said, W. A.; Mohamed, M. B. Spectroscopic characterization of magnetic Fe_3O_4 @Au core shell nanoparticles. *Spectrochim. Acta - Part A Mol. Biomol. Spectrosc.* **2015**, *140*, 392–397.
- [116] Brennan, G.; Thorat, N. D.; Pescio, M.; Bergamino, S.; Bauer, J.; Liu, N.; Tofail, S. A.; Silien, C. Spectral drifts in surface textured Fe_3O_4 -Au, core-shell nanoparticles enhance spectra-selective photothermal heating and scatter imaging. *Nanoscale* **2020**, *12*, 12632–12638.
- [117] Yan, X.; Yu, H.; Guo, Z.; Wu, C.; Wang, S.; Li, B.; Yan, B.; Yin, H. One-pot synthesis of Au- Fe_2O_3 @ SiO_2 core-shell nanoreactors for CO oxidation. *New J. Chem.* **2020**, *44*, 5661–5665.
- [118] Oliveira-Filho, G. B.; Atoche-Medrano, J. J.; Aragón, F. F.; Mantilla Ochoa, J. C.; Pacheco-Salazar, D. G.; da Silva, S. W.; Coaquira, J. A. Core-

- shell Au/Fe₃O₄ nanocomposite synthesized by thermal decomposition method: Structural, optical, and magnetic properties. *Appl. Surf. Sci.* **2021**, *563*, 1–6.
- [119] Senthil, V. P.; Gajendiran, J.; Raj, S. G.; Shanmugavel, T.; Ramesh Kumar, G.; Parthasaradhi Reddy, C. Study of structural and magnetic properties of cobalt ferrite (CoFe₂O₄) nanostructures. *Chem. Phys. Lett.* **2018**, *695*, 19–23.
- [120] Khizar, S.; Ahmad, N. M.; Ahmed, N.; Manzoor, S.; Hamayun, M. A.; Naseer, N.; Tenório, M. K.; Lebaz, N.; Elaissari, A. Aminodextran coated CoFe₂O₄ nanoparticles for combined magnetic resonance imaging and hyperthermia. *Nanomaterials* **2020**, *10*, 1–16.
- [121] Gupta, N.; Jain, P.; Rana, R.; Shrivastava, S. Current Development in Synthesis and Characterization of Nickel Ferrite Nanoparticle. *Mater. Today Proc.* **2017**, *4*, 342–349.
- [122] Amulya, M. A.; Nagaswarupa, H. P.; Kumar, M. R.; Ravikumar, C. R.; Prashantha, S. C.; Kusuma, K. B. Sonochemical synthesis of NiFe₂O₄ nanoparticles: Characterization and their photocatalytic and electrochemical applications. *Appl. Surf. Sci. Adv.* **2020**, *1*, 100023.
- [123] Sharifianjazi, F.; Moradi, M.; Parvin, N.; Nemati, A.; Jafari Rad, A.; Sheysi, N.; Abouchenari, A.; Mohammadi, A.; Karbasi, S.; Ahmadi, Z.; Esmailkhanian, A.; Irani, M.; Pakseresht, A.; Sahmani, S.; Shahedi Asl, M. Magnetic CoFe₂O₄ nanoparticles doped with metal ions: A review. *Ceram. Int.* **2020**, *46*, 18391–18412.
- [124] Jauhar, S.; Kaur, J.; Goyal, A.; Singhal, S. Tuning the properties of cobalt ferrite: A road towards diverse applications. *RSC Adv.* **2016**, *6*, 97694–97719.

- [125] Liu, X.; Yang, X.; Li, K.; Liu, H.; Xiao, R.; Wang, W.; Wang, C.; Wang, S. Sensors and Actuators B: Chemical Fe₃O₄-@Au SERS tags-based lateral flow assay for simultaneous detection of serum amyloid A and C-reactive protein in unprocessed blood sample. *Sensors Actuators B. Chem.* **2020**, *320*, 128350.
- [126] He, H.; Sun, D.; Pu, H.; Huang, L. Bridging Fe₃O₄@Au nanoflowers and Au@Ag nanospheres with aptamer for ultrasensitive SERS detection of a flatoxin B1. *Food Chem.* **2020**, *324*, 127443.
- [127] Podolak, K.; Buckser, E.; Qudsi, Z.; Salvamoser, I.; Tiwari, K. Plasmon resonance studies of iron coated gold films with and without an applied magnetic field. *AIP Adv.* **2017**, *7*.
- [128] Zhou, X.; Li, X.; Li, S.; An, G. W.; Cheng, T. Magnetic Field Sensing Based on SPR Optical Fiber Sensor Interacting with Magnetic Fluid. *IEEE Trans. Instrum. Meas.* **2019**, *68*, 234–239.

Co-authorship Statement

Stephanie Gallant is the major contributor to the works reported in this document, including (but not limited to): research plans and goals, synthesis of materials, designing and fabrication of sensing surfaces, and sensing tests. Results and discussions for all chapters, including data visualization and analysis, were also completed by S. Gallant. E. Merschrod provided feedback on experiments and writing.

Contributions of co-authors includes the following:

In Chapter 2, GC-MS data and analysis of the PW was completed by L. Whelan and L. Stewart, as were PW tests on the substrates. The extraction details found in the corresponding Supplementary Information (Appendix A) were also written by L. Whelan and L. Stewart.

The initial document writing for Chapter 3 was completed by S. Gallant and L. Whelan, and all figures were made by S. Gallant. This documentation was then reworded by the legal team at BERESKIN & PARR LLP to the syntax/format required for patent submission. The documents were then revised through several iterations, including responses to the patent examiners (patent agents), by S. Gallant.

Chapter 4 was completed in full by S. Gallant, including all data collection, visualization, interpretation, and writing.

Chapter 5 was written in its entirety by S. Gallant. NPs for scaling reproducibility tests, directed by S. Gallant, were created by L. Strelnikova, O. Daini, E. Connors,

and S. Clarke. All substrates, NP characterization, data collection, LOD testing, and data interpretation was completed by S. Gallant. All NPs used in substrate fabrication were additionally made by S. Gallant.

Chapter 2

Hierarchical magnetic films for high-performing plasmonic sensors*

Hierarchically structured films comprise a growing section of the field of surface-enhanced Raman spectroscopy (SERS). Here we report a novel, powerfully-enhancing hierarchical plasmonic substrate featuring patterned multi-layers of magnetic iron oxide nanospheres, using an external magnetic field to create sets of radial ridges. This new substrate allows for effective analyte adsorption and significant Raman signal enhancement, thanks to the contribution of both the magnetic and plasmonic components to the electromagnetic hotspots. We demonstrate significant and reliable Raman enhancement for polycyclic aromatic hydrocarbons (PAHs), dilute but persistent environmental pollutants, in a complex and real-world matrix of produced water (PW). The substrate's activity for PAHs is validated by gas chromatography-mass spectrometry analysis. An impressive signal-to-noise ratio (SNR) of several dB enables detection of analyte below 1 ppm. This multi-layer magnetic film sensor sub-

*This chapter is a reformatted version of "Hierarchical magnetic films for high-performing plasmonic sensors", Stephanie M. V. Gallant, Liam D. Whelan, Lucas D. Stewart, and Erika F. Mer-schrod S, *Langmuir* 2021, 37, 48, 14043–14049.

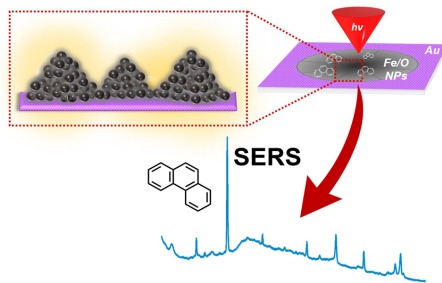


Figure 2.1: A novel plasmonic surface utilizing patterned multi-layers of magnetic nanoparticles as the forefront enhancement material for SERS

strate shows remarkable stability and robustness suitable for real-world applications, while boasting simple methods and strong potential to scale up fabrication.

2.1 Introduction

Sensing devices relying on solid-state films or layers are of great interest to many industries, as they are versatile and robust for detecting in many phases.¹ Though a large body of solid state sensor research investigates gas-phase sensing, aqueous-phase sensing is of great interest as well.^{2,3} Metal oxides have been studied in many contexts including such sensors,⁴ as they are an accessible class of materials with many interesting optical and physical properties, particularly at the nanoscale.^{1,5}

In this work, we report a facile and effective optoelectronic sensor design featuring magnetically-patterned nanoparticle multi-layered film as the predominant sensing material, boasting strong enhancement and analyte adhesion. This fabrication method offers an accessible way to create structure on the nano-to-micro scale for surfaces.

As magnetic materials can be influenced by external magnetic fields, the location of particles can be controlled and predicted by understanding the field of any external magnet used. By using a permanent magnet to generate the externally-applied field,

we therefore have the ability to control where the particles deposit across our sensing surface, lending to an overall hierarchical patterning with serial layering.

This methodology allows for simpler and quicker formation of reliable films, as compared to traditional fabrication methods such as layer-by-layer assembly or photolithography.^{6,7} Without the difficulties of these methods, including issues with scaling-up or uniformity, our design allows for substrate fabrication with strong potential for scaling while using simple instrumentation. Additionally, by varying the geometry of the external magnetic field, one could achieve new patterns which may provide advantages in molecule adhesion or plasmonic enhancement.

One major hurdle in functional sensor design is successful detection in the presence of a complex matrix.^{8,9} Samples beyond the lab are often part of complex environmental systems, containing hundreds to thousands of different molecules in a small amount of sample. The device must have the capability to selectively sense the molecule(s) of interest over other structures present, along with additional sensing challenges like low-level detection (sensitivity) or robustness of use.^{8,10}

We demonstrate the practical detection of phenanthrene, a common polycyclic aromatic hydrocarbon (PAH) and persistent environmental pollutant,¹¹ both in lab tests and with samples obtained from offshore platform waters. Multi-ringed and conjugated organic structures, PAHs are major byproducts of various oil & gas processes, additionally forming a host of derivative structures from their parent molecules.^{12,13} Due to their stability and bio-accumulative nature, this class of molecules and their derivatives are of major concern to health, as they are known carcinogens, endocrine disruptors, and neurotoxins.¹²⁻¹⁴

These molecules are of high importance for sensing and monitoring, but pose challenges for detection in the aforementioned complex matrices of the environment.¹⁵ Optical sensing offers lower costs and simpler methods than those associated with mass

spectrometry, thus development of specialized surfaces for these organic analytes is imperative for practical usage. Furthermore, our ability to measure analytes in a complex matrix removes the need for the sample purification or separation required for other detection methods, further reducing costs.

2.2 Experimental

2.2.1 Materials

Iron(II) chloride tetrahydrate ($\geq 99\%$), iron(III) chloride hexahydrate ($\geq 99\%$), and (3-aminopropyl)triethoxysilane (APTES, $\geq 99\%$) were purchased from Sigma Aldrich (Oakville, Ontario, Canada). Concentrated hydrochloric acid and sulfuric acid were purchased from Fisher Scientific (Ottawa, Ontario, Canada). Concentrated ammonium hydroxide solution was purchased from ACP Chemicals (Montreal, Quebec, Canada). N_2 and Ar (ultra-high purity) was purchased from Praxair Canada. Distilled and filtered nanopure water was obtained from a Barnstead 18.2 $M\Omega \cdot cm$ system. All chemicals were used without further purification.

2.2.2 Iron Oxide Nanoparticle Synthesis

The magnetic iron oxide nanoparticles (NPs) were prepared by the Massart¹⁶ method of pH-mediated coprecipitation, under N_2 ,¹⁷⁻¹⁹ with a total iron molar concentration of 50 mmol. A 3:2 molar ratio of Fe^{3+}/Fe^{2+} accounts for some expected oxidation of the 2+ ion due to any latent oxygen present.^{20,21}

To create the NPs, 8.11 g of $FeCl_3 \cdot 6 H_2O$ and 3.99 g of $FeCl_2 \cdot 4 H_2O$ were dissolved in 50 mL of a prepared 2 M HCl solution under constant stirring, at around 80 °C, inside a glovebox under N_2 . Once salts had dissolved to give a clear brown solution, concentrated NH_4OH was slowly (around 0.5 mL/sec) added to the reaction vessel

to approach a solution pH of 11. Black-brown particles began to precipitate out of solution around a pH of 9, with amounts increasing as the pH was raised. These products were stirred in solution for up to 1 hr, at which point they were taken from heat and neutralized with HCl until a pH of 7 was obtained.

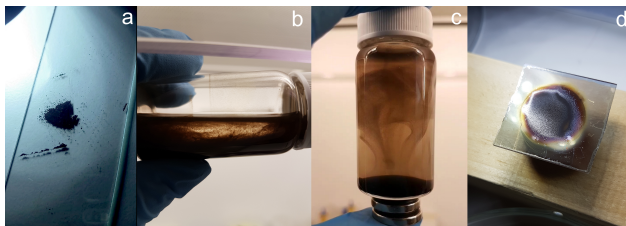


Figure 2.2: Photos of (a) bulk NPs showing their dark brown-black colour, easily distinguishable from red hematite, (b) Suspension of NPs, (c) NPs being collected with a magnet. (d) Near-finished substrate, with the solvent evaporating from the last NP layer addition, resting on the magnet used for patterning.

Once neutralized, the NPs were triple washed with nanopure water, followed by three washes with 95% ethanol, to ensure all counter-ions were removed. A magnet was used to collect the product for each solvent decanting step, as seen in panel c of Figure 2.2. The NPs were then stored in ethanol.

In order to prevent oxidation^{19,22} outside of the N₂ environment, the magnetic iron oxide NPs were capped by adding 1 mL of prepared NP suspension to 50 mL of ethanol while stirring and heating gently. Once mixed, 100 μ L of organosilane (APTES) were added to the reaction vessel quickly. This mixture was allowed to stir and heat for 2 hours, at which point the product was removed and washed again as described above.

2.2.3 Substrate Fabrication Method

To prepare the substrate base layer, plain glass microscope slides (Technologist ChoiceTM, 75 mm x 26 mm x 1 mm) were cut into thirds with a diamond scribe (SPI Supplies). These cut slides were then put through an acid-washing procedure,

first sitting in an approximately 40 °C concentrated HCl bath for 5-10 mins and then in a concentrated H₂SO₄ bath at the same temperature for another 5-10 mins, with nanopure water rinses in between. The washed slides were then rinsed with ethanol and submerged in ethanol until ready for use.

To create the plasmonic metal layer of the substrate, the washed slides were removed from ethanol, rinsed again with ethanol, and dried using compressed air. They were then placed in a single layer on the stage of a Quorum Technologies K550X Sputter Coater with a gold target (Soquelec model number K550X Au target: 60 mm diameter Au disk, 0.1 mm thickness), and argon was pumped through. The slides were then coated for 1 minute at a current of 20 mA, corresponding to a deposited gold thickness of around 5 nm.

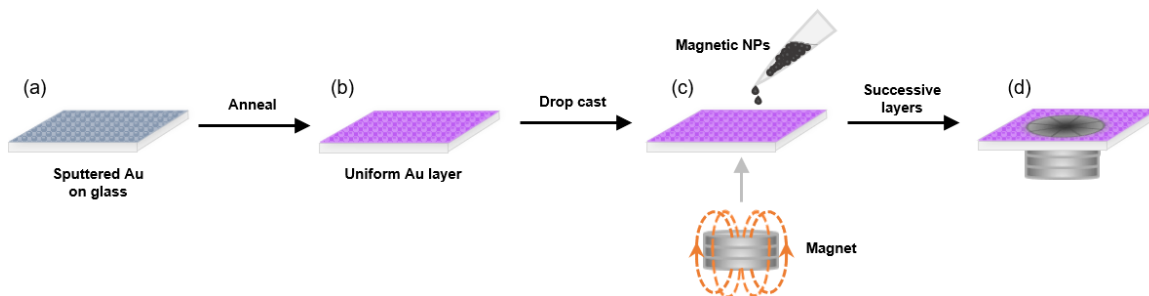


Figure 2.3: Schematic showing components of the working substrate. Starting with (a) roughly sputtered gold on glass in, this layer is then annealed (b) to allow for a more uniform layer. Once the gold is prepared, (c) magnetic NPs in solution are added with a magnet below the glass to control the particles, resulting in patterning of the dried layers which follow the magnetic field lines of the external magnet. (d) Successive layers are built up, and additions are repeated until a sufficient number of layers have been added.

Once coated, the gold slides were placed in a Thermo Scientific Lindberg Blue M tube furnace and annealed for 2 hours at 300 °C. Before annealing, the slides appeared blue-grey (Figure 2.3a) and afterwards appeared pink-purple (Figure 2.3b).

While a number of layer addition methods were attempted to create the metal oxide layers, they proved to be unsuccessful for these NPs. Classic methods of film

creation were attempted, including spin-coating, dip-coating, passive layer-by-layer assembly in solution, and drop-casting. Due to a combination of van der Waals (vdW) interactions and the magnetic characteristics of the NPs,^{22,23} these methods created uneven, patchy films with little reproducibility. Attempts at functionalizing the NPs with terminal thiols to allow for favourable interactions with the base gold layer created additional problems with surface activity, and as such, this method was subsequently discontinued.

The substrate with gold was ultimately placed on top of a stack of neodymium alloy disk magnets (stack of three disks, each with dimensions 18 mm \times 3 mm), where layers of NP suspension were added successively (Figure 2.3c-d). The NP suspension was sonicated (Fisher Scientific FS20) for 30 minutes to prepare for these layer additions, in order to disperse the particles and prevent avoidable aggregation. Layers of a 3 mg/mL NP suspension were added 20 μ L at a time until the fluorescence of the glass present in the Raman spectrum was quenched, where iron oxide peaks instead became dominant.

As the NPs in solution moved under the influence of an external magnetic field (Figure 2.2c), the patterning of the dried multi-layers followed the direction of field lines. A substrate in fabrication, towards the end of these layer additions, can be seen in Figure 2.2d. The layered NPs form a distinct pattern, featuring a micron-scale radial distribution of particles, like spokes on a wheel, seen under optical magnification in Figure 2.4.



Figure 2.4: Stitched optical microscope images taken at 20x across the patterned surface, showing the NP pattern that formed under the influence of an external magnetic field and remains once the field is removed. (Multiple scale bars digitally removed and replaced with single set.)

2.2.4 Characterization

For characterization of the solid products themselves, thin layers of the NP suspensions (as-synthesized or capped) were deposited on glass under N₂ atmosphere and allowed to dry. These layers were then scraped off and collected into sealed containers, until they were removed for various analysis methods (Figure 2.2a).

Powder X-ray diffraction (pXRD) data were collected from 20° to 80° 2 θ using a Rigaku Ultima IV X-Ray diffractometer with a Cu-K α source. **Raman spectroscopy** of the NPs, analyte, and substrates was performed using a Renishaw InVia confocal Raman system with an 830 nm diode laser source, coupled with a Leica DM2700 microscope, whose camera also provided the optical micrographs. All Raman spectra were collected at 3.0 ± 0.3 mW (1% power) due to sample sensitivity.^{18,24} **Scanning electron microscopy (SEM)** was utilized to analyze sizes and shapes of the particles with a JEOL JSM-7100F Scanning Electron Microscope, which was also equipped to perform particle elemental analysis by **energy-dispersive X-ray spectroscopy (EDX)**. Samples were prepared for electron beam analysis by carbon coating a 2 nm layer, and probe voltages were kept at 15 kV during imaging with a working distance of 12 mm. **Vibrating sample magnetometry (VSM)** was performed to study the magnetic properties of the particles, using a MicroSense EZ vibrating sample magnetometer (VSM), where data was collected across a field of ± 20 kOe at 25 °C.

2.2.5 Substrate Testing Method

Once sufficient iron oxide NP layers were added, the substrate was exposed to an analyte solution. (See section S3 in the SI[†] for details about the PW sample.) Around 0.5 mL of solution was dropped onto the substrate surface using a pipette and then

allowed to air dry at room temperature. Once dry, the substrate was immediately analyzed via Raman spectroscopy as described in section 2.2.4.

2.3 Results and Discussion

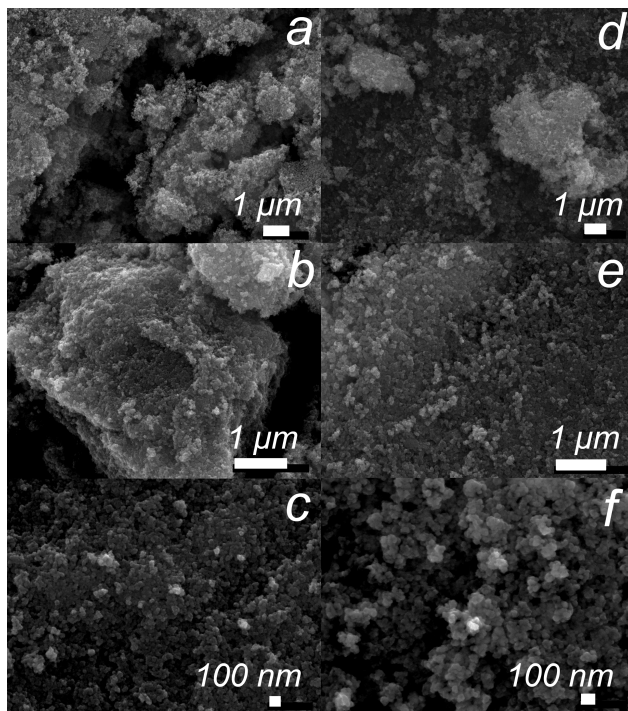


Figure 2.5: SEM images of (a-c) as-synthesized iron oxide NPs and (d-f) APTES-capped NPs. As seen in (a), (b), (d) and (e), the particle sizes and shapes are consistent across each sample. The higher magnification in (c) and (f) show a size range of 30-60 nm for both capped and uncapped NPs.

2.3.1 Determining Properties of Synthesized Nanoparticles

Figure 2.5 shows the expected spherical particles, which range from 30-60 nm in size. The NPs had a tendency to cluster, even after physical grinding, which could partly be attributed to their magnetic properties.²² The NPs remained suspended for some time after sonication or shaking (Figure 2.2(b)), but they eventually did settle

out, as they were not a true ferrofluid containing any surfactant to promote colloidal behaviour.^{21,25}

This aggregation within suspension was not an issue during substrate preparation: The particles were agitated through sonication immediately before layer additions to break up large clusters. Alternate NP sizing was also attempted via dynamic light scattering (DLS; see SI for details), but agglomeration meant that the DLS data was inconclusive.

The pXRD analysis (Figure 2.6) confirmed the formation of cubic inverse spinels matching the diffraction patterns of both magnetite and maghemite, as identified through comparison with JCPDS 19-629 and JCPDS 39-1346 respectively,²⁶ along with literature references.²⁷⁻²⁹ Hematite can readily form and remain a stable byproduct with high crystallinity from the synthesis, but pXRD data showed no evidence of hematite in the samples, indicating the successful preparation of the desired magnetic NPs.

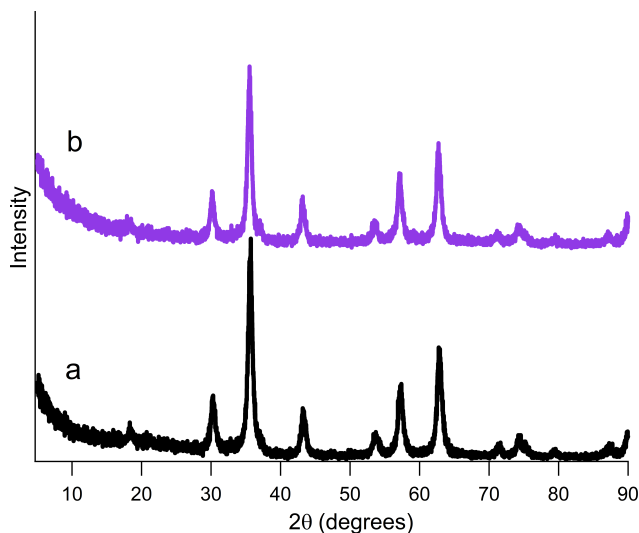


Figure 2.6: X-ray diffraction patterns for (a) as-synthesized iron oxide NPs and (b) APTES-capped NPs confirm the expected cubic inverse spinel crystal structure. A comparison of (a) and (b) shows that the silane coating does not alter the structure of the NPs.

As pXRD cannot readily distinguish magnetite from maghemite, Raman spectroscopy was also used to characterize the NPs. Raman not only provides information about bonds and their vibrations, but also gives insight into local crystal environments, being sensitive enough to distinguish atom substitutions or vacancies in lattice sites.^{24,29,30}

Raman spectra of the solid products seen in Figure 2.7c show three broad peaks at 348 cm^{-1} , 500 cm^{-1} , and 670 cm^{-1} which are characteristic of cubic inverse spinel ferrites.^{24,31} The 348 cm^{-1} band corresponds to an E_g mode of symmetric O-Fe-O bending, while the band at 500 cm^{-1} is a T_{2g} mode from asymmetric Fe-O bending.³² The final and most intense peak at 670 cm^{-1} is an A_{1g} mode resulting from symmetric O-Fe-O stretches.

Shifting of specific bands gives insight into the proportion of magnetite/maghemite character, as well as lattice defects or substitutions.^{32,33} The 670 cm^{-1} A_{1g} mode of the experimental product matches with the most commonly reported values for magnetite, as it would instead shift closer to 700 cm^{-1} in maghemite.^{24,27,32} However, the peak intensity of the product's A_{1g} mode is not as pronounced as in pure magnetite references, suggesting only partial magnetite composition of this experimental sample.^{27,33} The other two visible Raman active modes, E_g and T_{2g} at 348 cm^{-1} and 500 cm^{-1} , correspond with peak locations of those modes in maghemite.^{29,34} This Raman evidence in full, along with pXRD confirmation, shows a mixture with both magnetite and maghemite present.

Once the structure was confirmed as mixed magnetic iron oxides, VSM analysis was performed to understand the magnetic character of the NPs. As the proposed use of these NPs in a device would be under ambient conditions, measurements were carried out at $25\text{ }^\circ\text{C}$. Figure 2.8 shows the response of the NPs as the magnetic field is swept from -20 kOe to $+20\text{ kOe}$, displaying the expected hysteresis for magnetic

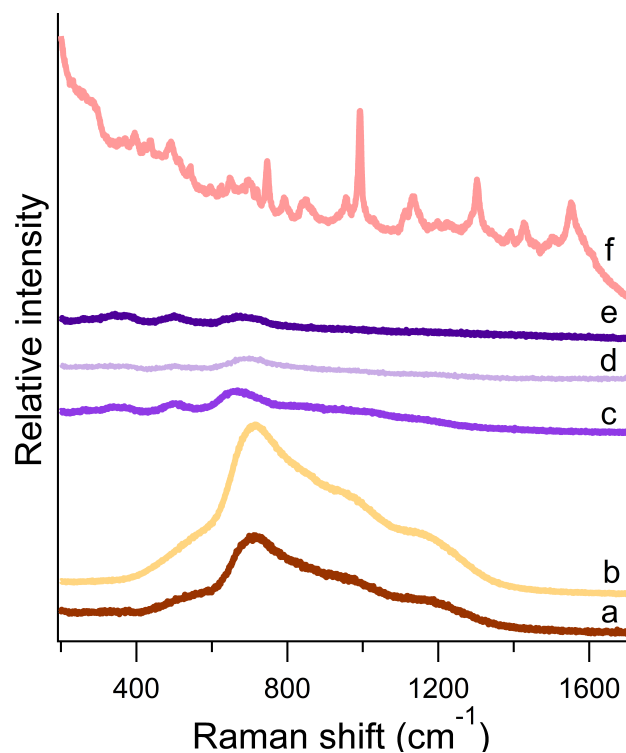


Figure 2.7: Raman spectra highlighting the importance of the composite substrate including hierarchically patterned NPs, through a series of control experiments. The 5 nm annealed gold layer in (a), as well as that same layer exposed to 1 ppm of analyte (b), show significant fluorescence in their spectra. Spectra (c-e) all show nanoparticle peaks dominating for each case: unpatterned nanoparticles on a blank glass surface (c), patterned nanoparticles on glass (no gold) exposed to analyte (d), and non-patterned NPs on top of annealed gold exposed to analyte (e). Spectrum (f) shows a successful and strong enhancement of analyte on the working substrate, with magnetically patterned NP multi-layers on top of annealed gold.

iron oxides. The saturation magnetisation (M_S) values for the NPs, noted by the plateauing tails starting around ± 10 kOe, were 60 emu/g for the uncapped NPs and 49 emu/g for the APTES-capped.

2.3.2 Sensor Design Focused on Magnetic Films

This SERS design differs from others which utilize magnetic NPs, in that our NPs are at the forefront of this sensing platform with the classic plasmonic material as a background contributor. The NPs are an essential component for the function of this

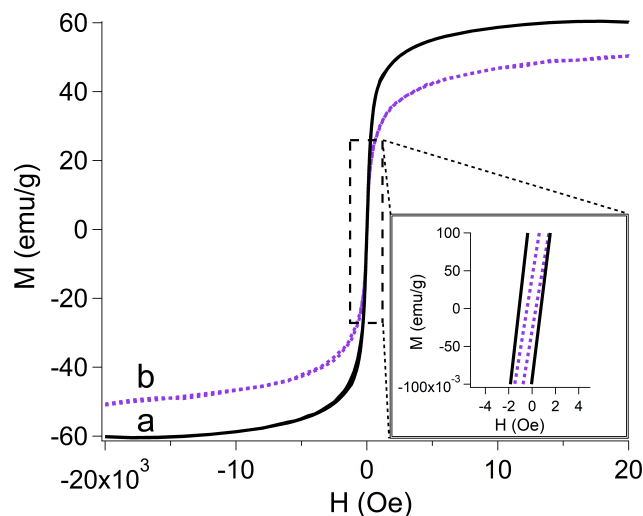


Figure 2.8: Magnetic character shown via VSM hysteresis loops for (a) as-synthesized plain NPs and (b) APTES-capped NPs. Capped NPs show a slight drop in saturation magnetization from the plain NPs, but both exhibit comparable magnetic coercivity and remanence (inset).

sensor, and are not simply used for mobility in solution as reported previously.^{10,35,36}

As described in section 2.2.3, layers of the magnetic NPs proved challenging to reproducibly create using traditional methods. The prevailing success of using magnetic fields in layer creation allowed for multi-layers to be built up in a controlled and reliable fashion. By adding micro-additions in solution and allowing the solvent to evaporate with each layer, the magnetic NPs deposit on the field lines and remain secure once dried. A substrate towards the end of fabrication can be seen in Figure 2.2d.

The profile of the final substrate results in a “wheel-and-spoke” radial patterning, as seen in Figure 2.4. The gaps between the hills of NPs are around 10-20 μm while the heights vary, with maximum heights around 40 μm and the majority being 5-20 μm . The gaps allow for the annealed gold thin film underneath to show through, while the complex hierarchical topography of the NPs also allow many locations for the analytes to settle on the surface.

Gold is the plasmonically active base of the sensor, which has been well studied in such a role.^{37–39} The gold in this design proves essential in providing additional plasmonic activity, working together with the NPs in combined surface enhancement. However, it is important to note that gold does not account for the entire enhancement effect seen in the final composite substrate. In addition to its plasmonic activity, the layer of gold also serves as a barrier between the glass slide and the analyte solution.

To demonstrate that the NPs contribute to surface enhancement on the substrate, and that the patterning of these magnetic NPs is essential, we performed a number of control experiments, isolating each feature. All components were tested on their own and in various combinations to determine their importance. Figure 2.7 shows that as individual components, the gold (a, b) and the NPs (c-e) do not provide sufficient enhancement to overcome fluorescence or their own Raman signal, respectively. Moreover, the presence of non-patterned NPs on gold is not sufficient for enhancement, as seen in the lack of analyte peaks in the spectrum displayed in Figure 2.7e. When the gold is combined with the patterned multi-layers of NPs as seen in Figure 2.7f, analyte peaks dominate the spectrum.

Furthermore, the material comprising the patterned surface impacts performance. A substrate was stored for 4 years under ambient conditions, without any temperature or environment control, allowing it to naturally oxidize with time. The resulting new oxide which formed was predominantly γ -FeO(OH), as confirmed by Raman spectroscopy (SI, Figure A.6)), while the patterning of the surface remained as before. Since this oxy-hydroxide is not a magnetic iron oxide, this new version of the patterned surface is a magnetically-inert analogue to the reported working surface. After analyte exposure at 1 ppm, the converted surface does not display enhancement of the expected phenanthrene peaks. This implicates the ferrimagnetic forms of iron oxides as crucial to the performance of the SERS substrate.

Additionally it is important to note that in order to obtain enhancement, the laser focus must be within the NP multi-layers, and not on the reflective gold surface below (SI, Figure A.4)). This further proves that the gold is not the sole plasmonic contributor, as plasmonic enhancement is a short range and local effect, and the collection of our Raman data occurs multiple microns off of the base surface.

Through rigorous Raman testing, we have determined that there is no preferential enhancing location on the NP surface (SI, Figure A.5)). Though the centre and edges of the substrate show differences in macroscale patterning (Figure 2.4) due to the field line path coming from the cylindrical magnet stack, the local environment of alternating stacks of NPs and Au showing through remains consistent across the substrate. The enhancement locations are not dependent on a certain large-scale orientation of the NP stacks themselves: The signal is comparable across the substrate, and it is not affected by macroscale patterning differences.

To quantify enhancement on this surface, signal-to-noise ratio (SNR) calculations were performed (see SI for details). As opposed to enhancement factor (EF) calculations, which compare separate Raman and SERS spectra, our SNR calculations allow for direct comparison of enhancement peaks to continuous baseline noise. This allows us to clearly assess signal strength of the enhanced Raman spectra, without any solvent or surface-comparison issues innate to EF methods.⁴⁰ Our complex structured film has SNRs of 2.9 dB and above at the ppm level, and these SNRs are consistently high across replicates of our substrates (SI, Figure A.5)).

A 2.9 dB of SNR represents nearly three orders of magnitude of signal over baseline noise. The peak itself is many orders of magnitude larger than it would be without enhancement, since we cannot detect the peak at all on the equivalent non-magnetic (non-SERS-active) substrate. Herein lies the challenge with EF calculations: they rely on comparison of different systems, extrapolating an enhancement over a hypothetical

non-SERS system. The SNR is a practical indicator of detection ability: even a signal 100 times lower would still be clearly detectable above the baseline.

One potential source of signal enhancement in nanostructured surfaces is simply the increased surface area relative to a flat substrate, allowing for more analytes to bind. This increased surface area does not explain the enhancement of our surfaces. The patterned surface is about 25% larger than the corresponding unpatterned surface. The unpatterned surface does not show any enhancement (Figure 2.7e), while the patterned surface does. Furthermore, the surface mentioned above that is patterned but no longer magnetic has the same surface area as the original patterned surface, and it does not show any enhancement either.

As this substrate is proposed for detecting PAHs in aqueous systems, we performed tests using a sample of produced water obtained from an offshore oil platform. The sample was first analyzed using gas chromatography coupled with a mass-spectrometer (GC-MS), performed for two separate extraction techniques (see SI for details). While GC-MS analysis showed that there were hundreds of compounds present (SI, Table A.1)), our surface was selective for the desired multi-ringed hydrocarbons over various long-chained molecules. There is a preference for these PAHs due to a number of factors, including the van der Waals forces between surface and adsorbates, the high hydrophobicity of the PAHs, and their high symmetry.¹⁵

Along with its successful performance as a cost-effective sensor, our platform also boasts a practical longevity. Once the magnetic NPs are successfully capped with an inert layer, they are stable upwards of one year in solution, or longer as a dried layer on a substrate. The sensor has potential to function in an archival manner once exposed, particular if stored with consideration to ambient temperature and oxygen of the environment.

2.4 Conclusions

In summary, we introduce a novel sensor design using magnetic nanoparticles to create hierarchical films for use as optoelectronic sensors. Direction of particles using an external magnetic field creates complex layers reliably, via successive micro-additions of the particles in fluid. This resulting patterned multi-layer film provides an abundance of sites for analyte binding, and the patterned gaps in the multi-layer allow access to the gold base layer as an additional plasmonic contributor. Rigorous testing shows each component of the sensor are necessary for optimal function.

By working with a solid-state sensing platform design, sample loading is straightforward and fast, while the sensor itself is stable and physically robust. This composite substrate offers longevity on the scale of > 1 year, with this shelf-life applying to both pre- and post-exposure to analytes.

Our magnetic film sensor results in impressive signal, with SNR of 2.9 dB and above. The signal we obtain is particularly significant when noting that our testing analyte is phenanthrene, an environmental PAH of concern, not a high-signal molecule like crystal violet or rhodamine 6G. Coupled with our successful testing in complex matrices showing selectivity for PAHs over other organics, the whole of our reported results are promising for future uses of such patterned magnetic multi-layer films in sensing devices.

2.5 Acknowledgement

This research was conducted on the island of Newfoundland, the ancestral homeland of the Beothuk and the unceded ancestral and current land of the Mi'kmaq. The authors thank the Natural Science and Engineering Council of Canada (NSERC, DG program) for operating funds, the Canada Foundation for Innovation (CFI) for instrumentation

funding, the Research and Development Corporation of Newfoundland and Labrador (RDC-NL, Arctic Tech program) for salaries for LDW and LDS, and the School of Graduate Studies of Memorial University of Newfoundland for a stipend for SMVG. We also thank Prof. K. Poduska (Physics) for access to the VSM, Garrett McDougall for AFM data collection, and Dr. W. Aylward (CREAIT) for access to the SEM and EDX, sample preparation for SEM, EDX and pXRD, and for operation of the XRD facility.

Bibliography

- [1] Korotcenkov, G. Metal oxides for solid-state gas sensors: What determines our choice? *Mater. Sci. Eng. B Solid-State Mater. Adv. Technol.* **2007**, *139*, 1–23.
- [2] O’Hare, D.; Parker, K. H.; Winlove, C. P. Metal-metal oxide pH sensors for physiological application. *Med. Eng. Phys.* **2006**, *28*, 982–988.
- [3] Uria, N.; Abramova, N.; Bratov, A.; Muñoz-Pascual, F. X.; Baldrich, E. Miniaturized metal oxide pH sensors for bacteria detection. *Talanta* **2016**, *147*, 364–369.
- [4] Kaur, N.; Singh, M.; Comini, E. One-Dimensional Nanostructured Oxide Chemoresistive Sensors. *Langmuir* **2020**, *36*, 6326–6344.
- [5] Shiohara, A.; Wang, Y.; Liz-Marzán, L. M. Recent approaches toward creation of hot spots for SERS detection. *J. Photochem. Photobiol. C Photochem. Rev.* **2014**, *21*, 2–25.
- [6] Ai, B.; Yu, Y.; Möhwald, H.; Zhang, G.; Yang, B. Plasmonic films based on colloidal lithography. *Adv. Colloid Interface Sci.* **2014**, *206*, 5–16.

- [7] Yu, Y.; Zhang, G. In *Updat. Adv. Lithogr.*; Hosaka, S., Ed.; InTech, 2013; Chapter Colloidal, pp 3–34.
- [8] Szlag, V. M.; Rodriguez, R. S.; He, J.; Hudson-Smith, N.; Kang, H.; Le, N.; Reineke, T. M.; Haynes, C. L. Molecular Affinity Agents for Intrinsic Surface-Enhanced Raman Scattering (SERS) Sensors. *ACS Appl. Mater. Interfaces* **2018**, *10*, 31825–31844.
- [9] Mei, H.; Zhao, X.; Bai, S.; Li, Q.; Xia, J.; Bai, H.; Cheng, L. Tuning SERS properties of pattern-based MWNTs-AuNPs substrates by adjustment of the pattern spacings. *Carbon N. Y.* **2018**, *136*, 38–45.
- [10] Gloag, L.; Mehdipour, M.; Chen, D.; Tilley, R. D.; Gooding, J. J. Advances in the Application of Magnetic Nanoparticles for Sensing. *Adv. Mater.* **2019**, *31*, 1–26.
- [11] Wang, C.; Zou, X.; Li, Y.; Zhao, Y.; Song, Q.; Yu, W. Pollution levels and risks of polycyclic aromatic hydrocarbons in surface sediments from two typical estuaries in China. *Mpb* **2016**, *114*, 917–925.
- [12] Murawski, A.; Roth, A.; Schwedler, G.; Schmied-Tobies, M. I.; Rucic, E.; Plum, N.; Scherer, M.; Scherer, G.; Conrad, A.; Kolossa-Gehring, M. Polycyclic aromatic hydrocarbons (PAH) in urine of children and adolescents in Germany – human biomonitoring results of the German Environmental Survey 2014–2017 (GerES V). *Int. J. Hyg. Environ. Health* **2020**, *226*, 113491.
- [13] Nováková, Z.; Novák, J.; Kitanovski, Z.; Kukučka, P.; Smutná, M.; Wietzorek, M.; Lammel, G.; Hilscherová, K. Toxic potentials of particulate and gaseous air pollutant mixtures and the role of PAHs and their derivatives. *Environ. Int.* **2020**, *139*, 105634.

- [14] Roslund, M. I. et al. Endocrine disruption and commensal bacteria alteration associated with gaseous and soil PAH contamination among daycare children. *Environ. Int.* **2019**, *130*, 104894.
- [15] Du, J.; Jing, C. Preparation of Thiol Modified Fe₃O₄@Ag Magnetic SERS Probe for PAHs Detection and Identification. *J. Phys. Chem. C* **2011**, *115*, 17829–17835.
- [16] Massart, R. Preparation of Aqueous Magnetic Liquids in Alkaline and Acidic Media. *IEEE Trans. Magn.* **1981**, *17*, 1247–1248.
- [17] Lee, J.; Mulmi, S.; Thangadurai, V.; Park, S. S. Magnetically Aligned Iron Oxide/Gold Nanoparticle-Decorated Carbon Nanotube Hybrid Structure as a Humidity Sensor. *ACS Appl. Mater. Interfaces* **2015**, *7*, 15506–15513.
- [18] Giuntini, D.; Torresani, E.; Chan, K. T.; Blankenburg, M.; Saviot, L.; Bor, B.; Domènech, B.; Shachar, M.; Mueller, M.; Olevsky, E.; Garay, J.; Schneider, G. A. Iron oxide-based nanostructured ceramics with tailored magnetic and mechanical properties: development of mechanically robust, bulk superparamagnetic materials. *Nanoscale Adv.* **2019**, *1*, 3139–3150.
- [19] Schwaminger, S. P.; Bauer, D.; Fraga-García, P.; Wagner, F. E.; Berensmeier, S. Oxidation of magnetite nanoparticles: impact on surface and crystal properties. *CrystEngComm* **2017**, *19*, 246–255.
- [20] Karaagac, O.; Kockar, H. A simple way to obtain high saturation magnetization for superparamagnetic iron oxide nanoparticles synthesized in air atmosphere : Optimization by experimental design. *J. Magn. Magn. Mater.* **2016**, *409*, 116–123.

- [21] Maity, D.; Agrawal, D. C. Synthesis of iron oxide nanoparticles under oxidizing environment and their stabilization in aqueous and non-aqueous media. *J. Magn. Magn. Mater.* **2007**, *308*, 46–55.
- [22] Wu, W.; Wu, Z.; Yu, T.; Jiang, C.; Kim, W.-S. Recent progress on magnetic iron oxide nanoparticles: synthesis, surface functional strategies and biomedical applications. *Sci. Technol. Adv. Mater.* **2015**, *16*, 023501.
- [23] Torre, B.; Bertoni, G.; Fragouli, D.; Falqui, A.; Salerno, M.; Diaspro, A.; Cingolani, R.; Athanassiou, A. Magnetic force microscopy and energy loss imaging of superparamagnetic iron oxide nanoparticles. *Sci. Rep.* **2011**, *1*, 1–8.
- [24] Dar, M. I.; Shivashankar, S. A. Single crystalline magnetite, maghemite, and hematite nanoparticles with rich coercivity. *RSC Adv.* **2014**, *4*, 4105–4113.
- [25] Durdureanu-Angheluta, A.; Pricop, L.; Stoica, I.; Peptu, C. A.; Dascalu, A.; Marangoci, N.; Doroftei, F.; Chiriac, H.; Pinteala, M.; Simionescu, B. C. Synthesis and characterization of magnetite particles covered with α -triethoxysilil-polydimethylsiloxane. *J. Magn. Magn. Mater.* **2010**, *322*, 2956–2968.
- [26] *PDF-4+ 2019*; ICDD: Newtown Square, PA, 2019.
- [27] Rebodos, R. L.; Vikesland, P. J. Effects of oxidation on the magnetization of nanoparticulate magnetite. *Langmuir* **2010**, *26*, 16745–16753.
- [28] Pang, Y. L.; Lim, S.; Ong, H. C.; Chong, W. T. Research progress on iron oxide-based magnetic materials: Synthesis techniques and photocatalytic applications. *Ceram. Int.* **2016**, *42*, 9–34.
- [29] Ma, J.; Chen, K. Modulated self-reversed magnetic hysteresis in iron oxides. *Sci. Rep.* **2017**, *7*, 1–7.

- [30] Liang, K.; Hui, L. S.; Turak, A. Probing the multi-step crystallization dynamics of micelle templated nanoparticles: Structural evolution of single crystalline γ -Fe₂O₃. *Nanoscale* **2019**, *11*, 9076–9084.
- [31] Chourpa, I.; Douziech-Eyrolles, L.; Ngaboni-Okassa, L.; Fouquenot, J. F.; Cohen-Jonathan, S.; Soucé, M.; Marchais, H.; Dubois, P. Molecular composition of iron oxide nanoparticles, precursors for magnetic drug targeting, as characterized by confocal Raman microspectroscopy. *Analyst* **2005**, *130*, 1395–1403.
- [32] Shebanova, O. N.; Lazor, P. Raman spectroscopic study of magnetite (FeFe₂O₄): A new assignment for the vibrational spectrum. *J. Solid State Chem.* **2003**, *174*, 424–430.
- [33] Lee, N.; Schuck, P. J.; Nico, P. S.; Gilbert, B. Surface Enhanced Raman Spectroscopy of Organic Molecules on Magnetite (Fe₃O₄) Nanoparticles. *J. Phys. Chem. Lett.* **2015**, 970–974.
- [34] Chaudhari, N. S.; Warule, S. S.; Muduli, S.; Kale, B. B.; Jouen, S.; Lefez, B.; Hannoyer, B.; Ogale, S. B. Maghemite (hematite) core (shell) nanorods via thermolysis of a molecular solid of Fe-complex. *Dalton Trans.* **2011**, *40*, 8003–8011.
- [35] Leung, K. C.-F.; Xuan, S.; Zhu, X.; Wang, D.; Chak, C.-P.; Lee, S.-F.; Ho, W. K.-W. K.-W.; Chung, B. C.-T. C.-T. Gold and iron oxide hybrid nanocomposite materials. *Chem. Soc. Rev.* **2012**, *41*, 1911.
- [36] Song, D.; Yang, R.; Long, F.; Zhu, A. Applications of magnetic nanoparticles in surface-enhanced Raman scattering (SERS) detection of environmental pollutants. *J. Environ. Sci.* **2018**, 1–20.
- [37] Plascencia-Villa, G.; Torrente, D.; Marucho, M.; José-Yacamán, M. Biodirected

- synthesis and nanostructural characterization of anisotropic gold nanoparticles. *Langmuir* **2015**, *31*, 3527–3536.
- [38] Quaresma, P.; Osório, I.; Dória, G.; Carvalho, P. A.; Pereira, A.; Langer, J.; Araújo, J. P.; Pastoriza-Santos, I.; Liz-Marzán, L. M.; Franco, R.; Baptista, P. V.; Pereira, E. Star-shaped magnetite@gold nanoparticles for protein magnetic separation and SERS detection. *RSC Adv.* **2014**, *4*, 3690–3698.
- [39] Brennan, G.; Thorat, N. D.; Pescio, M.; Bergamino, S.; Bauer, J.; Liu, N.; To-fail, S. A.; Silien, C. Spectral drifts in surface textured Fe₃O₄-Au, core-shell nanoparticles enhance spectra-selective photothermal heating and scatter imaging. *Nanoscale* **2020**, *12*, 12632–12638.
- [40] Rodrigues, D. C.; De Souza, M. L.; Souza, K. S.; Dos Santos, D. P.; Andrade, G. F.; Temperini, M. L. Critical assessment of enhancement factor measurements in surface-enhanced Raman scattering on different substrates. *Phys. Chem. Chem. Phys.* **2015**, *17*, 21294–21301.

Chapter 3

Substrate with Magnetic Layer for SERS, Methods for their Preparation and Uses Thereof *

Note: Much of this text is phrased in a legalese, verbose way, as per professional legal documentation. Some common phrasing and their meanings include:

| Example phrasing | Meanings |
|--|----------------------------|
| "Schematic of an exemplary embodiment" | Illustration of |
| "A person skilled in the art" | Scientist in this field |
| "In an embodiment" | For example; In some cases |

This work covers methods outlined in Chapters 2 and 4.

*This chapter contains the text of Canadian patent application CA03118007, which is based on US Patent 62/751,776 (filed 2018, publication date 2022-01-13, no. US-2022-0011234-A1), which was the subject of Patent Cooperation Treaty (PCT) number PCT/CA2019/051518 (filing date 2019-10-28), with International Publication Number WO2020/087157.

Abstract

The present application relates, for example, to substrates for surface enhanced Raman spectroscopy (SERS), to methods for their preparation and to uses of such SERS substrates in methods for the detection of an analyte in a sample. The SERS substrates of the present application comprise a support material, a layer of a SERS-active metal on the support material, and a layer of magnetically active nanoparticles on the layer of the SERS-active metal. The methods of preparing such SERS substrates comprise depositing a layer of a SERS-active metal on a support material, and depositing a layer of magnetically active nanoparticles on the layer of the SERS-active metal.

3.1 Description

3.1.1 Cross-reference to related applications

[0001] The present application claims the benefit of priority from co-pending U.S. provisional application no. 62/751,776 filed on October 29, 2018, the contents of which are incorporated herein by reference in their entirety.

[0002] The present application relates to substrates for surface enhanced Raman spectroscopy (SERS), to methods for their preparation and to uses of such SERS substrates in methods for the detection of an analyte in a sample.

3.1.2 Background

[0003] Traditionally, the most sensitive and robust methods for organic contamination in water have been chromatographic methods such as gas chromatography-mass

spectrometry (GC-MS). This technique excels, for example, at complete speciation and quantification. However, it is a technically demanding analytical method which also requires significant sample preparation time. In some industries such as the oil production industry, complete speciation of the water has been sacrificed in lieu of speed and ease of detection.

[0004] In the offshore oil industry in Newfoundland and Labrador, real time monitoring is employed as a first line detection method using fluorescence- based spectroscopic methods. However, a significant drawback to fluorescence measurements is that there is no chemical speciation occurring, i.e. the individual components present in the observed waste stream are not able to be identified prior to discharge. A second method that is employed is an ultraviolet-visible (UV- Vis) photospectroscopic method that also suffers from a lack of specificity.

[0005] Surface enhanced Raman scattering (SERS) can provide structural information about an analyte and can permit trace analyses due to enhancement of Raman scattering of compounds which are adsorbed to certain surfaces. Such SERS substrates have included magnetic core-shell sensors (i.e. nanoparticles with a core made up of magnetic/iron oxide) having a plasmonic material shell and layered structures comprising a plasmonic material deposited as the frontier layer over a base layer of nanoparticles. Other SERS substrates are known which comprise, for example, rough metal surfaces or nanostructures.

[0006] For example, US 9,134,247 discloses a method and apparatus comprising a first SER-active material, of which a support structure is comprised and a second SER-active material comprising a liquid reagent. An analyte- specific binding agent is attached to at least one of the first or second SER- active material. The method comprises adding the analyte sample to one (or both) of the functionalized SER-active

materials then adding the liquid reagent (second SER-active material) to the support structure (first SER-active material) such that the SER-active materials are attached to the target analyte. US 8,149,397 discloses nanostructured SERS probes that are in the form of a spherical, asymmetrical tapered metallic shell having a round opening surrounded by an edge that can optionally comprise layers of different metals e.g. of gold and iron. US 7,242,470 discloses SERS substrates which can comprise a metal film over a nanostructured layer. US 8,003,408 discloses SERS active particles which include a gold nanoparticle coated with very fine iron oxide nanoparticles.

3.1.3 Summary

[0007] In contrast to prior SERS substrates, the SERS substrates of the present application employ a magnetic top layer which enhances signal through a magnetic field and promotes adhesion of certain classes of compounds that may, for example, be advantageous for using such SERS based materials for organic contamination analysis. Lab trials have indicated that the SERS substrates prepared in the present examples had a high affinity towards the types of organic contamination which are of significant industrial concern due to regulatory and compliance requirements. The SERS substrates may, for example, be competitive in cost, speed and ease of analysis, while also offering rich speciation which may afford an end user more overall information regarding their production system and/or their waste water discharge.

[0008] Accordingly, the present application includes a substrate for surface enhanced Raman spectroscopy (SERS), comprising:

- a support material;
- a layer of a SERS-active metal on the support material; and
- a layer of magnetically active nanoparticles on the layer of the SERS-active metal.

[0009] The present application also includes a method of preparing a substrate for surface enhanced Raman spectroscopy (SERS), comprising:

- depositing a layer of a SERS-active metal on a support material; and
- depositing a layer of magnetically active nanoparticles on the layer of the SERS-active metal.

[0010] The present application also includes a use of a SERS substrate of the present application for detecting and/or quantifying an analyte as well as a method for detecting an analyte in a sample, the method comprising:

- contacting a SERS substrate of the present application with the sample to adhere the analyte to the SERS substrate;
- obtaining a SERS spectrum of the analyte adhered to the SERS substrate; and
- analyzing the spectrum to detect the analyte.

[0011] Other features and advantages of the present application will become apparent from the following detailed description. It should be understood, however, that the detailed description and the specific examples while indicating embodiments of the application are given by way of illustration only, since various changes and modifications within the spirit and scope of the application will become apparent to those skilled in the art from this detailed description.

3.2 Brief Description of the Drawings

[0012] The present application will now be described in greater detail with reference to the drawings in which:

[0013] Figure 3.1 is a schematic of an exemplary embodiment of a SERS substrate of

the present application in use with a Raman spectrometer.

[0014] Figure 3.2 is a schematic of an exemplary embodiment of a method for detecting an analyte in a sample of the present application comprising submerging at least a portion of a SERS substrate of the present application in the sample.

[0015] Figure 3.3 is a schematic of an exemplary embodiment of a method for detecting an analyte in a sample of the present application comprising depositing at least a portion of the sample onto a SERS substrate of the present application.

[0016] Figure 3.3 shows the Raman spectra of a substrate with increasing layers of iron oxide nanoparticles deposited thereon (from top to bottom: 60, 80, 100, 120, 140, 160, 180, 200, 220 and 240 μL of iron oxide nanoparticle suspension added) according to embodiments of the present application.

[0017] Figure 3.5 shows SERS spectra obtained of a 1 ppm phenanthrene solution from five different spots of a SERS substrate that it was deposited on according to an embodiment of the present application.

[0018] Figure 3.6 shows SERS spectra obtained using a SERS substrate according to an embodiment of the present application pre-exposure (***) and post-exposure (****) to offshore oil produced water in comparison to a blank (*) and exposure to a 1 ppm phenanthrene solution (**).

[0019] Figure 3.7 shows SERS spectra of two SERS substrates prepared according to embodiments of the present application using 160 μL (*) and 140 μL iron oxide nanoparticles (**) exposed to 1 ppm phenanthrene, compared to a Raman spectrum of bulk (solid) phenanthrene (***).

[0020] Figure 3.8 shows SERS spectra obtained using a SERS substrate according to

an embodiment of the present application pre-exposure and post- exposure (*) to a 1 ppm phenanthrene solution.

[0021] Figure 3.9 shows SERS spectra obtained of a 1 ppm phenanthrene solution from four different spots of a SERS substrate that it was deposited on according to an embodiment of the present application.

3.3 Detailed Description

3.3.1 Definitions

[0022] Unless otherwise indicated, the definitions and embodiments described in this and other sections are intended to be applicable to all embodiments and aspects of the present application herein described for which they are suitable as would be understood by a person skilled in the art.

[0023] In understanding the scope of the present application, the term “comprising” and its derivatives, as used herein, are intended to be open ended terms that specify the presence of the stated features, elements, components, groups, integers, and/or steps, but do not exclude the presence of other unstated features, elements, components, groups, integers and/or steps. The foregoing also applies to words having similar meanings such as the terms, “including”, “having” and their derivatives. The term “consisting” and its derivatives, as used herein, are intended to be closed terms that specify the presence of the stated features, elements, components, groups, integers, and/or steps, but exclude the presence of other unstated features, elements, components, groups, integers and/or steps. The term “consisting essentially of”, as used herein, is intended to specify the presence of the stated features, elements, components, groups, integers, and/or steps as well as those that do not materially affect

the basic and novel characteristic(s) of features, elements, components, groups, integers, and/or steps.

[0024] Terms of degree such as “substantially”, “about” and “approximately” as used herein mean a reasonable amount of deviation of the modified term such that the end result is not significantly changed. These terms of degree should be construed as including a deviation of at least 5% of the modified term if this deviation would not negate the meaning of the word it modifies.

[0025] The term “and/or” as used herein means that the listed items are present, or used, individually or in combination. In effect, this term means that “at least one of” or “one or more” of the listed items is used or present.

[0026] As used in this application, the singular forms “a”, “an” and “the” include plural references unless the content clearly dictates otherwise.

[0027] The term “suitable” as used herein means that the selection of specific reagents or conditions will depend on the reaction being performed and the desired results, but none-the-less, can generally be made by a person skilled in the art once all relevant information is known.

[0028] The term “produced water” as used herein refers to waste water generated during the production of oil and/or natural gas. Produced water may include water from the reservoir, water that has been injected into the formation and/or chemicals added during production/treatment. Produced water may include organic compounds such as various polycyclic aromatic hydrocarbons (PAHs), BTEX (benzene, toluene, ethylbenzene and xAene), triterpanes, ketones, saturated hydrocarbons, phenols and/or organic acids which may be detectable by SERS.

[0029] The term “magnetically active” as used herein in reference to nanoparticles

refers to nanoparticles that are ferrimagnetic or ferromagnetic and does not include nanoparticles that are diamagnetic, paramagnetic or antiferromagnetic.

[0030] The term “alkyl” as used herein, whether it is used alone or as part of another group, means straight or branched chain, saturated alkyl groups. The term C₁₋₆alkyl means an alkyl group having 1, 2, 3, 4, 5 or 6 carbon atoms.

3.3.2 SERS Substrates and Methods for the Preparation Thereof

[0031] Highly sensitive magnetically active SERS substrates have been prepared that may, for example, be capable of detecting a wide variety of Raman-active compounds such as common organic pollutants in water used during industrial processes. The SERS substrates have been used to detect organic contamination present in laboratory simulated solutions (1 ppm phenanthrene) and raw produced water samples (sourced from a local oil production platform). The SERS substrates prepared and tested were made up of a 5 nm gold (Au⁰) film which was deposited onto a well-cleaned glass slide via a metal sputtering system. The Au film was then thermally annealed for 2 hours at 300 °C to serve as the sensor enhancement layer of the SERS substrate. The adhesion layer of the SERS substrate was formed by sequential deposition of portions of organosilane capacitated ferrimagnetic iron nanoparticles (FeNPs) of approximately 30-60 nm diameter, or uncapped ferrimagnetic cobalt iron oxide nanoparticles (CoFeNPs), where the majority was approximately 30-60 nm diameter, with some particles being 100-300 nm. Deposition thickness was monitored via Raman spectroscopy until underlying glass slide fluorescence was quenched via nanoparticle (NP) addition. This resulted in the sensing device composed of a glass slide with a Au⁰ film enhancement layer covered via a magnetic nanoparticle adhesion layer. This

represents an inversion of a typical SERS substrate which has the metal enhancement layer as the top layer of the device.

[0032] Accordingly, the present application includes a substrate for surface enhanced Raman spectroscopy (SERS), comprising: a support material; a layer of a SERS-active metal on the support material; and a layer of magnetically active nanoparticles on the layer of the SERS-active metal.

[0033] The support material is any suitable support material. For example, the person skilled in the art would appreciate that a suitable support material is a solid material that would not significantly affect the overall plasmonic behaviour of the layer of the SERS-active metal and is advantageously robust enough to be handled by means such as tweezers, by hand or with a robotic instrument. In an embodiment, the support material comprises, consists essentially of or consists of glass, plastic, silicon or highly oriented pyrolytic graphite (HOPG). In an embodiment, the support material comprises, consists essentially of or consists of glass or plastic. In another embodiment of the present application, the support material comprises, consists essentially of or consists of glass.

[0034] The support material (probe) can be of any shape or dimension as long as it has a flat area of at least 1 mm² coated with the layers of SERS-active metal and magnetically active nanoparticles. The thickness of the support material can be any suitable thickness may result. In an embodiment of the present application, the support material has a thickness of from about 1.0 mm to about 1.2 mm.

[0035] The SERS substrate tested in the examples of the present application used gold as the SERS active metal. However, other metals such as platinum, silver and copper may also be suitable alternatives in that they have demonstrated SERS properties.

Accordingly, in some embodiments, the SERS-active metal is gold, platinum, silver or copper. In another embodiment of the present application, the SERS-active metal is gold.

[0036] The thickness of the layer of the SERS-active metal may, for example, depend on the detector. For example, based on an 830 nm detector, a layer in the range of about 2.5 nm to about 30 nm would be suitable. Accordingly, in an embodiment, the layer of the SERS-active metal has a thickness of from about 2.5 nm to about 30 nm. In another embodiment of the present application, the layer of the SERS-active metal has a thickness of about 2.5 nm to about 20 nm or about 2.5 nm to about 7.5 nm. In a further embodiment, the layer of the SERS-active metal has a thickness of about 5 nm.

[0037] The SERS substrates tested in the examples of the present application used ferrimagnetic iron oxide or cobalt iron oxide nanoparticles. However, other suitable ferrimagnetic or ferromagnetic nanoparticles may also be used. In an embodiment, the magnetically active nanoparticles comprise iron oxide. In another embodiment of the present application, the magnetically active nanoparticles are ferrimagnetic iron (II,III) oxide nanoparticles, ferrimagnetic iron (III) oxide (γ form) nanoparticles or ferrimagnetic cobalt iron oxide nanoparticles. In another embodiment, the magnetically active nanoparticles are ferrimagnetic iron oxide nanoparticles or cobalt iron oxide nanoparticles. In a further embodiment, the magnetically active nanoparticles are ferrimagnetic iron oxide nanoparticles. In another embodiment, the magnetically active nanoparticles are ferrimagnetic cobalt iron oxide nanoparticles.

[0038] The person skilled in the art would readily appreciate that as the diameter of the magnetically active nanoparticles is varied, this will have an effect on the plasmonic behaviour of the material. For example, if the material has poor light absorption, a

significant decrease in enhancement or potentially loss of detectable SERS activity. Additionally, at sizes of greater than 100 nm, additional properties of the particles themselves will be altered. Accordingly, in an embodiment, the magnetically active nanoparticles have an average diameter of about 100 nm or less. In another embodiment, the magnetically active nanoparticles have an average diameter of from about 30 nm to about 60 nm.

[0039] In some embodiments, the magnetically active nanoparticles are capped. For example, in embodiments wherein the magnetically active nanoparticles are comprised of a material which may undergo oxidation under the conditions in which the SERS substrate would be stored or used, capping of the nanoparticles may reduce or prevent such oxidation such that magnetism is substantially maintained. The magnetically active nanoparticles can be capped by any suitable capping reagent. For example, a person skilled in the art would readily understand that the capping agent doesn't interfere with the magnetic properties or reactivity of the magnetically active nanoparticles. In the examples described herein below, (3-aminopropyl)triethoxysilane was demonstrated to be a suitable capping agent for the iron oxide nanoparticles. In contrast, in similar experiments, (3-mercaptopropyl)trimethoxysilane was found not to be a suitable capping agent. Accordingly, in some embodiments, the capping agent is amine-terminated. In some embodiments, the capping agent is devoid of a mercapto group. In some embodiments, for example, in the case of iron oxide nanoparticles or similar nanoparticles, the capping reagent can have a siloxy functional group which can undergo hydrolysis such that the silane moiety binds to the surface of the nanoparticles via an $-\text{OSi}$ bond, and optionally self-hydrolyze on the surface of the nanoparticles to provide a multilayer coating on the nanoparticles. In an embodiment, the siloxy functional group has the formula $-\text{Si}(\text{OR}^{\text{A}})_3$ wherein each R^{A} is independently C_{1-6} alkyl. In another embodiment, each R^{A} is ethyl. In another embodiment, the

capping reagent further comprises a primary amine functional group. In another embodiment, the capping agent has the formula $\text{H}_2\text{N}-(\text{CH}_2)_n-\text{Si}(\text{OR}^A)_3$ wherein n is an integer of from between 2 and 10 and R^A is as defined herein. In another embodiment, n is 3. In a further embodiment, the magnetically active nanoparticles are capped by (3-aminopropyl)triethoxysilane. In alternative embodiments, the magnetically active nanoparticles are uncapped.

[0040] In an embodiment, the layer of the magnetically active nanoparticles has a thickness such that a Raman spectrum of the SERS substrate does not show any detectable bands corresponding to the support material.

[0041] In an embodiment, the SERS substrate is configured for use in a handheld Raman spectrometer, a portable Raman spectrometer or a benchtop Raman spectrometer. In another embodiment, the substrate is configured for use in a handheld Raman spectrometer or a portable Raman spectrometer. A person skilled in the art could readily configure the SERS substrate for use in various Raman spectrometers, for example, based on the focal length of the probe (i.e. the distance between the substrate and the device for a particular spectrometer).

[0042] The present application also includes a method of preparing a substrate for surface enhanced Raman spectroscopy (SERS), comprising: depositing a layer of a SERS-active metal on a support material; and depositing a layer of magnetically active nanoparticles on the layer of the SERS-active metal.

[0043] The SERS- active metal can be deposited on the support material by any suitable means. In an embodiment, the SERS-active metal is deposited on the support material by a method comprising thermal evaporation or sputtering. In another embodiment, the SERS-active metal is deposited on the support material by a method

comprising sputtering. In another embodiment of the present application, the method further comprises annealing the SERS-active metal prior to depositing the layer of the magnetically active nanoparticles thereon.

[0044] In an embodiment, the layer of magnetically active nanoparticles is deposited on the layer of the SERS-active metal by a method comprising: depositing a portion of a suspension comprising magnetically active nanoparticles and a solvent on the layer of SERS-active metal; evaporating the solvent; and repeating the depositing and evaporating until a layer of magnetically active nanoparticles of a desired thickness has been deposited on the layer of SERS-active metal.

[0045] The deposition of the suspension can be carried out by any suitable means, the selection of which can be made by a person skilled in the art. In an embodiment, the portion is an aliquot of from about 10 μL to about 30 μL or about 20 μL of the suspension. In another embodiment, the method further comprises using a suitable strong permanent magnet (for example, a suitable rare-earth magnet such as a neodymium permanent magnet) beneath the support material during the deposition of the suspension and evaporation. In an embodiment, the strong permanent magnet is a neodymium permanent magnet.

[0046] In an embodiment, the desired thickness is such that a Raman spectrum of the SERS substrate does not show any detectable bands corresponding to the support material.

[0047] In some embodiments, the method further comprises capping the magnetically active nanoparticles to obtain capped magnetically active nanoparticles prior to deposition on the layer of the SERS-active metal. For example, in embodiments wherein the magnetically active nanoparticles are comprised of a material which may

undergo oxidation under the conditions in which the SERS substrate would be stored or used, capping of the nanoparticles may reduce or prevent such oxidation such that magnetism is substantially maintained. In an embodiment, the magnetically active nanoparticles are capped by a method comprising mixing a suspension comprising the magnetically active nanoparticles in a suitable solvent (e.g. ethanol) with a suitable amount of a capping agent (e.g. APTES) under suitable conditions to obtain the capped magnetically active nanoparticles. In an embodiment, the conditions comprise agitating (e.g. stirring) the mixture of the magnetically active nanoparticle suspension and the capping agent for a time and at a temperature for the capping to be complete, for example, in the case of APTES or a similar capping agent, a time of from about 1 hour to about 6 hours or about 2 hours at a temperature of about 60 °C to about 100 °C or about 80 °C. In alternative embodiments, the method is devoid of a capping step.

[0048] It will be appreciated by a person skilled in the art that embodiments relating to the SERS substrates in the methods for preparing the SERS substrates of the present application can be varied as described herein for the embodiments of the SERS substrates of the present application.

[0049] For example, in an embodiment of the methods for preparing the SERS substrates, the magnetically active nanoparticles are ferrimagnetic iron oxide nanoparticles having an average diameter of about 100 nm or less. In an embodiment, the magnetically active nanoparticles are ferrimagnetic iron oxide nanoparticles having an average diameter of from about 30 nm to about 60 nm. In another embodiment, the magnetically active nanoparticles are ferrimagnetic cobalt iron oxide nanoparticles, wherein the majority of the magnetically active nanoparticles have a diameter of about 100 nm or less. In an embodiment, the magnetically active nanoparticles are

ferrimagnetic cobalt iron oxide nanoparticles, wherein the majority of the magnetically active nanoparticles have a diameter of from about 30 nm to about 60 nm. In an embodiment, the magnetically active nanoparticles are ferrimagnetic cobalt iron oxide nanoparticles, wherein at least about 70% of the magnetically active nanoparticles have a diameter of about 100 nm or less. In an embodiment, the magnetically active nanoparticles are ferrimagnetic cobalt iron oxide nanoparticles, wherein at least about 75% of the magnetically active nanoparticles have a diameter of about 100 nm or less. In an embodiment, the magnetically active nanoparticles are ferrimagnetic cobalt iron oxide nanoparticles, wherein the at least about 70% of the magnetically active nanoparticles have a diameter of from about 30 nm to about 60 nm. . In an embodiment, the magnetically active nanoparticles are ferrimagnetic cobalt iron oxide nanoparticles, wherein the at least about 75% of the magnetically active nanoparticles have a diameter of from about 30 nm to about 60 nm.

[0050] It will be appreciated by a person skilled in the art that the diameter of the magnetically active nanoparticles may be affected by the reaction conditions, for example, the temperature of the reaction and/or scaling the reaction up or down wherein, for example, reaction vessel size could be a factor.

[0051] In another embodiment, the SERS active metal is gold.

[0052] The present application also includes a substrate for surface enhanced Raman spectroscopy (SERS) prepared by a method for preparing a substrate for surface enhanced Raman spectroscopy (SERS) of the present application.

3.3.3 Uses and Methods for Detecting an Analyte

[0053] SERS substrates were prepared that were made up of a glass slide with a

gold film enhancement layer that was subsequently covered with a magnetic iron nanoparticle adhesion layer. This represented an inversion of a typical SERS substrate which has the enhancement layer as the top layer of the device. The SERS substrates of the present application can be used in conjunction with an optical based Raman spectroscope to measure various compounds of interest adhered to the sensing surface. The SERS substrates are low cost, disposable and may, for example be used for rapid and accurate detection of organic contamination present, for example in waste water streams.

[0054] Accordingly, the present application also includes a use of a SERS substrate of the present application for detecting and/or quantifying an analyte.

[0055] The present application also includes a method for detecting an analyte in a sample, the method comprising: contacting a SERS substrate of the present application with the sample to adhere the analyte to the SERS substrate; obtaining a SERS spectrum of the analyte adhered to the SERS substrate; and analyzing the spectrum to detect the analyte.

[0056] It will be appreciated by the skilled person that embodiments relating to the SERS substrates in the uses and methods for detecting and/or quantifying an analyte in a sample of the present application can be varied as described herein for the embodiments of the SERS substrates of the present application.

[0057] It will be appreciated by a person skilled in the art that the SERS spectrum is obtained via a suitable Raman spectrometer, for example a handheld or portable instrument or a more traditional benchtop Raman instrument. Figure 3.1 shows a schematic of an exemplary embodiment of a SERS substrate of the present application 10 comprising a support material 12, a layer of a SERS-active metal 14 on the support

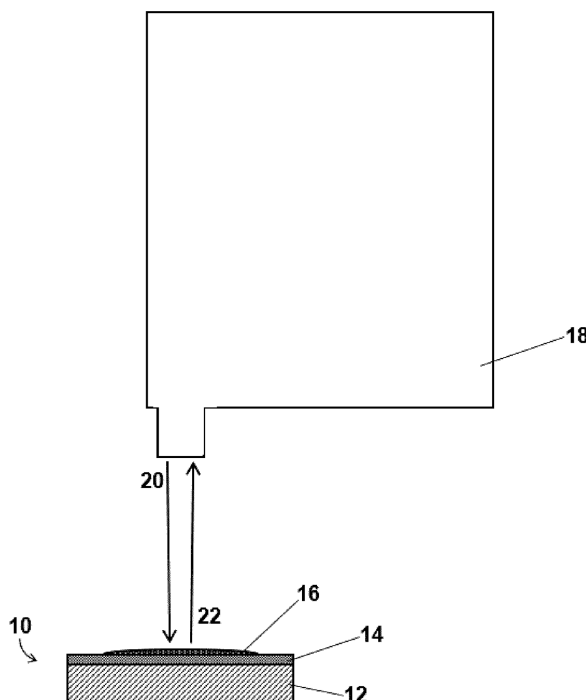


Figure 3.1: Schematic of an exemplary embodiment of a SERS substrate of the present application in use with a Raman spectrometer.

material 12 and a layer of magnetically active nanoparticles 16 on the layer of the SERS-active metal 14 with a sample deposited thereon (not shown) in use with a Raman spectrometer 18. Referring to Figure 3.1, a laser beam 20 travels to the SERS substrate, light interacts with the sample and the light with a new energy 22 is collected in the detector of the Raman spectrometer 18. A handheld or portable Raman system may be advantageous, for example, due to its mobility and/or smaller laboratory footprint (i.e. a handheld instrument will take up less valuable space in a lab setting). There would be, however, no significant difference in the data collected from either type of instrument. Accordingly, in an embodiment, the SERS spectrum is obtained using a handheld Raman spectrometer, a portable Raman spectrometer or a benchtop Raman spectrometer. In another embodiment of the present application, the SERS spectrum is obtained using a handheld Raman spectrometer or a portable Raman spectrometer.

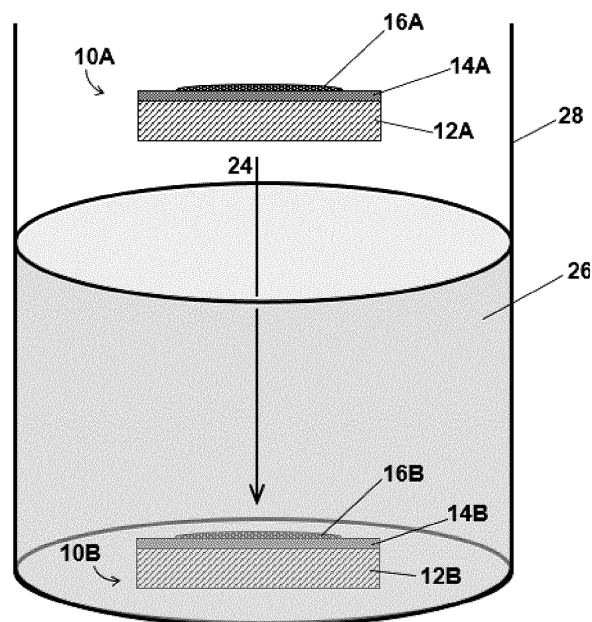


Figure 3.2: Schematic of an exemplary embodiment of a method for detecting an analyte in a sample of the present application comprising submerging at least a portion of a SERS substrate of the present application in the sample.

[0058] The SERS substrates of the present application can be advantageously used to detect analytes without the need for complex and/or time-consuming sample preparation. In an embodiment, the contacting comprises submerging at least a portion, optionally all of the SERS substrate in the sample followed by drying to adhere the analyte to the SERS substrate. Figure 3.2 shows a schematic of an exemplary embodiment wherein the contacting comprises submerging at least a portion of the SERS substrate in the sample. Referring to Figure 3.2, in the embodiment shown therein, a SERS substrate of the present application (10A, 10B) comprising a support material (12A, 12B), a layer of a SERS-active metal (14A, 14B) on the support material (12A, 12B) and a layer of magnetically active nanoparticles (16A, 16B) on the layer of the SERS-active metal (14A, 14B) is fully submerged 24 in the sample 26 which is housed in a suitable vessel 28. In an embodiment, the at least a portion of the SERS substrate is submerged in the sample for a time of up to about ten minutes.

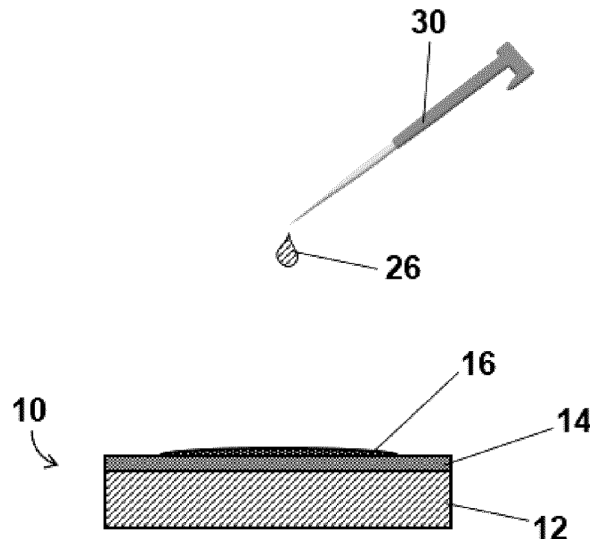


Figure 3.3: Schematic of an exemplary embodiment of a method for detecting an analyte in a sample of the present application comprising depositing at least a portion of the sample onto a SERS substrate of the present application.

In an alternative embodiment, the contacting comprises depositing the sample on at least a portion of the SERS substrate followed by drying to adhere the analyte to the SERS substrate. Figure 3.3 shows a schematic of an exemplary embodiment wherein the contacting comprises depositing the sample on at least a portion of the SERS substrate. Referring to Figure 3.3, in the embodiment shown therein, a portion of the sample 26 is deposited by a suitable means 30 onto a SERS substrate of the present application 10 comprising a support material 12, a layer of a SERS-active metal 14 on the support material 12 and a layer of magnetically active nanoparticles 16 on the layer of the SERS-active metal 14. The drying is not shown in Figures 2 or 3. The drying is carried out by any suitable means, the selection of which can be made by a person skilled in the art. In an embodiment, the drying is carried out under ambient conditions. In another embodiment, the conditions for drying further comprise the use of a fan to accelerate evaporation.

[0059] In an embodiment, the spectrum is obtained by placing the SERS active sub-

strate with the analyte adhered thereto in the path of a Raman laser and acquiring the spectrum in a wavenumber range of from about 200 cm^{-1} to about 2000 cm^{-1} . Such a spectral acquisition typically takes about three minutes to complete. Acquiring spectra from multiple spots on the surface of the SERS substrate may, for example, provide a more accurate sense of the analyte(s) in the sample. Accordingly, in another embodiment, the spectrum is acquired from a plurality (e.g. three) locations on the surface of the SERS substrate. In another embodiment, the analyzing comprises comparing the Raman shifts of the spectrum to a library of known Raman shifts to identify the analyte in the sample.

[0060] In an embodiment, the spectra is sent electronically to a separate location for analysis. In an embodiment, the analysis is qualitative. In another embodiment of the present application, the analysis is quantitative.

[0061] In an embodiment, the method further comprises obtaining a SERS spectrum of a SERS substrate without analyte adhered thereto to obtain a blank spectrum then subtracting the blank spectrum from the SERS spectrum obtained of the analyte adhered to the SERS substrate.

[0062] In an embodiment, the analyte is a known analyte or has been identified and the analyzing comprises: calculating the peak area of a diagnostic peak in the spectrum; and comparing the calculated peak area to a calibration curve of peak areas for that diagnostic peak as a function of concentration of analyte to quantify the amount of the analyte in the sample.

[0063] In another embodiment, the sample comprises an unknown analyte and the analyzing comprises: adding a desired amount of a stock solution comprising a known concentration of a known analyte to the sample; calculating the peak area of a di-

agnostic peak in the spectrum for the known analyte, calculating the peak area of a diagnostic peak for the unknown analyte, and comparing the calculated peak area of the unknown analyte to the peak area of the known analyte to quantify the amount of the unknown analyte in the sample.

[0064] The SERS substrates of the present application may be used for detection of organic contamination in water by a variety of end users. For example, the SERS substrates may be used by an assortment of industries including but not limited to oil production, mining and/or pharmaceuticals. Such large industrial sectors all have a demonstrated need for water monitoring programs and desire reliable and cost-effective methods to accomplish this. Accordingly, in an embodiment, the sample is wastewater. In another embodiment, the wastewater is from oil production, mining or pharmaceutical industry. In a further embodiment of the present application, the wastewater is produced water. The SERS substrates may, for example also be of interest to quickly diagnose water potability and suitability for consumption. For example, such SERS substrates may, for example be advantageously used in rural areas where regular laboratory facilities are not present to quickly determine whether water was suitable for consumption. This simple method of analysis may allow an untrained person to collect the data and determine rapidly whether organic contamination is present within their source. Accordingly, in another embodiment, the sample is drinking water.

[0065] The following non-limiting examples are illustrative of the present application:

3.4 Examples

3.4.1 Example 1: General preparation of SERS substrates with organosilane capacitated ferrimagnetic iron nanoparticles (FeNPs)

I. Materials

[0066] Substrate preparation: Glass microscope slides, diamond- tipped scribe, nano-pure water, 12 M hydrochloric acid (HCl), 18 M sulfuric acid (H_2SO_4), 95% Ethanol (EtOH), hot plates, PyrexTM containers (for oil baths), Eppendorf pipette (20 μL delivery) and tips, and small neodymium (Nd) magnets (3 p.c., 18 x 3 mm).

[0067] Reactants for iron oxide nanoparticle preparation: Ferric chloride hexahydrate (Sigma Aldrich), Ferrous chloride tetrahydrate (Sigma Aldrich), concentrated ammonium hydroxide (Fisher Scientific), hydrochloric acid (Fisher Scientific), (3-aminopropyl)triethoxysilane (APTES) (Sigma Aldrich), 95% ethanol (Sigma Aldrich) and nano-pure water.

II. Methods

[0068] Washing slides: Separate baths of concentrated H_2SO_4 and HCl were prepared in dishes and each warmed on hot plates in a fume hood to approximately 50 degrees Celsius. Glass microscope slides were cut into thirds using a diamond scribe. In a single layer, the cut slides were placed in the warm HCl bath for about 5-10 minutes. The slides were then individually removed and dipped in a beaker of nano-pure water. The slides were then placed in the warm H_2SO_4 bath in a single layer for another 5-10 minutes before being individually removed and dipped in a beaker of nano-pure water.

The cleaned slides were stored in the EtOH prior to being used in the gold coating step.

[0069] Gold coating slides: A slide was removed from the EtOH and dried with a Kimwipe™. The slide was then rinsed well with EtOH and then dried under a flow of clean, dry air. The dried slide was placed on a stage inside a metal sputterer (Quorum Technologies K550X Sputter Coater), numbered side down. The sputterer was turned on and the argon tank valve opened. The sputterer current was set to 20 mA for 1 minute. This corresponds to a gold deposition thickness of 5 nm. The vacuum chamber was then closed and the procedure started. Once the gold coating was complete, the gold-coated slide was carefully removed, touching the surface at little as possible and was stored in slide box or flat Pyrex dish with Parafilm™ prior to being used in the annealing step.

[0070] Annealing gold-coated slides: A tube furnace was set to 300 °C and the gold-coated slides arranged in a single file in the glass tube, gold side up. The gold-coated slides were left in the oven to anneal for 2 hrs. The oven was then turned off to let the glass cool. The annealed slides were stored in a slide box, or a Pyrex dish with Parafilm prior to being used in further steps.

[0071] Iron oxide nanoparticle (NP) preparation: The NP reactions were carried out under N₂ or another inert gas atmosphere; both the synthesis reaction and coating reaction. The molar ratio of Fe³⁺ Fe²⁺ used was 3:2, with 50 mmol iron total. Nanoparticle formation can, for example, be affected by reaction vessel size, which could, for example, be a factor in scaling the reaction up or down. See, for example: Milosevic et al., “Magnetic metrology for iron oxide nanoparticle scaled-up synthesis” RSC Adv., 2014, 4, 49086-49089 (doi:10.1039/04RA08944H) and Cui et al., “Structure switch between α -Fe₂O₃, γ -Fe₂O₃ and Fe₃O₄ during the large scale and low temper-

ature sol-gel synthesis of nearly monodispersed iron oxide nanoparticles” Advanced Powder Technology 2013, 24:1, 93-97 (doi:10.1016/j.apt.2012.03.001) for exemplary large scale syntheses of iron oxide nanoparticles.

[0072] Synthesis of iron NPs: In a 150 mL or 250 mL beaker under constant stirring with an about 2 cm long magnetic stir bar under an inert environment, about 8.11 g of $\text{FeCl}_3 \cdot 6 \text{H}_2\text{O}$ and about 3.99 g $\text{FeCl}_2 \cdot 4 \text{H}_2\text{O}$ were added to 50 mL of 2M HCl (made with nano-pure H_2O). The solution was heated gently (i.e. temperature kept under 100 °C) throughout. Once the salts had dissolved while still stirring, concentrated NH_4OH (about 25-50 mL) was added slowly, until the reaction reached a pH of 11. Dark brown/black nanoparticles immediately formed upon reaction. Shiny islands may form on the surface of the solution but this will be removed with washing steps. This mixture was allowed to stir and heat for about 30-60 minutes. When complete, the stir bar was removed so as to avoid losing too much product (which was also magnetic), by using a wash bottle to rinse as the bar was brought out of the mixture. The reaction mixture containing NPs was separated into 20 mL scintillation vials for the washing step. The NPs were washed at least 3x with 95% EtOH, using the small magnets to collect solids at the bottom of vials while decanting the supernatant solution off. To retain as much product as possible, decanting was not carried out until the solution was clear. After each addition of EtOH, the vial was shaken to suspend NPs and then the vials were sonicated for about 10 minutes, then these steps repeated.

After washings were complete, about 10 mL of EtOH was added to each vial, the NPs suspended by shaking, and the contents of all vials recombined into one beaker to ensure the same concentration was in each. The contents were then redistributed back into the individual vials.

[0073] Organosilane coating reaction: In a beaker under inert atmosphere, 1 mL of the iron NP solution prepared in the previous step was added to 50 mL of EtOH, while constantly stirring and heating (at a temperature of about 80 °C). 100 μL of APTES was then rapidly added to the reaction vessel and the reaction allowed to heat and stir for about 2 hours. The washing steps outlined above for the synthesis of the iron NPs were then repeated. After washing, the NPs were stored in about 10 mL of EtOH prior to being used in the deposition step.

[0074] Depositing FeNP layers: The annealed gold-coated substrate was placed face-up on an Nd magnet stack. A vial of APTES-coated iron oxide nanoparticles was shaken well before use to ensure the nanoparticles were well suspended. 20 μL of NPs were then delivered onto the substrate, depositing manually around the entire area of magnet (not only in the middle of the substrate) and this layer allowed to dry completely. The deposition and drying was repeated until about 160 μL of NPs had been added. At this point, the substrate was checked via Raman scans to see if the large glass fluorescence band around about 800 cm^{-1} was still present. The 20 μL additions and drying were continued, checking with Raman throughout, until the fluorescence band disappeared, and instead the iron profile became apparent (three broad peaks at roughly 700 cm^{-1} , 500 cm^{-1} , and 350 cm^{-1}). Typically, between a total of 200- 300 μL of iron oxide NP solution was added. This approximately corresponds to 3-5 mg of iron oxide NP. Figure 3.4 shows exemplary Raman spectra of iron oxide NP. At approximately 180 μL of nanoparticles added, Raman peaks for the iron oxide start to appear at around 500 and 350 cm^{-1} . This provides a spectral cue that the appropriate amount of nanoparticle has been added to the substrate.

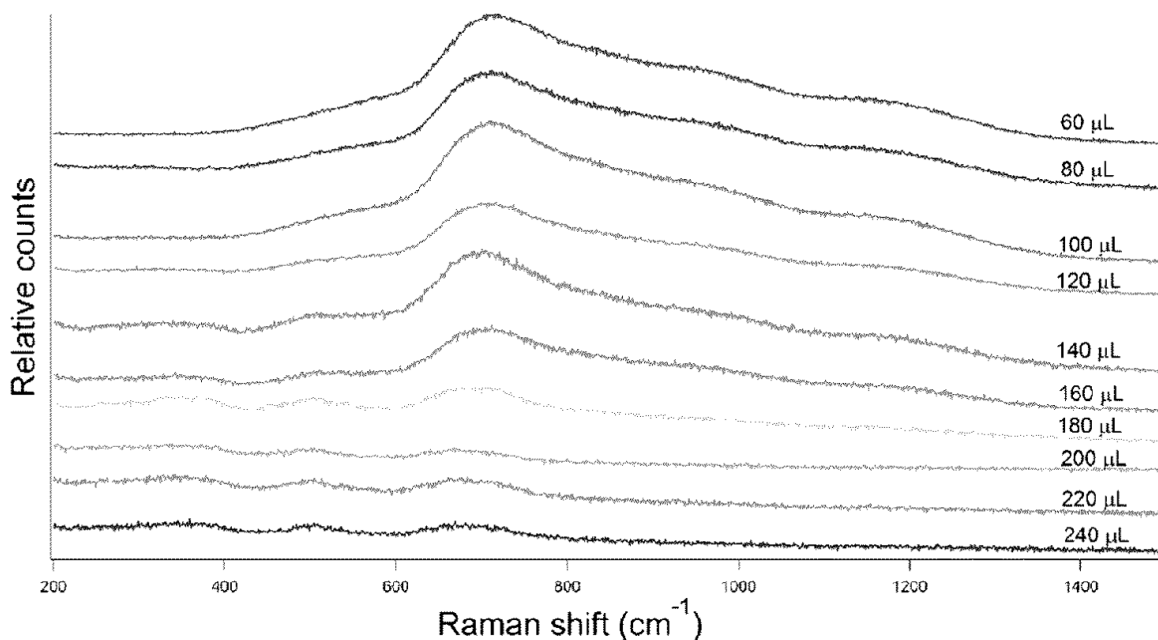


Figure 3.4: Raman spectra of a substrate with increasing layers of iron oxide nanoparticles deposited thereon (from top to bottom: 60, 80, 100, 120, 140, 160, 180, 200, 220 and 240 μL of iron oxide nanoparticle suspension added) according to embodiments of the present application.

3.4.2 Example 2: General preparation of SERS substrates with uncapped ferrimagnetic cobalt iron oxide nanoparticles (CoFeNPs)

I. Materials

[0075] The materials for substrate preparation were in line with those described above in Example 1.

[0076] Reactants for cobalt iron oxide nanoparticle preparation: Ferric chloride hexahydrate (Sigma Aldrich), Cobalt chloride hexahydrate (Sigma Aldrich), concentrated ammonium hydroxide (Fisher Scientific), 95% ethanol (Sigma Aldrich) and nano-pure water.

II. Methods

[0077] The methods for washing slides, gold coating slides and annealing the gold-coated slides were in line with those described above in Example 1.

[0078] Cobalt iron oxide nanoparticle (NP) preparation: The NP reactions were carried out in open air. The molar ratio of Fe^{3+} Co^{2+} used was 2:1.

[0079] Synthesis of cobalt iron oxide NPs: In a 150 mL or 250 mL beaker under constant stirring with an about 5 cm long magnetic stir bar, about 37.8 g of $\text{FeCl}_3 \cdot 6 \text{H}_2\text{O}$ and about 16.6 g $\text{FeCl}_2 \cdot 4 \text{H}_2\text{O}$ were added to 100 mL of nano-pure water. The solution was heated gently (i.e. temperature kept around 80 °C) throughout. Once the salts had dissolved while still stirring, concentrated NH_4OH (about 25-50 mL) was added slowly, until the reaction reached a pH of 11. Dark brown/black solids immediately formed upon reaction. This mixture was allowed to stir and heat for about 90 minutes. When complete, the stir bar was removed by using a wash bottle to rinse as the bar was brought out of the mixture. The reaction mixture containing NPs was separated into 50mL centrifuge tubes for the washing step. The NPs were centrifuged 3x with nano-pure water, decanting the supernatant each time and sonicating in fresh solution to re-suspend the solids. At the end of sufficient washing steps, the supernatant will be a clear colourless solution. The product was collected and dried in an oven overnight to remove the solvent. Once dried, the solid black product was annealed in a tube furnace at 600 °C for 9-10 hours. The final solid after this annealing was ferrimagnetic and responded to external magnetic force. The CoFeNPs were not capped.

[0080] Depositing CoFeNP nanoparticle layers: The annealed gold-coated substrate was placed face-up on an Nd magnet stack. A vial of cobalt iron oxide nanoparticles

(NP) was shaken well before use to ensure the nanoparticles were well suspended. 20 μL of NPs were then delivered onto the substrate, depositing manually around the entire area of magnet (not only in the middle of the substrate) and this layer allowed to dry completely. The deposition and drying was repeated until about 160 μL of NPs had been added. At this point, the substrate was checked via Raman scans to see if the large glass fluorescence band around about 800 cm^{-1} was still present. The 20 μL additions and drying were continued, checking with Raman throughout, until the fluorescence band disappeared, and instead the cobalt iron profile (seven broad peaks at 222 cm^{-1} , 290 cm^{-1} , 409 cm^{-1} , 470 cm^{-1} , 558 cm^{-1} , 612 cm^{-1} , and 676 cm^{-1}) became apparent. Typically, between a total of 400-500 μL of cobalt iron oxide was added. This approximately corresponds to 1-2 mg of cobalt iron oxide NPs. Accordingly, a spectral check with the cobalt iron profile for preparing the SERS substrate with the CoFeNP can be used similar to the spectral check described above in Example 1 using the iron profile for preparing the SERS substrate with the FeNPs.

3.4.3 Example 3: Detection of organic compounds using SERS substrates

I. General Experimental Procedure

[0081] Using a Renishaw in Via confocal Raman system, coupled with an 830 nm diode laser, all Raman scans were performed using a 45 second exposure time at 1% laser power on the 20-times objective lens of the microscope stand. A SERS spectrum of a blank (unexposed) magnetically active SERS substrate prepared as described in Example 1 was taken. A small volume of analyte solution was then dropped onto the substrate and allowed to air dry. Alternatively, the substrate was submerged in the analyte solution for a short period of time and then removed and allowed to dry. Once

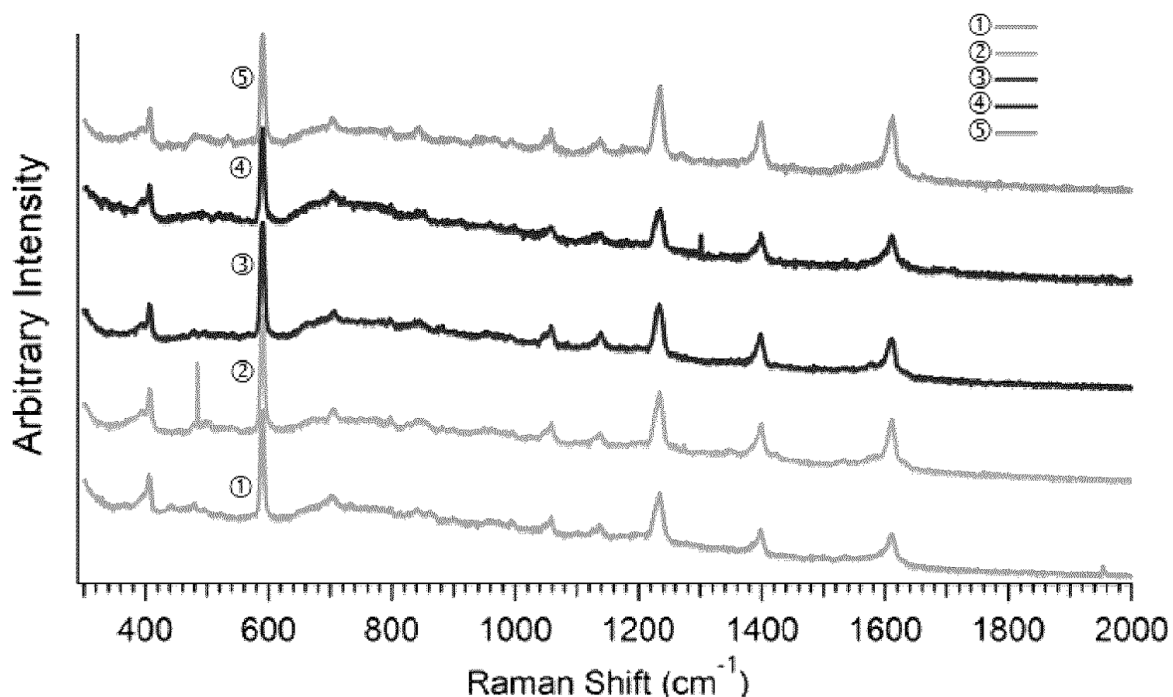


Figure 3.5: SERS spectra obtained of a 1 ppm phenanthrene solution from five different spots of a SERS substrate that it was deposited on according to an embodiment of the present application.

dried, a series of SERS spectra were taken using the same Raman settings as above. The substrate blank spectrum can then be subtracted from the analyte spectra.

II. Results and Discussion

[0082] Once the iron peaks were dominant in the Raman spectra of the SERS substrates prepared as described in Example 1, an analyte solution can be drop cast onto the iron area and allowed to completely dry. Raman analysis can then immediately follow. This method was used to obtain SERS spectra of a 1 ppm phenanthrene solution (Figure 3.5). Spectra were taken across a total of twelve different spots on the substrate, with five spots (1-5) visualized in Figure 5. The results indicated good reproducibility across varying locations on the substrate. The peaks situated at approximately 500 cm^{-1} in spot 2, 1280 cm^{-1} in spot 4, and 1960 cm^{-1} in spot 1 are the

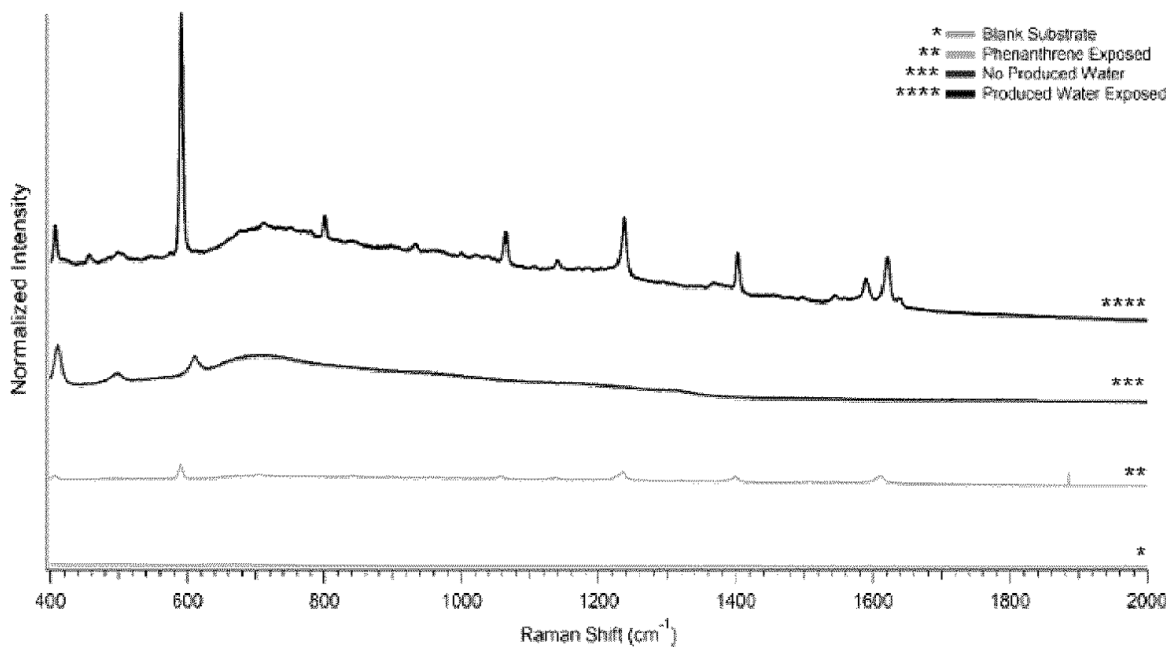


Figure 3.6: SERS spectra obtained using a SERS substrate according to an embodiment of the present application pre-exposure (***) and post-exposure (****) to offshore oil produced water in comparison to a blank (*) and exposure to a 1 ppm phenanthrene solution (**).

result of cosmic radiation interference, and not from the sample or the SERS substrate itself.

[0083] The use of the SERS substrate of Example 1 to detect the components of a produced water sample (from a local oil production platform) was also examined. SERS spectra are shown in Figure 3.6. A substrate blank (spectrum labelled *) was first taken, followed by exposure to a 1 ppm phenanthrene solution (spectrum labelled **). The substrate was then stored for 239 days without washing. Upon receiving a fresh sample of offshore oil produced water, the substrate's ability to detect the components of the water, which are often in the ppb-ppm concentration range was tested by using the same substrate. It was first scanned again (spectrum labelled ***) and was then submerged in the produced water for 10 minutes, removed, and allowed to air dry before re-scanning. Numerous peaks appeared corresponding to various com-

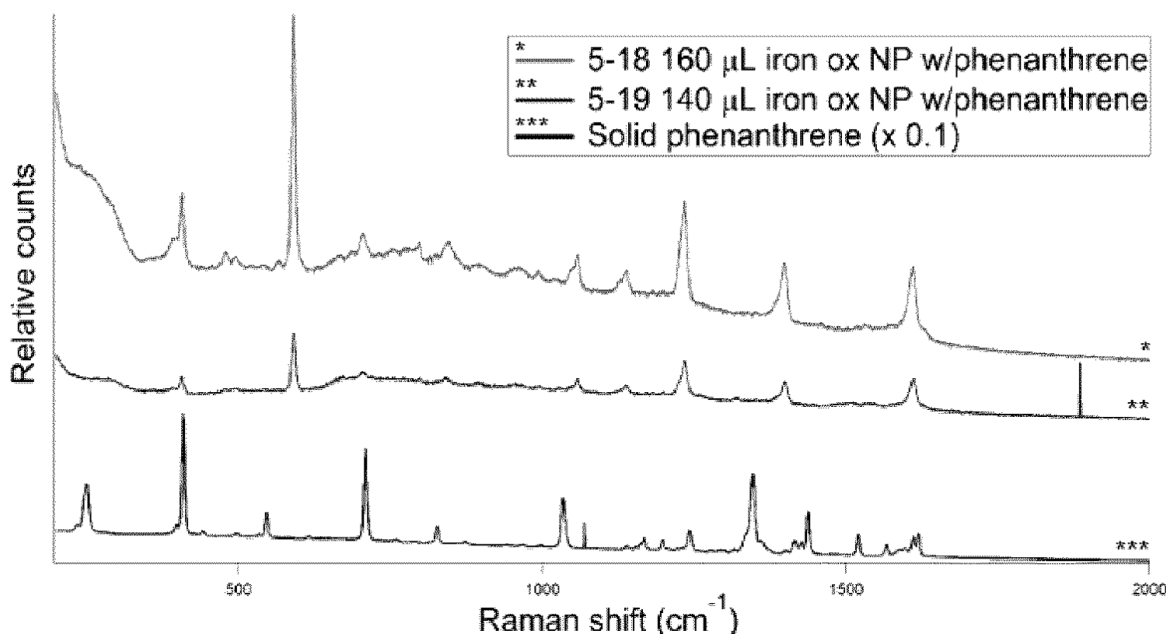


Figure 3.7: SERS spectra of two SERS substrates prepared according to embodiments of the present application using 160 μL (*) and 140 pL iron oxide nanoparticles (***) exposed to 1 ppm phenanthrene, compared to a Raman spectrum of bulk (solid) phenanthrene (***)).

ponents of the produced water sample (spectrum labelled ****). The produced water peaks are easily identified in Figure 3.6 which can facilitate determining individual contaminants. This spectral output can be deconvoluted and individual components are identified to fully characterize and quantify the components present within the produced water using the magnetic SERS substrate and Raman method of detection.

[0084] Validation from other analytical methods may be used, for example, to determine what each Raman peak corresponds to in the spectra obtained using the SERS substrates. For example, the spectra can be compared to a Raman spectrum of known materials. Figure 3.7 shows the SERS spectra of two SERS substrates prepared according to the general procedure described in Example 1 using different amounts of iron oxide NPs (top spectrum: 160 μL , middle spectrum: 140 μL) exposed to 1 ppm phenanthrene, compared to a Raman spectrum (bottom spectrum) of bulk (solid)

phenanthrene.

[0085] For qualitative analysis, the spectra can be analyzed to produce a list of wavenumber shifts that correspond to a SERS peak. The peaks can then be used to determine the analyte of question. If the matrix is more complicated, (i.e., more than one analyte), analysis can be more challenging, especially if it is unknown what the sample is composed of. Accordingly, coupling SERS with a more traditional technique can be beneficial in these instances. For example, initially identifying compounds using either gas or liquid chromatography methods can help make Raman band assignment easier in subsequent analyses.

[0086] For quantitative analysis of analytes using the magnetically active SERS substrates, SERS spectra of analytes of known concentrations can be collected. A diagnostic peak for the analyte can be identified, and Raman peak area calculated using suitable means such as IGOR Pro software. Peak area vs. concentration curves can be produced, giving a calibration curve for that analyte. Concentrations of unknown analytes in a sample with known analytes can then be determined from only the peak area of its diagnostic peak.

[0087] Spectra were also obtained using SERS substrates of Example 2 in which a volume of analyte solution was dropped on the substrate and allowed to air dry using the same general method described above in respect to the spectra obtained using the SERS substrates of Example 1. This method was used obtain SERS spectra of a 1 ppm phenanthrene solution (Figures 8 and 9). Figure 3.8

shows a cobalt iron oxide SERS substrate before and after analyte addition. Spectra were also taken across different spots on the substrate, with four spots (1-4) visualized in Figure 3.9, which shows consistent analyte signal across the substrate.

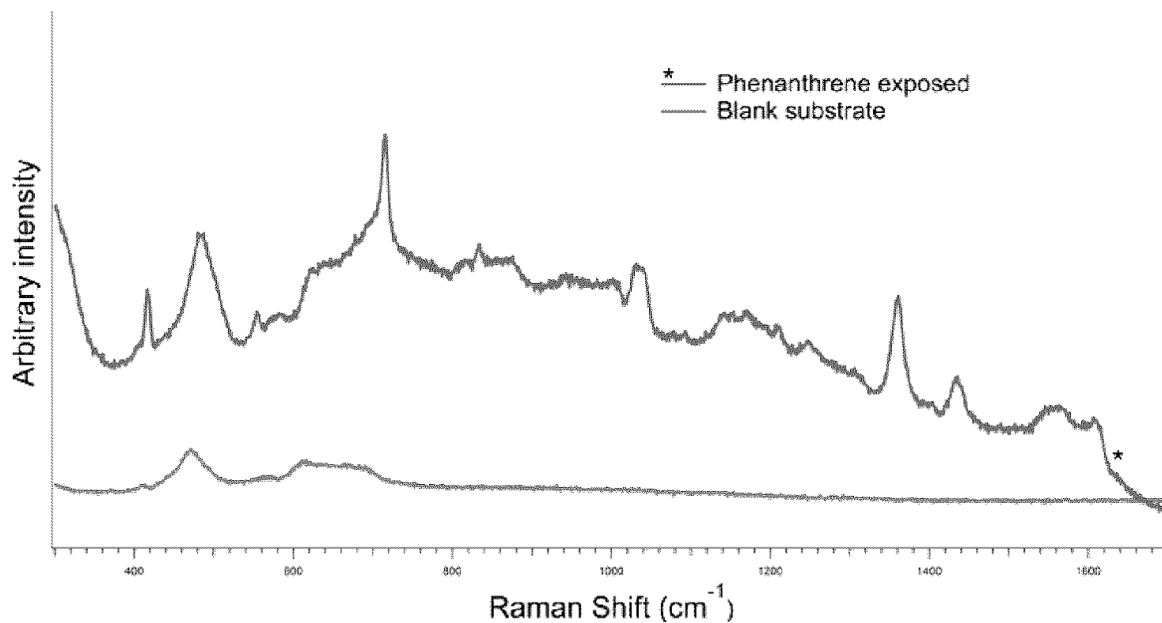


Figure 3.8: SERS spectra obtained using a SERS substrate according to an embodiment of the present application pre-exposure and post- exposure (*) to a 1 ppm phenanthrene solution.

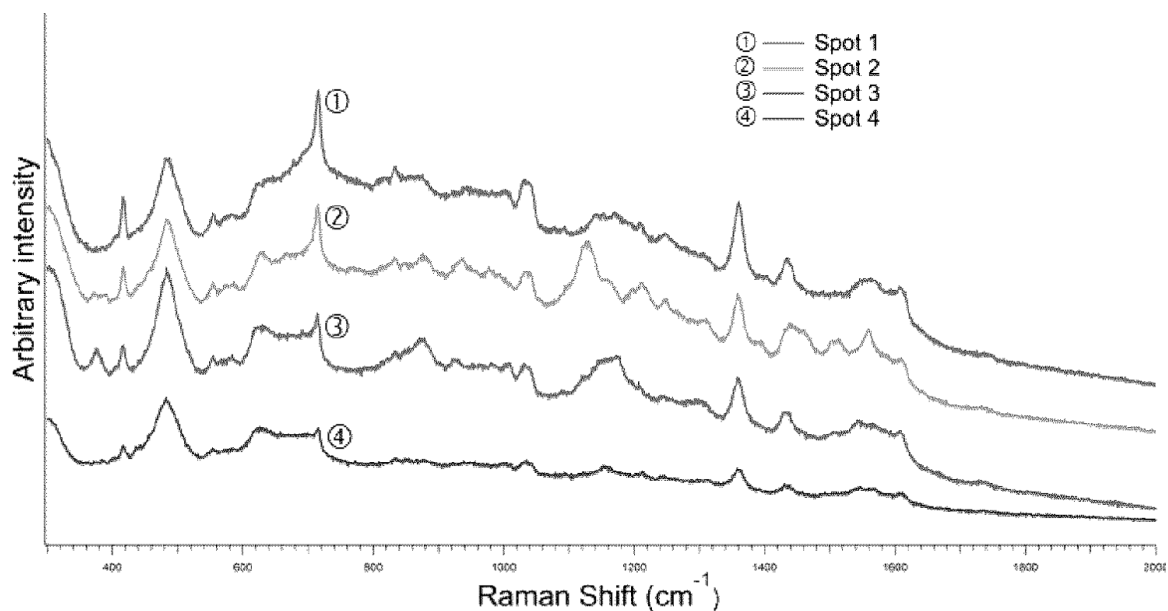


Figure 3.9: SERS spectra obtained of a 1 ppm phenanthrene solution from four different spots of a SERS substrate that it was deposited on according to an embodiment of the present application.

[0088] While the present application has been described with reference to what are presently considered to be the preferred examples, it is to be understood that the application is not limited to the disclosed examples. To the contrary, the present application is intended to cover various modifications and equivalent arrangements included within the spirit and scope of the appended claims.

[0089] All publications, patents and patent applications are herein incorporated by reference in their entirety to the same extent as if each individual publication, patent or patent application was specifically and individually indicated to be incorporated by reference in its entirety. Where a term in the present application is found to be defined differently in a document incorporated herein by reference, the definition provided herein is to serve as the definition for the term.

3.5 Claims

1. A substrate for surface enhanced Raman spectroscopy (SERS), comprising: a support material; a layer of a SERS-active metal on the support material; and a layer of magnetically active nanoparticles on the layer of the SERS-active metal.
2. The SERS substrate of claim 1, wherein the support material comprises glass or plastic.
3. The SERS substrate of claim 2, wherein the support material is glass.
4. The SERS substrate of any one of claims 1 to 3, wherein the support material has a thickness of from about 1.0 mm to about 1.2 mm.
5. The SERS substrate of any one of claims 1 to 4, wherein the SERS- active metal is gold, platinum, silver. or copper.
6. The SERS substrate of claim 5, wherein the SERS-active metal is gold.
7. The SERS substrate of any one of claims 1 to 6, wherein the layer of the SERS-

active metal has a thickness of from about 2.5 nm to about 7.5 nm.

8. The SERS substrate of claim 7, wherein the layer of the SERS-active metal has a thickness of about 5 nm.

9. The SERS substrate of any one of claims 1 to 8, wherein the magnetically active nanoparticles comprise iron oxide.

10. The SERS substrate of any one of claims 1 to 9, wherein the magnetically active nanoparticles are capped.

11. The SERS substrate of claim 10, wherein the magnetically active nanoparticles are capped by (3-aminopropyl)triethoxysilane.

12. The SERS substrate of claim 10 or 11, wherein the magnetically active nanoparticles are ferrimagnetic iron oxide nanoparticles.

13. The SERS substrate of any one of claims 1 to 12, wherein the magnetically active nanoparticles have an average diameter of from about 30 nm to about 60 nm.

14. The SERS substrate of any one of claims 1 to 9, wherein the magnetically active nanoparticles are uncapped.

15. The SERS substrate of claim 14, wherein the magnetically active nanoparticles are ferrimagnetic cobalt iron oxide nanoparticles.

16. The SERS substrate of any one of claims 1 to 15, wherein the layer of the magnetically active nanoparticles has a thickness such that a Raman spectrum of the SERS substrate does not show any detectable bands corresponding to the support material.

17. The SERS substrate of any one of claims 1 to 16, wherein the SERS substrate is configured for use in a handheld Raman spectrometer, a portable Raman spectrometer or a benchtop Raman spectrometer.

18. The SERS substrate of claim 17, wherein the substrate is configured for use in a handheld Raman spectrometer or a portable Raman spectrometer.

19. A method of preparing a substrate for surface enhanced Raman spectroscopy (SERS), the method comprising: depositing a layer of a SERS-active metal on a support material; and depositing a layer of magnetically active nanoparticles on the layer of the SERS-active metal.
20. The method of claim 19, wherein the SERS-active metal is deposited on the support material by a method comprising sputtering.
21. The method of claim 19 or 20, wherein the method further comprises annealing the SERS-active metal prior to depositing the layer of the magnetically active nanoparticles thereon.
22. The method of any one of claims 19 to 21, wherein the layer of magnetically active nanoparticles is deposited on the layer of the SERS-active metal by a method comprising: depositing a portion of a suspension comprising magnetically active nanoparticles and a solvent on the layer of SERS-active metal; evaporating the solvent; and repeating the depositing and evaporating until a layer of magnetically active nanoparticles of a desired thickness has been deposited on the layer of SERS-active metal.
23. The method of claim 22, wherein the desired thickness is such that a Raman spectrum of the SERS substrate does not show any detectable bands corresponding to the support material.
24. The method of any one of claims 19 to 23, wherein the method further comprises capping the magnetically active nanoparticles prior to deposition on the layer of the SERS-active metal.
25. The method of any one of claims 19 to 24, wherein the magnetically active nanoparticles are ferrimagnetic iron oxide nanoparticles having an average diameter of from about 30 nm to about 60 nm.
26. The method of any one of claims 19 to 23, wherein the nanoparticles are uncapped and the method is devoid of a capping step.

27. The method of claim 26, wherein the magnetically active nanoparticles are ferromagnetic cobalt iron oxide nanoparticles, wherein the majority of the magnetically active nanoparticles have a diameter of from about 30 nm to about 60 nm.
28. The method of any one of claims 19 to 27, wherein the SERS active metal is gold.
29. A substrate for surface enhanced Raman spectroscopy (SERS) prepared by a method as defined in any one of claims 19 to 28.
30. A use of a SERS substrate as defined in any one of claims 1 to 18 and 29 for detecting and/or quantifying an analyte.
31. A method for detecting an analyte in a sample, the method comprising: contacting a SERS substrate as defined in any one of claims 1 to 18 and 29 with the sample to adhere the analyte to the SERS substrate; obtaining a SERS spectrum of the analyte adhered to the SERS substrate; and analyzing the spectrum to detect the analyte.
32. The method of claim 31, wherein the contacting comprises submerging at least a portion of the SERS substrate in the sample followed by drying to adhere the analyte to the SERS substrate.
33. The method of claim 31, wherein the contacting comprises depositing the sample on at least a portion of the SERS substrate followed by drying to adhere the analyte to the SERS substrate.
34. The method of any one of claims 31 to 33, wherein the spectrum is obtained by placing the SERS active substrate with the analyte adhered thereto in the path of a Raman laser and acquiring the spectrum in a wavenumber range of from about 200 cm^{-1} to about 2000 cm^{-1} .
35. The method of claim 34, wherein the spectrum is acquired from three locations on the surface of the SERS substrate.
36. The method of any one of claims 31 to 35, wherein the analyzing comprises comparing the Raman shifts of the spectrum to a library of known Raman shifts to

identify the analyte in the sample.

37. The method of any one of claims 31 to 36, further comprising obtaining a SERS spectrum of a SERS substrate without analyte adhered thereto to obtain a blank spectrum then subtracting the blank spectrum from the SERS spectrum obtained of the analyte adhered to the SERS substrate.

38. The method of any one of claims 31 to 37, wherein the analyte is a known analyte or has been identified and the analyzing comprises: calculating the peak area of a diagnostic peak in the spectrum; and comparing the calculated peak area to a calibration curve of peak areas for that diagnostic peak as a function of concentration of analyte to quantify the amount of the analyte in the sample.

39. The method of any one of claims 31 to 38, wherein the sample comprises an unknown analyte and the analyzing comprises: adding a desired amount of a stock solution comprising a known concentration of a known analyte to the sample; calculating the peak area of a diagnostic peak in the spectrum for the known analyte, calculating the peak area of a diagnostic peak for the unknown analyte, and comparing the calculated peak area of the unknown analyte to the peak area of the known analyte to quantify the amount of the unknown analyte in the sample.

40. The method of any one of claims 31 to 39, wherein the sample is wastewater.

41. The method of claim 40, wherein the wastewater is produced water.

42. The method of any one of claims 31 to 39, wherein the sample is drinking water.

Chapter 4

Powerful electromagnetic field enhancement via complex cobalt ferrite surfaces for plasmonic sensing *

4.1 Abstract

Though magnetic nanomaterials have been employed in a number of surface-enhanced Raman spectroscopy (SERS) applications, they often fill a background role in being an anchoring site or vehicle for other materials. Cobalt ferrites are robust analogues to the well-studied ferrimagnetic iron oxides, but despite this link, their implementation into SERS devices have not been well explored. Here we report a powerful, novel plasmonic surface which features hierarchically-patterned magnetic nanoscale

*This chapter has been submitted to *Chemical Communications* as “Powerful electromagnetic field enhancement via complex cobalt ferrite surfaces for plasmonic sensing”, Stephanie M. V. Galant, Erika F. Merschrod S, CC-COM-08-2021-004641 (2021).

cobalt ferrites, with limits of detection below 1 ppb, signal-to-noise ratios upwards of 3 dB, and strong enhancement across the substrate. Beyond its outstanding performance, our surface opens a new direction in SERS sensing, using magnetic materials to enhance signal.

4.2 Communication

Traditional coinage metals used in surface-enhanced Raman spectroscopy (SERS), like silver and gold, have been well-studied in their roles as plasmonic surfaces. On the Raman platforms where sensing occurs, the free surface electrons of a plasmonic material allows for enhancement of the overall electromagnetic field, increasing the resultant Raman signal. This is particularly advantageous for the sensing of dilute analytes, or molecules without particularly strong Raman modes. Though substrates made of these aforementioned coinage metals have been heavily relied on, researchers are looking towards more novel surface designs and materials, which allow for better performance and stability as optical sensors.

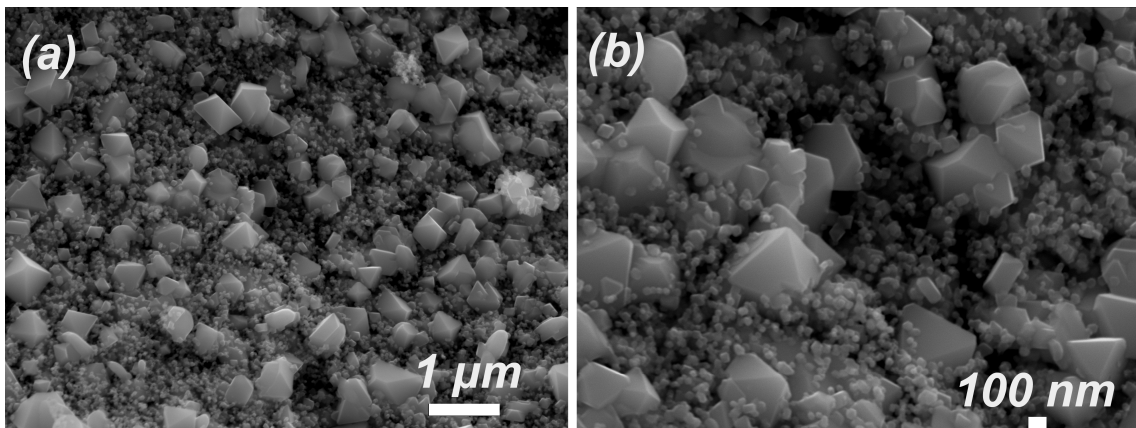


Figure 4.1: Nanoscale cobalt ferrite crystals, as synthesized via coprecipitation. The one-pot method at this reaction scale results in a mixture of particle shapes: nanospheres with a diameter around 45 nm, octahedra ranging from 100-500 nm, and a small number of disks around 100-300 nm.

We report a new sensing platform which incorporates nanoscale magnetic cobalt ferrites of mixed geometry in a hierarchical arrangement on our surface. The nanoparticle (NP) layers are directed via a magnetic field, creating a radial pattern like spokes of a wheel, where the gaps between the spokes allow the base layer of a gold thin-film to show through. This combination of materials, along with surface topography, provides both facile adhesion sites and a strongly-enhancing environment for highly sensitive Raman analysis.

In the fields of nanomaterials and inorganic chemistry, iron oxides have been well-studied, allowing for implementation into sensing devices.^{1,2} Ferrimagnetic forms like magnetite (Fe_3O_4) and maghemite (Fe_2O_3) have been utilised, often acting as core-shell attachment sites and/or vehicles for other molecules, particularly for biological sensing.^{3,4} Given these common uses, very few studies even consider the role which magnetic nanoparticles may play in the sensing itself, particularly in SERS.⁵

Iron oxide analogues, such as cobalt or nickel iron oxides, are of more recent interest, where these crystal types of these new ferrites are the same as traditional magnetite.^{6,7} Co^{2+} or Ni^{2+} fill the sites which would typically be occupied by Fe^{2+} in the inverse spinel structure, constituting a portion of the octahedral sites in the crystal.⁸ By changing the metal at this site, the resultant material has notably increased stability, magnetic remanence, and magnetic hardness when compared to iron oxides, along with a comparable saturation magnetization.^{7,9}

We report an extremely sensitive, reliable, and strongly enhancing optoelectronic sensor designed using magnetic cobalt ferrite nanoparticles (NPs), synthesized via coprecipitation.^{6,10} The cobalt ferrite NPs have two major sizes and shapes, which can be seen in (a) and (b) of Figure 4.1: spheres around 45 nm in diameter, and octahedra ranging from 100-500 nm in size. Each shape has the same composition, as confirmed by energy-dispersive X-ray spectroscopy (EDS), where the ratio of cobalt,

iron, and oxygen remain effectively the same between the spheres and octahedra.

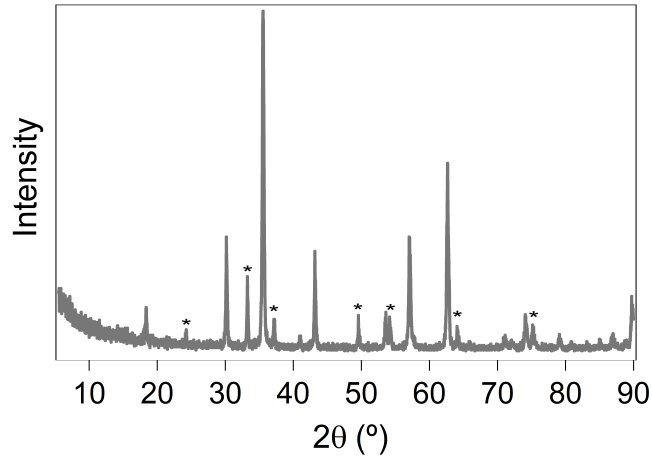


Figure 4.2: Diffraction patterns of cobalt ferrite nanoparticles synthesised by coprecipitation, showing the expected inverse spinel profile. Asterisks denote minor hematite ($\alpha\text{-Fe}_2\text{O}_3$) impurity.

As seen in Figure 4.2, the major X-ray diffraction (XRD) peaks of the cobalt ferrite NPs show the diffraction pattern for an inverse spinel structure.¹¹ The cobalt ferrite NPs contain a small portion of hematite impurity¹² (marked with asterisks) due to the oxygenic environment of the synthesis, making up a minority of the solid. Numerous attempts to separate this hematite from the magnetic ferrite proved unsuccessful, both via centrifuging and magnetic separation, which implies the hematite is within the magnetic particles themselves. Along with Raman spectroscopy confirming the presence of cobalt ferrite¹³ in Figure 4.5 (b), the lack of hematite¹² present in the Raman spectra of the NPs implies it is highly crystalline, but a minority product.

Figure 4.3 shows a Vibrating Sample Magnetometry (VSM) curve for the cobalt ferrite NPs. The magnetic saturation value (plateaus ± 8 kOe) is 58 emu/g for these mixed cobalt ferrites, comparable to values for equivalent iron oxides,¹ while the magnetic coercivities (H_C) are large at around 1.2 kOe. The magnetic remanence is also large at 25 emu/g, meaning these NPs behave as permanent magnets, as they retain a field without being under the influence of an external field.

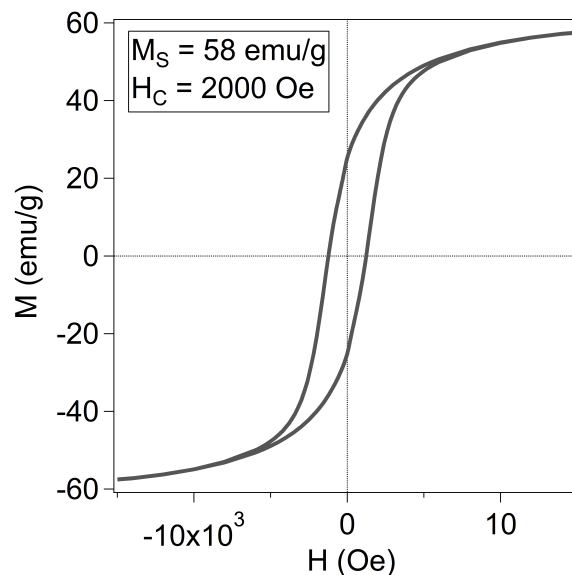


Figure 4.3: VSM curve for cobalt ferrite nanoparticles. The cobalt ferrites have a H_C value of 2 kOe, meaning the NPs behave as permanent magnets.

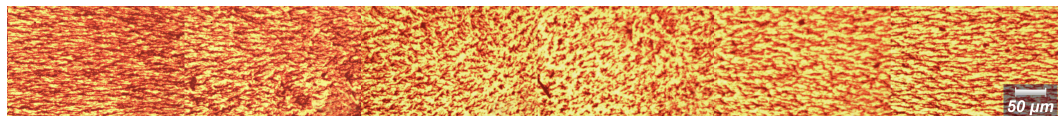


Figure 4.4: Stitched optical images at x5 of the fabricated substrate surface, showing the magnetic patterning of the cobalt ferrite layers.

When added to the substrate as this top surface component, the cobalt ferrite NPs pattern following the magnetic field lines of the applied magnet, seen in Figure 4.4. Spectral collection is easy, with no difficulties locating hot-spots, giving consistent spectra across the 2 cm^2 surface. The spot size of the laser is around $50 \mu\text{m}$ in diameter. (The spot is not a perfect circle; see Figure C.2 in SI.)

Figure 4.5 displays an enhancement spectrum for 1 ppm phenanthrene (a highly-stable poly-aromatic hydrocarbon (PAH) of environmental concern^{15,16}) on the patterned cobalt ferrite surface, after loading via substrate submersion in solution. The blank substrate signal in (b) only displays characteristic NP peaks, while (c) shows a significant signal in the exposed spectrum with phenanthrene present. The spectrum

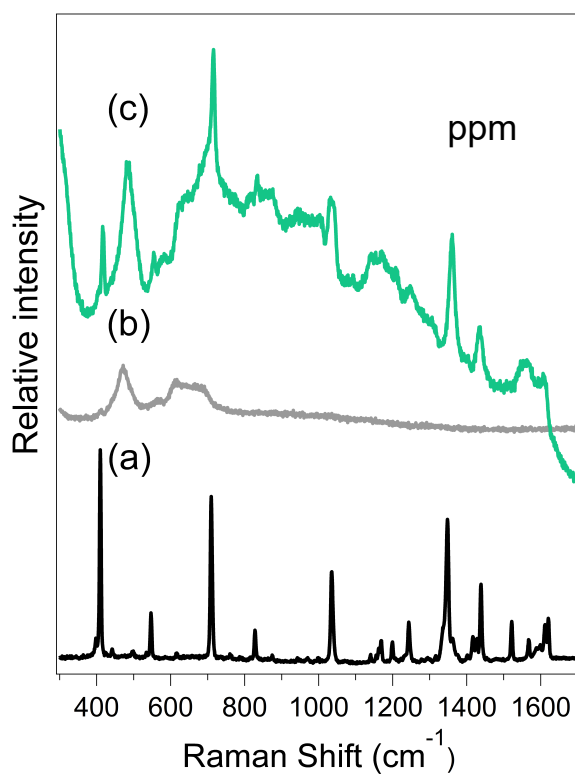


Figure 4.5: Raman enhancement of 1 ppm phenanthrene on substrate surface with patterned NP layers. Spectrum (a) shows the modes of solid phenanthrene crystals. In the exposed spectrum (c), the broad peak at 460 cm^{-1} can be attributed to the strong T_{1g} mode of cobalt ferrite also present in (b), showing Raman modes of the substrate itself before exposure to analyte, while the remainder of peaks in (c) are the result of analyte enhancement on the surface.¹⁴ The spectra are offset for clarity but are all on the same scale.

of the PAH itself is displayed in Figure 4.5 (a), showing peaks which are correspondingly enhanced in the SERS spectrum. The Raman modes are from various C-C bends and stretches of the analyte in proximity to the surface.¹⁷ Due to the surface, the spectrum changes from the bulk analyte spectrum. The signal-to-noise ratios (SNRs) for these spectra are upwards of 3 dB for major peaks, with the smaller enhancement peaks having SNRs of 2 dB.

The greatly enhanced performance of the cobalt ferrite surface can likely be attributed to a combination of geometry and magnetic properties of the solids. For the geometry, octahedral particles as pictured in Figure 4.1 provide hot spots through their sharp edges and points, allowing for surface electron localization.^{18,19} Spherical NPs fill in the gaps between the much larger octahedra, which are 2-10 times larger than the nanospheres; this filling between large particles allows for greater hot spot location probability across the entire surface.¹⁹

When signal strength is weak due to extremely low analyte concentrations, the addition of an external magnet during collection boosts the electromagnetic field across the entirety of the surface. Figure 4.6 shows Raman spectra for the same surface exposed to 1 ppb of phenanthrene, with and without an applied external magnetic field during acquisition. Applying this field greatly increases the intensity of the Raman signal.

Exposed substrates were allowed to sit in ambient conditions for one year, and Raman spectra were collected from the surface after this time period. The substrate showed enhancement of the original analyte comparable to the freshly exposed data, indicating the surface can be used in an archival nature. Additionally, the substrates are reusable with simple rinsing. With a small volume of toluene (around 150 mL total) the exposed substrate surface was sprayed with solvent while held vertically with tweezers. This rinse was repeated three times, and the substrate was allowed

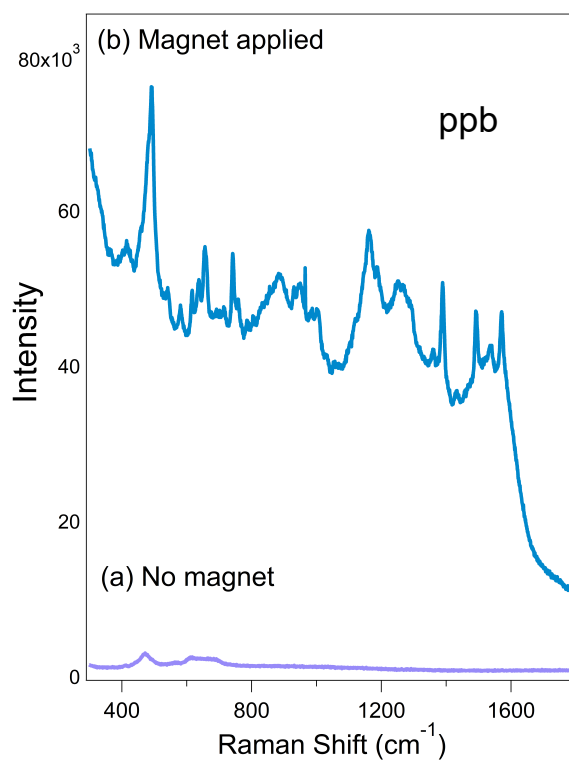


Figure 4.6: Raman enhancement of 1 ppb of phenanthrene on patterned CF surface. For areas of surface where sensing is a challenge (a), an external magnetic field applied during acquisition greatly boosts the signal of the analyte (b).

to dry before a Raman spectrum was collected. The Raman spectra before and after rinsing can be seen in Figure C.1.

The geometry and magnetic remanence of the NPs on this surface are important factors that influence how our sensors are able to enhance signal. In this work, we have shown that cobalt ferrite nanoparticles can be patterned in multi-layers using a magnetic field, with this novel surface acting as an extremely sensitive SERS platform. Boasting limits of detection below 1 ppb for polyaromatic hydrocarbons and SNRs of 3 dB, our surface has strong potential to be integrated into sensing devices for complex matrices with dilute analytes of interest.

4.3 Acknowledgement

This research was conducted on the island of Newfoundland, the ancestral homeland of the Beothuk and the unceded ancestral and current land of the Mi'kmaq. The authors thank the Natural Science and Engineering Council of Canada (NSERC, DG program) and the Dean of Science office at Memorial University for operating funds, The Canada Foundation for Innovation (CFI) for instrumentation funding, and the School of Graduate Studies of Memorial University of Newfoundland for a stipend for SMVG. We also thank Prof. K. Poduska (Physics) for access to the VSM, and Dr. W. Aylward (CREAIT) for access to the SEM and EDX, sample preparation for SEM, EDX and pXRD, and for operation of the XRD facility.

4.4 Conflicts of interest

There are no conflicts to declare.

Bibliography

- [1] Wu, W.; Wu, Z.; Yu, T.; Jiang, C.; Kim, W.-S. Recent progress on magnetic iron oxide nanoparticles: synthesis, surface functional strategies and biomedical applications. *Sci. Technol. Adv. Mater.* **2015**, *16*, 023501.
- [2] Tümay, S. O.; Şanko, V.; Şenocak, A.; Demirbas, E. A hybrid nanosensor based on novel fluorescent iron oxide nanoparticles for highly selective determination of Hg²⁺ ion in environmental samples. *New J. Chem.* **2021**, *45*, 14495–14507.
- [3] Lim, J.; Majetich, S. A. Composite magnetic-plasmonic nanoparticles for biomedicine: Manipulation and imaging. *Nano Today* **2013**, *8*, 98–113.
- [4] Kang, H. J.; Ali, R. F.; Paul, M. T.; Radford, M. J.; Andreu, I.; Lee, A. W.; Gates, B. D. Tunable functionalization of silica coated iron oxide nanoparticles achieved through a silanol-alcohol condensation reaction. *Chem. Commun.* **2019**, *55*, 10452–10455.
- [5] Wang, Y.; Liu, Q.; Sun, Y.; Wang, R. Magnetic field modulated SERS enhancement of CoPt hollow nanoparticles with sizes below 10 nm. *Nanoscale* **2018**, *10*, 12650–12656.
- [6] Karaagac, O.; Bilir, B.; Köçkar, H. The influence of synthesis parameters on one-step synthesized superparamagnetic cobalt ferrite nanoparticles with high saturation magnetization. *J. Magn. Magn. Mater.* **2019**, *473*, 262–267.
- [7] Saeid, M.; Shokrollahi, H.; Zamanian, A. The magnetic-field-assisted synthesis of the Co-ferrite nanoparticles via reverse co-precipitation and their magnetic and structural properties. *Mater. Chem. Phys.* **2018**, *215*, 355–359.

- [8] Houshiar, M.; Zebhi, F.; Razi, Z. J.; Alidoust, A.; Askari, Z. Synthesis of cobalt ferrite (CoFe_2O_4) nanoparticles using combustion, coprecipitation, and precipitation methods: A comparison study of size, structural, and magnetic properties. *J. Magn. Magn. Mater.* **2014**, *371*, 43–48.
- [9] Senthil, V. P.; Gajendiran, J.; Raj, S. G.; Shanmugavel, T.; Ramesh Kumar, G.; Parthasaradhi Reddy, C. Study of structural and magnetic properties of cobalt ferrite (CoFe_2O_4) nanostructures. *Chem. Phys. Lett.* **2018**, *695*, 19–23.
- [10] Naik, S. R.; Salker, A. V. Change in the magnetostructural properties of rare earth doped cobalt ferrites relative to the magnetic anisotropy. *J. Mater. Chem.* **2012**, *22*, 2740–2750.
- [11] Estrada, S. O.; Huerta-Aguilar, C. A.; Pandiyan, T.; Corea, M.; Reyes-Domínguez, I. A.; Tavizon, G. Tuning of the magnetic response in cobalt ferrite $\text{Co}_x\text{Fe}_{3-x}\text{O}_4$ by varying the Fe_2^+ to Co_2^+ molar ratios: Rietveld refinement and DFT structural analysis. *J. Alloys Compd.* **2017**, *695*, 2706–2716.
- [12] Feng Lu, J.; Tsai, C. J. Hydrothermal phase transformation of hematite to magnetite. *Nanoscale Res. Lett.* **2014**, *9*, 1–8.
- [13] Puli, V. S.; Adireddy, S.; Ramana, C. V. Chemical bonding and magnetic properties of gadolinium (Gd) substituted cobalt ferrite. *J. Alloys Compd.* **2015**, *644*, 470–475.
- [14] Rani, B. J.; Ravina, M.; Saravanakumar, B.; Ravi, G.; Ganesh, V.; Ravichandran, S.; Yuvakkumar, R. Ferrimagnetism in cobalt ferrite (CoFe_2O_4) nanoparticles. *Nano-Structures and Nano-Objects* **2018**, *14*, 84–91.
- [15] Bartonitz, A.; Anyanwu, I. N.; Geist, J.; Imhof, H. K.; Reichel, J.; Graßmann, J.;

- Drewes, J. E.; Beggel, S. Modulation of PAH toxicity on the freshwater organism *G. roeseli* by microparticles. *Environ. Pollut.* **2020**, *260*, 113999.
- [16] Murawski, A.; Roth, A.; Schwedler, G.; Schmied-Tobies, M. I.; Rucic, E.; Pluym, N.; Scherer, M.; Scherer, G.; Conrad, A.; Kolossa-Gehring, M. Polycyclic aromatic hydrocarbons (PAH) in urine of children and adolescents in Germany – human biomonitoring results of the German Environmental Survey 2014–2017 (GerES V). *Int. J. Hyg. Environ. Health* **2020**, *226*, 113491.
- [17] Alajtal, A. I.; Edwards, H. G. M.; Elbagerma, M. A.; Scowen, I. J. The effect of laser wavelength on the Raman Spectra of phenanthrene, chrysene, and tetracene: Implications for extra-terrestrial detection of polyaromatic hydrocarbons. *Spectrochim. Acta - Part A Mol. Biomol. Spectrosc.* **2010**, *76*, 1–5.
- [18] Heo, J.; Kim, D. S.; Kim, Z. H.; Lee, Y. W.; Kim, D.; Kim, M.; Kwon, K.; Park, H. J.; Yun, W. S.; Han, S. W. Controlled synthesis and characterization of the enhanced local field of octahedral Au nanocrystals. *Chem. Commun.* **2008**, 6120–6122.
- [19] Gong, T.; Luo, Y.; Zhang, H.; Zhao, C.; Yue, W.; Pu, M.; Kong, W.; Wang, C.; Luo, X. Hybrid octahedral Au nanocrystals and Ag nanohole arrays as substrates for highly sensitive and reproducible surface-enhanced Raman scattering. *J. Mater. Chem. C* **2020**, *8*, 1135–1142.

Chapter 5

Scaling the synthesis of cobalt ferrite nanoparticles resulting in differing properties: a SERS study

Magnetic nanoparticles (NPs) are a powerful and versatile class of materials, boasting both the properties found only at the nanoscale, along with magnetic behaviour. Cobalt ferrite nanoparticles (CFNPs) are a newer class of magnetic nanomaterial, some of which act as individual nanomagnets with various geometries. Here we report the tuning of CFNPs in a surface-enhanced Raman spectroscopy (SERS) platform, where these materials are arranged in a complex multi-layer mediated by magnetic fields. Mixtures of CFNP crystals with different geometries are created by varying the synthesis scale, and these products are each tested in their abilities as SERS components for enhancement of dilute environmental hydrocarbons. All sensors made with CFNPs resulted in significant and reliable detection beyond 1 ppb. Sensors made using CFNP crystals with large octahedra & disks among a majority of nanospheres, with magnetic remanence of 25 emu/g and a magnetic coercivity of 1200 Oe, resulted

in the best performance with signal-to-noise ratios (SNRs) of over 4 dB. Additionally, an applied magnetic field on the sensing surface during spectral acquisition resulted in a three-fold increase in signal intensity, providing evidence that the magnetic influence of the surface materials are integral to the enhancement mechanism.

5.1 Introduction

Magnetic nanoparticles (NPs) are of great interest to many fields of applied materials research, finding use in applications such as drug delivery,¹ biological sensing,² magnetic separation,³ magnetic resonance imaging,⁴ among others. Iron oxides nanoparticles (IONPs) are the most well-studied and utilized type magnetic NPs,^{5,6} as they are highly accessible materials which are bio-compatible⁷ and easily surface-functionalized.⁸

Cobalt ferrite nanoparticles (CFNPs) are an analogue of traditional IONPs, where Co^{2+} replaces Fe^{2+} in the inverse spinel crystal structure.⁹ These CFNPs are finding new applications beyond that of IONPs, particularly for use in electronics,¹⁰ batteries,¹¹ and sensors.^{12,13} While replacing the Fe^{2+} with Co^{2+} in CFNPs aids in preventing their prevalent oxidation issues, swapping the metal ions also results in changes in material properties. CFNPs have significantly higher magnetic coercivities compared to IONPs, meaning they behave as permanent magnets, though at critical sizes they can also have paramagnetic behaviour.⁹

While magnetic NPs have been used in optoelectronic/plasmonic sensing applications like surface-enhanced Raman spectroscopy (SERS), they have been limited to use as "handles" for moving (via magnetic fields) other materials, often plasmonic components like gold or silver.¹⁴ The contribution of the IONPs (or other magnetic metal oxides) have been negated and not studied or quantified in their plasmonic

contributions thus far.

There have been some studies in recent years looking into effects of magnetic fields on electric fields (and vice versa) in plasmonic systems,^{15, 16} where presence of one field will influence the other when occupying the same space.^{15, 16} However, most of these studies utilize fibre-optics and magnetic fluids, and they don't include the impact of magnetic fields on potential SERS activity of these plasmonic materials. With this in mind, along with the awareness that SERS aims to similarly enhance local fields through electron-light interactions, it follows that the addition of a magnetic field on a solid sensing surface could lead to enhancement of the overall electromagnetic field.

In this report, we present a continuation of the work in 2 using a new magnetic material (CFNPs), studying changes in the crystal properties as we scale the reaction mechanism. We then integrate these products into a sensing surface, and test the SERS performances of the different crystals, in efforts to quantify the sensing parameters required for enhancement. As magnetism plays such a significant role in the materials and design, we additionally aim to explore the question: does magnetism on the sensing surface boost plasmonic enhancement?

5.2 Experimental

5.2.1 Materials

Cobalt(II) chloride hexahydrate ($\geq 99\%$) and iron(III) chloride hexahydrate ($\geq 99\%$) were purchased from Sigma Aldrich (Oakville, Ontario, Canada). Concentrated acids (sulfuric and hydrochloric) were obtained from Fisher Scientific (Ottawa, Ontario, Canada). Concentrated ammonium hydroxide was purchased from ACP Chemicals (Montreal, Quebec, Canada). Nanopure water (distilled and filtered) was obtained from a Barnstead 18.2 M Ω ·cm system. All chemicals were used without further

purification.

5.2.2 Nanoparticle Synthesis

A method of pH-mediated coprecipitation was performed as per the well-reported Masart¹⁷ method.

Nanoparticles were initially synthesized based on the masses of reagents reported by Karaagac (2019).⁹ Into 100 mL of nanopure water, 37.8 g of $\text{FeCl}_3 \cdot 6 \text{H}_2\text{O}$ and 16.6 g of $\text{CoCl}_2 \cdot 6 \text{H}_2\text{O}$ were added under constant stirring at 90 °C. After dissolution of the salts, yielding a brown solution, concentrated NH_4OH was gently added, around 0.5 mL/sec. A total volume of around 50 mL was added, approaching the target pH of 11 for the reaction mixture. When base was added, a light brown solid formed, creating an overall thick mixture. The products continued to stir under heat for 90 minutes, after which they were allowed to cool and were then neutralized using dilute HCl.

To wash the solids and remove all counter-ions, the products were put into 50 mL centrifuge tubes and then washed in triplicate with nanopure water, with centrifuging down solids between each wash. Once washing was complete, the products were dried at 80 °C overnight.

Once dried, the solids were finely ground using a mortar and pestle, and annealed in a tube furnace at 600 °C for 9 hours. Post-annealing, the solid is magnetic, which can be quickly checked by applying an external magnet to a vessel containing the particles. The solids were then stored under ambient conditions in closed containers, and were then used as-is.

For the scaled-down syntheses (25%, 12%), the above synthesis procedure was repeated with reactant masses scaled down equivalently. Size of the reaction beaker was also scaled down appropriately, while all other variables and parameters remained

unchanged.

5.2.3 Characterization

Scanning electron microscopy (SEM) analysis was completed with a JEOL JSM-7100F Scanning Electron Microscope, with a working probe of 10-15 kV and a working distance of 12 mm. All samples were lightly carbon coated to prepare solids for the beam. Additionally, elemental analysis was completed at the same time as SEM analysis, via **energy-dispersive X-ray spectroscopy (EDX)**. Magnetic **Vibrating sample magnetometry (VSM)** measurements were completed with a MicroSense EZ vibrating sample magnetometer, where data was collected between ± 20 kOe at (25 \circ).

Raman spectroscopy of all solids and substrates was performed with a Renishaw InVia confocal Raman system, fit with an 830 nm diode laser source, along with a Leica DM2700 microscope. Optical micrographs were obtained with the camera on this microscope. All Raman spectra were collected at reduced power, 3.0 ± 0.3 mW (1% power). Raman shift values were determined via maximum intensities of each peak, while peak areas were calculated using Gaussian fits centred on these maximum intensities. **Powder X-ray diffraction (pXRD)** data were collected from 20° to 80° 2θ using a Rigaku Ultima IV X-Ray diffractometer (Cu-K α source).

5.2.4 Substrate Fabrication Method

Microscope slides (Technologist ChoiceTM, 75 mm x 26 mm x 1 mm in size) were used as the base of substrates, each one being cut into three pieces with a diamond scribe (SPI Supplies). Slides were washed in warmed acid baths (HCl, followed by H₂SO₄), using nanopure water to rinse between each stage. Washed slides were rinsed with nanopure water, followed by ethanol, and then stored in ethanol until ready for use.

The clean slides were then rinsed and dried using compressed air, after having been etched with sample codes on the back side. Then the slides were layed out on the stage of a Quorum Technologies K550X Sputter Coater, fit with a gold target (Soquelec model number K550X Au target: 60 mm diameter Au disk, 0.1 mm thickness). Argon gas (Praxair Canada Inc., ultra-high purity) was then pumped into the chamber, and the slides immediately coated via sputtering of gold. A time of 60 seconds in the chamber, with a working current of 20 mA, led to a deposited thickness of gold around 5 nm. The coated slides were then annealed for 2 hours at 300 °C in a tube furnace (Thermo Scientific Lindberg Blue M).

After the tube furnace annealing, the slides were layed on a stack of neodymium alloy magnets (stack of three disks, with sizes of 18 mm × 3 mm). Layers of the CFNP solution were then successively added in layers on the surface. These NPs were suspended in solution via sonication (Fisher Scientific FS20) beforehand, to ensure they were adequately dispersed. The layers were added in 2 μ L volume intervals, until any fluorescence peaks in the Raman spectrum were adequately quenched.

5.2.5 Substrate Testing Method

The completed substrates were individually exposed to an analyte solution, through a simple beaker loading. The substrate was placed in a beaker containing 50 mL of analyte solution at a given concentration, and then allowed to sit for half an hour. After this time, the substrate was removed and the solvent allowed to evaporate. Once dry, the substrate could be analyzed immediately via Raman spectroscopy.

5.2.6 Substrate Washing Method

Washing procedures were implemented on the substrate surface to test potential reusability of the substrates. Previously exposed samples were checked for enhance-

ment after sitting in storage for 6 months (under ambient conditions), where analyte peaks were still present.

Exposed substrates were held perpendicular to the bench-top above a beaker, and toluene was sprayed onto the substrate surface in quick, ~ 0.5 mL intervals. Raman data collected after this rinse showed removal of all analyte peaks.

5.3 Results

5.3.1 Characterization of Particles

While many aspects of the products synthesized are similar, many crucial properties differ in ways which provide insight to their potential use in optoelectronics.

| Scale | Geometries | % distribution | Smaller particle (<100nm) details | Larger particle details | min & max (nm) |
|---------------|------------|----------------------------------|---|--|----------------|
| 100% (90 °C) | S, D, O | 60% small, 40% large | Many NS, avg size 60 nm, majority of sample | Equal amounts D & O. Avg sizes around 400 nm. | 40 1000 |
| 100% (45 °C) | S, D, O | 10% small, 75% medium, 15% large | NS avg size 60nm, very small amount of the sample | Majority "medium" S ~ 150 nm. Some O and D with size 200-300 nm. | 45 500 |
| 25% | S, D, O | 50% small, 50% large | Many NS, avg size 60 nm | 3:2 ratio D:O. Avg O size ~400 nm; avg disk size ~700 nm | 45 850 |
| 12% | S, D | 50% small, 50% large | Many NS, avg size 60 nm | Large D make up remainder of sample. Avg size ~500 nm | 45 600 |

Table 5.1: Comparison of CFNP products produced in different reaction scales, as studied via SEM. Shapes include spheres (S), octahedra (O), and disks (D). The smallest particles are nanospheres (NS), which are present in all samples.

| Scale | E_g (cm^{-1}) | T_{2g} (2) (cm^{-1}) | A_{1g} (2) (cm^{-1}) | A_{1g} (1) (cm^{-1}) |
|---------------|----------------------------|-----------------------------------|-----------------------------------|-----------------------------------|
| 100% (90 °C) | 292.0 | 470.4 | 630.9 | 678.9 |
| 100% (45 °C) | 290.81 | 471.8 | 617.6 | 672.4 |
| 25% | 292.2 | 473.3 | 595.4 | 657.9 |
| 12% | 294.2 | 475.5 | 612.1 | 660.2 |

Table 5.2: Raman modes of CFNPs synthesized at different reaction scales, showing shifting of peak position which trend with scale.

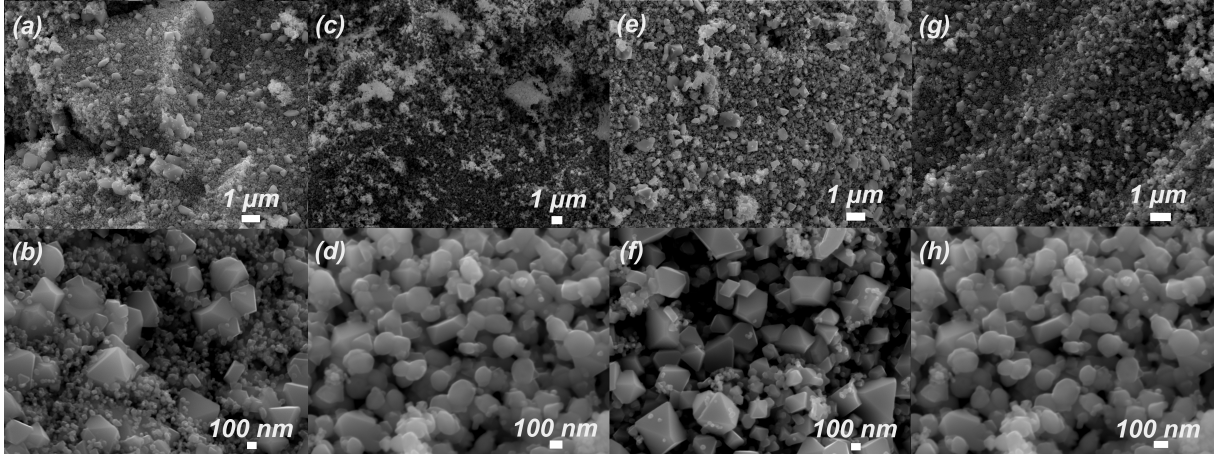


Figure 5.1: Scanning electron microscope images of as-synthesized (post-annealing) cobalt ferrite crystals. (a-b) show crystals from a 100%-scale reaction performed at the standard 90 °C , while (c-d) show crystals for the same scale where the reaction was performed at 45 °C . (e-f) show crystals from a 25%-scale reaction, and (g-h) show crystals from a 12%-scale reaction, both synthesized at 90 °C .

CFNP sizes and shapes were analyzed by SEM, as seen in Figure 5.1. While sizes of the nanospheres present remain consistent through each reaction scale at around 60 nm, the size and shapes of larger particles differ in proportion through the samples. A summary of the SEM results is included in Table 5.1.

The 100%-scale reaction at 90 °C in Figure 5.1 (a) and (b) produces some disks 100-300 nm in size, along with many octahedra around 300-600 nm, with a few “super-sized” particles (disks and octahedra) around 1 μm in size. The smallest spheres make up a significant portion of the total particles, at around an estimated 60%. (c) and (d) show particles for the same reaction scale (100%) at 45 °C , where disks and

octahedra distributions are in equal proportion and have sizes around 100-300 nm. Interestingly, the 45 °C iteration of the 100%-scale reaction does not have any super-sized particles seen in the 90 °C synthesis products, nor a significant amount of the small nanospheres (estimated <10% total product), and instead the majority of the sample comprises of many spheres around 150 nm.

Figure 5.1 (e) and (f) show CFNP crystals from a 25%-scale synthesis where there are more fully-formed octahedra than disks (estimated 3:2), both geometries ranging in size from 300-600 nm, with super-sized particles upwards of 800 nm. The 12%-scale reaction products in (g) and (h) show no octahedral particles, instead having many disks with an average size of around 500 nm, and around 50% of the sample being comprised of nanospheres.

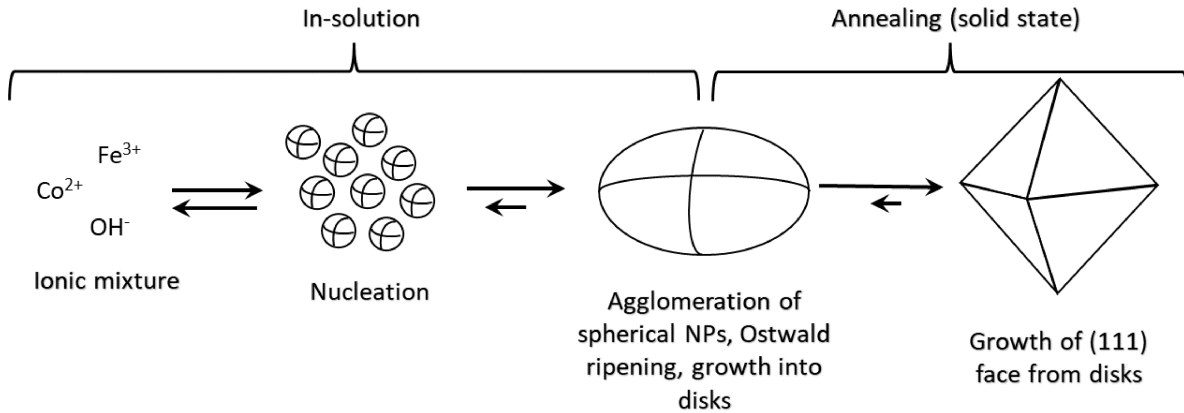


Figure 5.2: Proposed growth mechanism for the observed CFNP morphologies. Octahedra form as the stable (111) face grows from a disk, which result from the agglomeration and combining of nanospheres.

Based on the resulting morphologies observed via scaling of the synthesis, Figure 5.2 shows a proposed growth mechanism for these products. A number of reports on synthesis of cobalt ferrites note that agglomeration of small NPs into bigger groups — and eventually larger particles — is a direct result of Ostwald ripening.^{18,19} Small particles are dissolved and/or combined at the expense of larger particle growth to

minimize surface area. This results in a lower surface energy and therefore a lower overall free energy of the system. Just as solid precipitates may re-dissolve and add onto solid surfaces in solution, Ostwald ripening can also occur in the solid state, which is partially responsible for our observations with these scaling experiments.²⁰ As our final morphologies are only observed after annealing, it is clear that part of this process does occur out of solution. Thermal annealing at high temperatures provides sufficient energy for atoms to diffuse from small particles in favour of growth of larger particles.

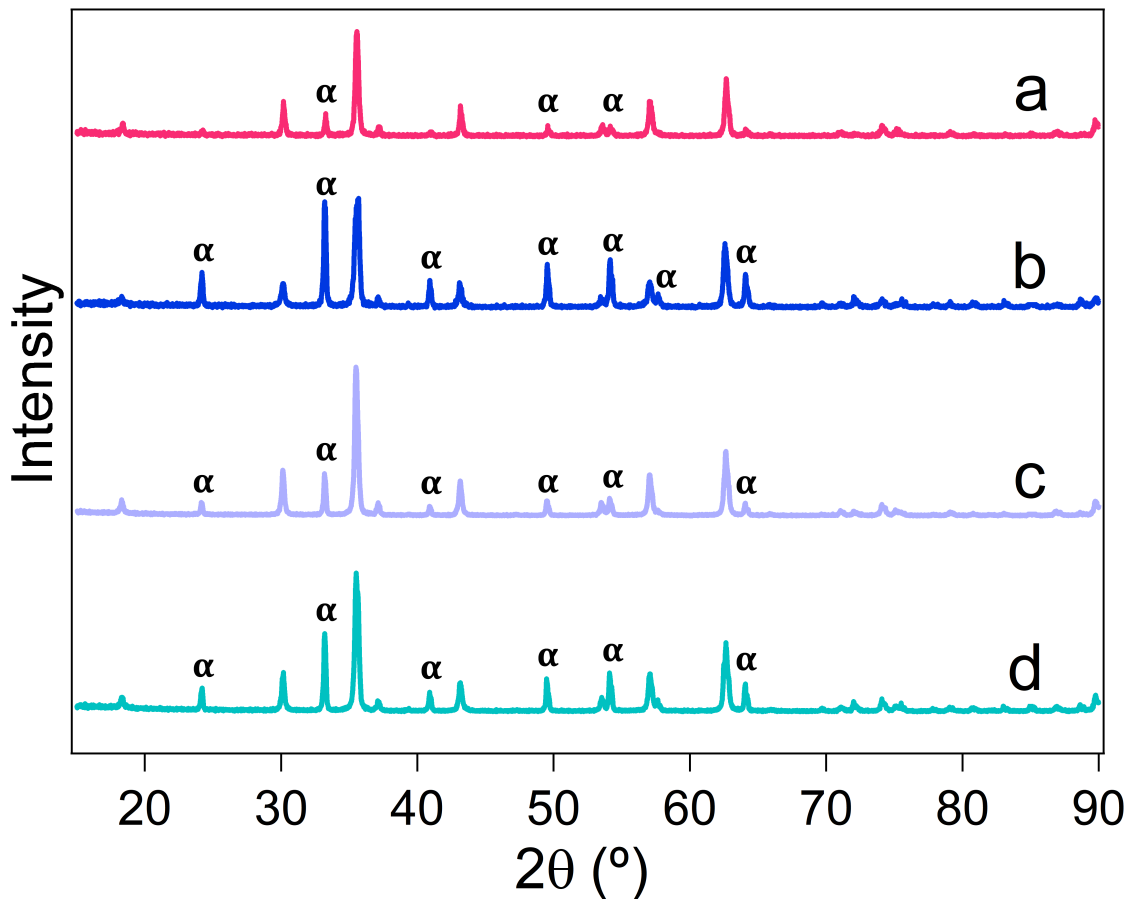


Figure 5.3: X-ray diffraction peaks for CF products. (a) 100%-scale synthesized at 90 °C (b) 100%-scale synthesized at 45 °C (c) 25%-scale (d) 12%-scale. α markers denote peaks corresponding to hematite impurities.

XRD for each scaled-product provided confirmation of an inverse spinel crystal structure present after annealing, confirmed by comparison to literature sources.^{21–23} Figure 5.3 (a-d) shows XRD data for synthesized CFNPs at 100%-scale for 90 °C and 45 °C , 25%-scale, and 12%-scale, respectively. The α markers denote hematite (α -Fe₂O₃) impurities. Jade (MDI JADE Pro (MDI, 2019)),²⁴ a software package for analysis of XRD data in conjunction with a database of powder patterns, calculated that 57% of the signal in the 100%-scale 45 °C sample was hematite, with the lowest hematite impurities found in the 100%-scale 90 °C (19%). As explained further below, these are not true compositional percentages of the samples but rather an estimate of composition of the most crystalline portions of the sample.

| Peak (hkl) | Sample | 2θ (°) | d (Å) | a (Å) |
|------------|-----------|---------------|-------|-------|
| (4 0 0) | 100% 90°C | 43.16 | 2.094 | 8.377 |
| | 100% 45°C | 43.08 | 2.098 | 8.392 |
| | 25% | 43.14 | 2.095 | 8.381 |
| | 12% | 43.10 | 2.097 | 8.388 |
| (4 4 0) | 100% 90°C | 62.66 | 1.481 | 8.380 |
| | 100% 45°C | 62.56 | 1.484 | 8.392 |
| | 25% | 62.64 | 1.482 | 8.383 |
| | 12% | 62.64 | 1.482 | 8.383 |

Table 5.3: The (400) and (440) peaks for this cubic structure were used to calculate distance, d, and lattice parameter, a, for the various scaled CF products. As the NP synthesis is scaled down, d and a both increase, which may be due to metal ion occupancy changes in the crystal, as Fe₃⁺ has a larger radius than that of Co²⁺.

Table 5.3 shows calculated values for the distance between planes (d) and the resultant lattice parameter (a), both reported in Å, for peaks of indices (400) and (440). The peak locations of the indices differ for each scaled NP product, resulting in differences in the calculated lattice values. There is no clear trend that is consistent for both peaks, but the smallest lattice sizes are associated with 100%-scale CFNPs, which may be due to changes in metal occupation. Any one metal in an inverse spinel structure may either migrate to a new geometry (tetrahedral to octahedral, or

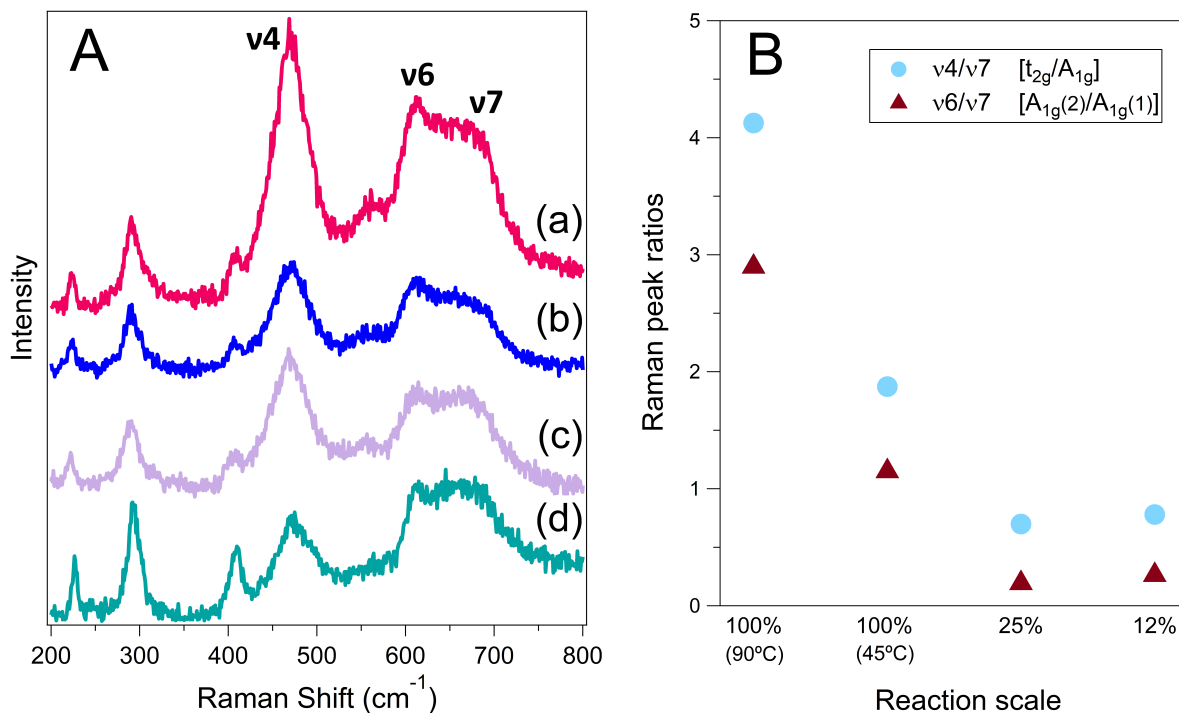


Figure 5.4: Part (A): Raman spectra of bulk CF crystals (a) 100%-scale synthesized at 90 °C (b) 100%-scale synthesized at 45 °C (c) 25%-scale (d) 12%-scale. Part (B): Ratios of Raman peak areas for ν_4 and ν_6 compared with ν_7 (roughly 470 cm^{-1} , 620 cm^{-1} , and 670 cm^{-1} , respectively) as synthesis reaction scale changes. Peak area values are averaged over triplicate data-sets, with peaks fit to a Gaussian.

vice versa), or occupy more/fewer sites in their original coordination. With this in mind, the varied lattice size may be the result of changes in Co^{2+} occupation within the crystal as the reaction is scaled. Co^{2+} is a smaller metal ion of the two in the structure and is typically found octahedrally coordinated in the CoFe_2O_4 structure, so changes in either the coordination site or amount of vacancy of Co^{2+} could explain the changes in lattice distances and parameters through the syntheses, though further experimentation and analysis is required to draw a complete conclusion.???

Despite notable amounts of hematite in the XRD data, analysis via Raman spectroscopy (Figure 5.4A) showed that the bulk crystal has an inverse spinel structure. This indicates that the strong signal of hematite in the XRD data is due to its highly

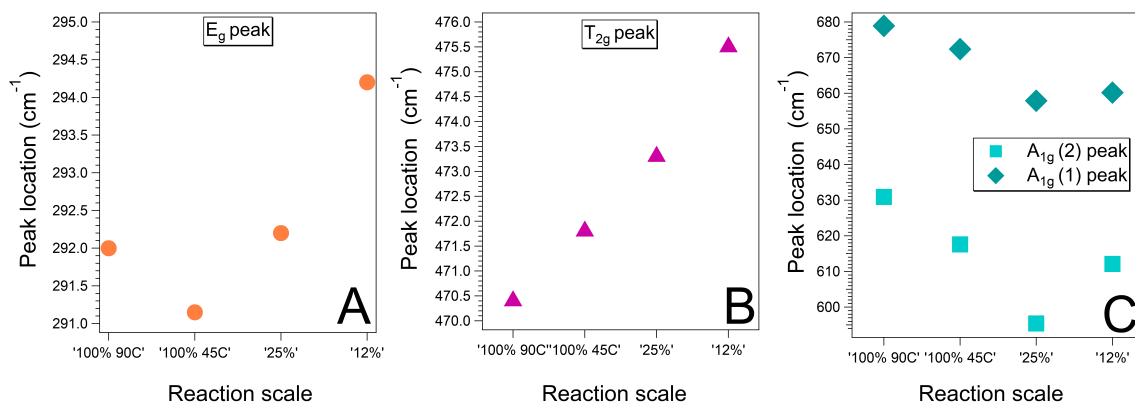


Figure 5.5: Raman peak analysis for CFNPs showing shifting of peaks with decreasing reaction scale. The E_g mode (A) remains largely the same throughout the scales, with a net difference of 3 cm^{-1} . The T_{2g} mode (B) shifts to a higher wavenumber as reaction scale is decreased, while the two A_{1g} modes (C) shift to lower wavenumbers as scale is decreased.

crystalline nature; it is not in fact a significant product, which would be notable in the Raman spectrum if present.²⁵ Additionally, the Raman data for the synthesized products helped elucidate the type of inverse spinel crystal present, as XRD typically cannot distinguish specifically between Fe_3O_4 , $\gamma\text{-Fe}_2\text{O}_3$, and CoFe_2O_4 , which have differences in cation distributions/vacancies.²⁶⁻²⁸

The Raman also gives us insight into what is changing in the crystal structure as the reaction is scaled down. Figure 5.4B shows the trends in peak areas for major Raman modes (T_{2g} , $A_{1g}(1)$, and $A_{1g}(2)$) of CFNPs from each reaction. The $A_{1g}(1)$ mode arises from vibrations of the T_d sublattice (symmetric stretching of oxygen with respect to the T_d centre²⁸), while the T_{2g} mode is due to vibrations in O_h sublattice (symmetric and antisymmetric oxygen bending²⁸).^{29,30} As the reaction is scaled down, the T_{2g} peak diminishes significantly, while the $A_{1g}(2)$ slightly decreases. The change at ν_4 signifies major changes at O_h sites, corresponding to decreased Co^{2+} occupation as the reaction is scaled down.³¹

As well as trends in peak area, reaction scale also results in the shift of the four

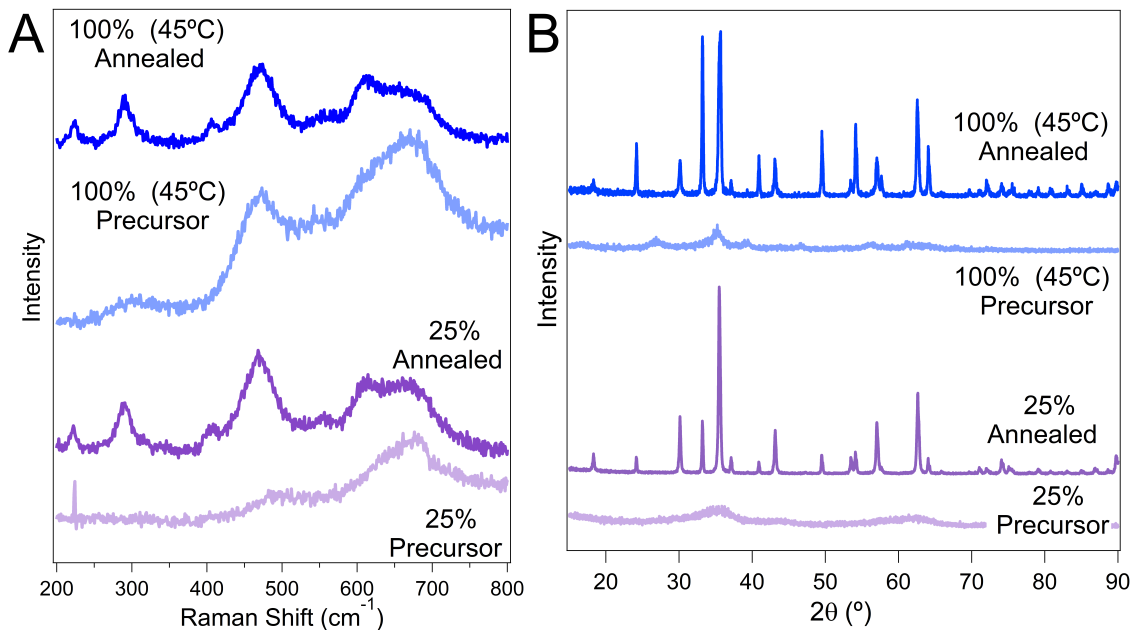


Figure 5.6: (A): Raman spectra of CF crystals before (precursor product) and after annealing for 100%-scale at 45 °C and 25%-scale. (B): Corresponding XRD data for products before and after annealing.

most significant Raman peaks. Table 5.2 shows Raman peak locations for the E_g , T_{2g} , and two A_{1g} modes; the peak shifting trends are visualized in Figure 5.5. The E_g peak in Figure 5.5(A) associated with octahedral sites^{25,28} doesn't considerably shift, remaining ± 2 cm^{-1} from the median value of 292 cm^{-1} though generally trending to a higher wavenumber as the reaction scale decreases. The T_{2g} mode (B) is also associated with octahedral sites, and similarly shifts to a higher wavenumber as the reaction scale decreases. The shifts of both the E_g and T_{2g} modes to higher wavenumber (and therefore higher energies) indicate changes at octahedral sites, potentially due to an increased proportion of Fe^{3+} occupancy. The two A_{1g} modes (C) shift to lower wavenumbers (higher energies) with decreasing reaction scale. The biggest difference for these modes is seen between the 100% (90°C) and 25% A_{1g} peaks, with a shift from 630.9 cm^{-1} to 595.4 cm^{-1} (Δ 35.5 cm^{-1}) for A_{1g} (2), and from 678.9 cm^{-1} to 657.9 cm^{-1} (Δ 21.0 cm^{-1}) for A_{1g} (1).

| Scale | M_S (emu/g) | H_c (Oe) | M_r (emu/g) | Squareness |
|---------------|---------------|------------|---------------|------------|
| 100% (90 °C) | 57.2 | 1200 | 25.296 | 0.4420 |
| 100% (45 °C) | 29.3 | 1400 | 11.9780 | 0.4080 |
| 25% | 53.9 | 0 | 0.617 | 0.0114 |
| 12% | 48.5 | 0 | 1.6537 | 0.0362 |

Table 5.4: Magnetic parameters for each CFNP synthesis, showing changes in saturation, coercivity, remanence, and squareness as the reaction is scaled.

Further insight into the crystal structure and growth can be seen when comparing precursor and post-annealing products. Figure 5.6A shows a snapshot of Raman spectra before and after annealing for two of the scales, 100% at 45 °C and 25%, while part B shows equivalent XRD data. Raman of both precursors shows strong presence of the A_{1g} peak around 668cm^{-1} associated with T_d geometry, while the 100% (45 °C) additionally has a significant T_{2g} peak at around 668cm^{-1} . The XRD data (Figure 5.6B indicates that the 25% precursor product is amorphous, while that for the 100% (45 °C) is crystalline in nature. This is likely to be attributed to the lower reaction temperature, allowing for slower growth of crystals. After annealing, both products exhibit high crystallinity.

Along with geometry changes, the NPs from each scaled reaction exhibit differences in their magnetic properties. Figure 5.7 shows magnetic hysteresis curves for each scaled product, and how they each respond to the applied field. Magnetic saturation values (M_S) indicate the maximum magnetic strength of a material when all domains are aligned via an external field, noted as the maximum y-value plateau in a VSM curve.³² While M_S values for 100% (90 °C), 25%, and 12% scales were found to be relatively similar (Table 5.4), the 100% (45 °C) deviates from the rest with a M_S value of 29 emu/g, likely due to slower crystal growth at the lower temperature affecting domain size.^{33,34}

While it may seem a hematite impurity is potentially responsible for the drop in saturation magnetization, being an anti-ferromagnetic material, again the confirma-

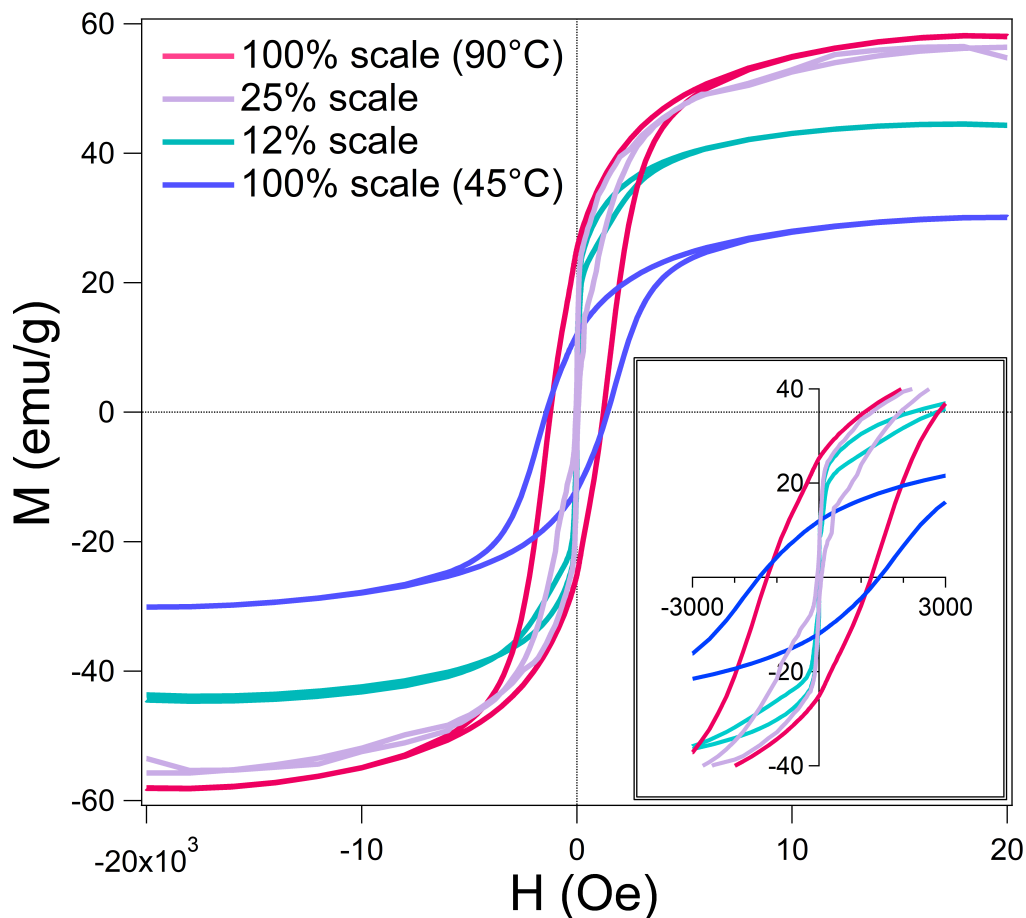


Figure 5.7: Magnetic hysteresis curves for CF crystals synthesized at 100%-scale at both 90 °C and 45 °C , 25%-scale, and 12%-scale. The saturation values for each sample are listed in the inset.

tion from Raman spectral analysis shows us that any hematite present is a negligible minority. A minority phase can show significant signal in XRD if that phase is highly crystalline.

Remanence (M_R) refers to the magnetic field a material retains when no external field is applied, while coercivity (H_C) represents the field required (in the opposing direction) to de-magnetize the material.³⁵ The M_R and H_C values differs greatly between the scaled products (Table 5.4, visualized in the inset of Figure 5.7. The M_R value is largest for the 100%-scale products, with a M_R of 25 emu/g for the 90 °C

product and 12 emu/g for the 45 °C product, while the scaled-down 25% and 12% products have M_R values of 0.62 emu/g and 1.6 emu/g respectively. The 25% and 12% crystals additionally exhibit no coercivity (closed hysteresis loop), which others have attributed to superparamagnetic behaviour.³³ Both 100%-scale products differ from this, exhibiting open hysteresis loops with H_C values of 1400 Oe (45 °C) and 1200 Oe (90 °C), behaving as so-called “permanent” magnets.

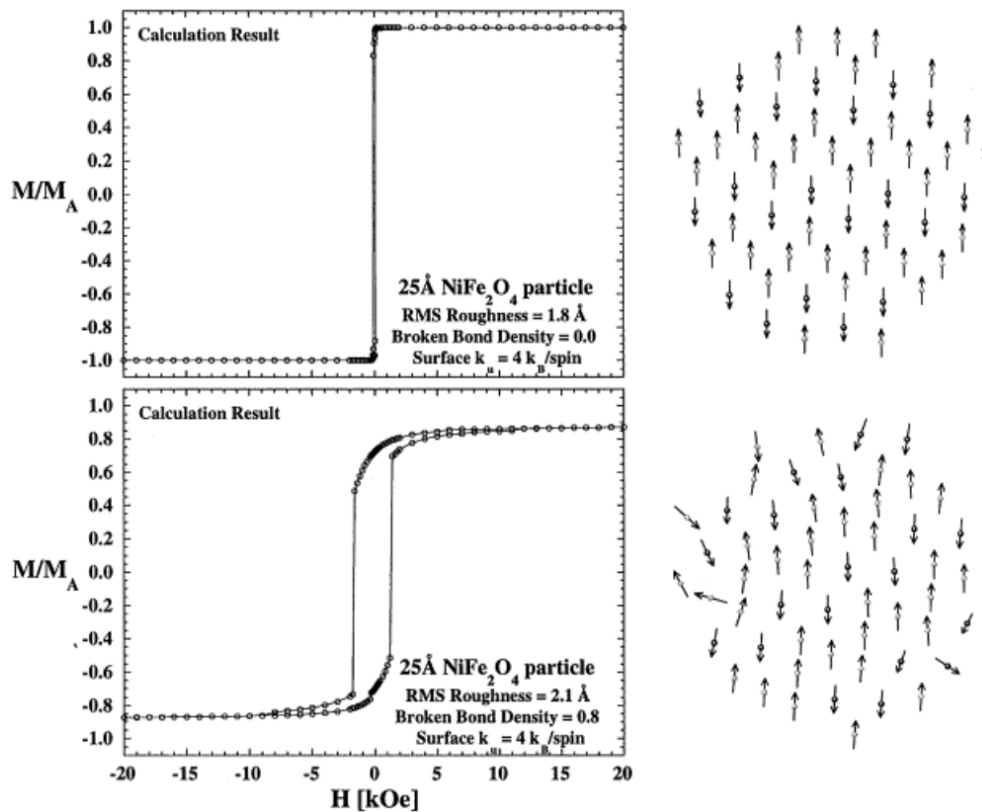


Figure 5.8: Simulated VSM curves for an inverse spinel (NiFe_2O_4) with nanoscale particle size, showing resultant curves for single-domain particles (top) versus multi-domain (bottom). Reprinted from *Journal of Magnetism and Magnetic Materials*, R. H. Kodama, “Magnetic Nanoparticles”, 200, 359-372, (1999), with permission from Elsevier.

By definition, a single-domain material cannot have a coercivity. Single-domain materials (such as superparamagnetic particles) undergo a rapid and efficient flip of directional spins, and remain aligned until an opposing field influences them. Figure 5.8

from Kodama (1999)³⁶ illustrates this for calculated hysteresis loops of a nickel ferrite, analogous to CF in structure. This illustrates how some magnetic boundaries (ie. domains) are required for net electron spins in >1 direction, creating permanent magnetism and therefore coercivity.

To further elaborate, the clearest trend for the scaled products and their associated magnetic characteristics is seen in the squareness, which is the ratio of magnetic remanence (M_R) to saturation (M_S). Specifically, M_R indicates the net magnetic moment per unit of material when the applied field is removed. As seen in Table 5.4, the squareness of the 90 °C and 45 °C 100%-scale products are similar, with the higher reaction temperature having a slightly larger squareness value than the lower temperature (0.4424 vs 0.4084, respectively). The value for squareness of the 25%-scale reaction is 0.1387, almost 3x smaller than that of the largest value, while for 12%-scale the squareness is 0.0362, an order of magnitude less than the largest value.

In summarizing the characterization of the particles throughout all scales of syntheses, it is important to note that the initial nucleation and subsequent growth of particles in the reaction mixture determines the final product. Annealing of the precursor product is necessary to obtain the highly-crystalline inverse spinel, but the annealing conditions remain the same across all trials. The differences in NP products are therefore determined earlier than the annealing step, indicating the nucleation in solution is the key factor.

5.3.2 Altering synthesis parameters beyond scale

5.3.3 Sensor design

The design process for the sensing platform utilizing magnetic NPs is outlined in Chapter 2. This final procedure was used to fabricate the CF version of the sensor as well.

As a proof-of-concept measure, all components of the working sensor were isolated and tested to assess individual-performance versus composite-performance. Figure 5.9 shows isolated spectra for the Au base-layer and CFNPs (100%-scale at 90 °C , patterned on glass alone and non-patterned on Au), both as blanks and exposed to 1 ppm phenanthrene, which primarily show fluorescence and/or CFNP signal, and no enhancement is visible. When all components are combined as described in 5.2.4, strong enhancement is observed. It is clear that each layer plays a role in successful enhancement, and is particularly notable that the patterning of the NPs (and not simply their presence) is crucial for the powerful enhancement of the whole platform.

This method of magnetic patterning results in a complex multi-layer, and within these layers are where sensing occurs. The Raman laser collects strong SERS spectra only when set within the layers; collecting while focused on the base Au surface results in either very poor peak intensity from the analyte, or only seeing glass fluorescence. The complex topography also allows for a multitude of adhesion sites for the organic analyte.

5.3.4 Sensor performance

Pattern directionality of the magnetic NPs (Figure 5.11, (a) middle versus (b) outer edge), as mediated by the external field during the fabrication process, does not influence the quality of SERS data collected. Data collected from any location of the

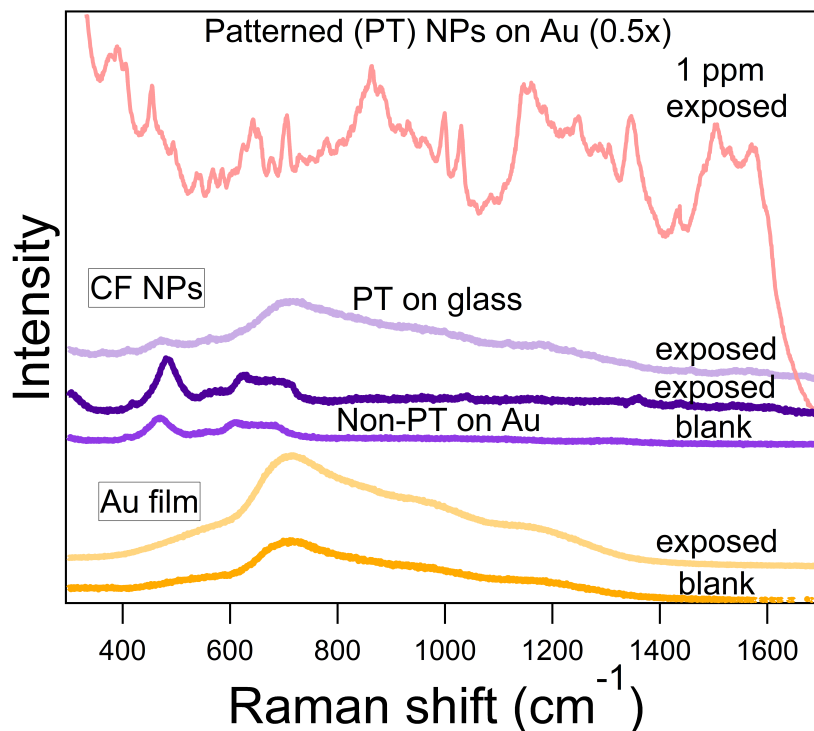


Figure 5.9: Separation of Au film and CFNPs, showing how each behave under testing conditions of the working sensor. Annealed Au is shown as a blank and exposed layer, while the same is done for CFNPs (both patterned and a non-patterned equivalent), all of which display glass fluorescence or NP signal and no visible enhancement of the loaded 1 ppm phenanthrene. When all components are combined (top spectrum), enhancement of the analyte is successful (spectrum scaled down 0.5x)

surface gives reproducible results, noted in Figure 5.10. Instead, the type of NPs is the determining factor for SERS performance on any given substrate.

Figure 5.12 shows SERS spectra for substrates made with CFNPs from the major scaled-syntheses (100%, 25%, & 12%), exposed to 1 ppm (left) and 1 ppb (right) phenanthrene. The 100%-scale CFNPs consistently exhibit the strongest enhancement at the ppm level, with an average SNR of 4.33 dB for 1 ppm of phenanthrene, and the max SERS peak of 4.49 dB. The 25%- and 12%-scale CFNPs then follow, respectively, with SNRs of 4.12 dB and 4.11 dB. For ppb trials, 100%-scale substrates exhibit an average enhancement of 3.38 dB, while 25% had an average SNR of 3.87 dB, and 12%

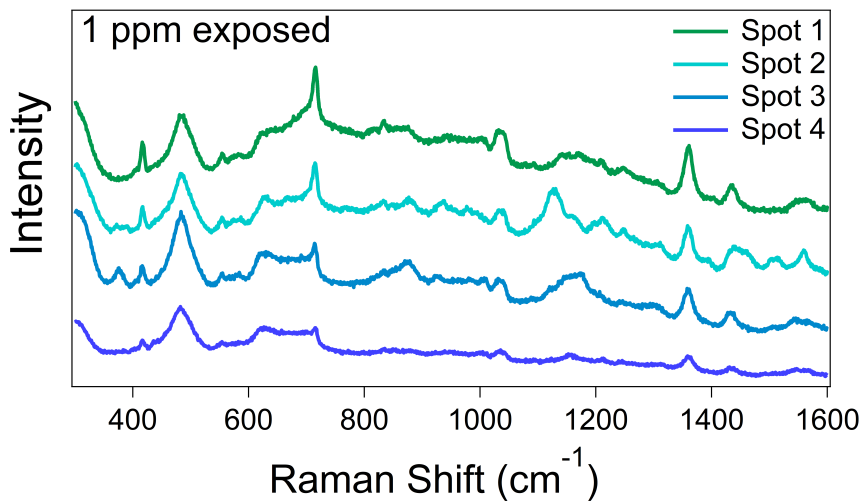


Figure 5.10: SERS spectra collected from various locations across a substrate, exposed to 1 ppm of phenanthrene. Signal is consistent and strong at all points on the surface, with no preferential location.



Figure 5.11: Optical images stitched together, showing the patterning across the surface of a finished substrate. Sensing differences at locations (a) or (b) are negligible, indicating there is no preferential spot for spectral acquisition.

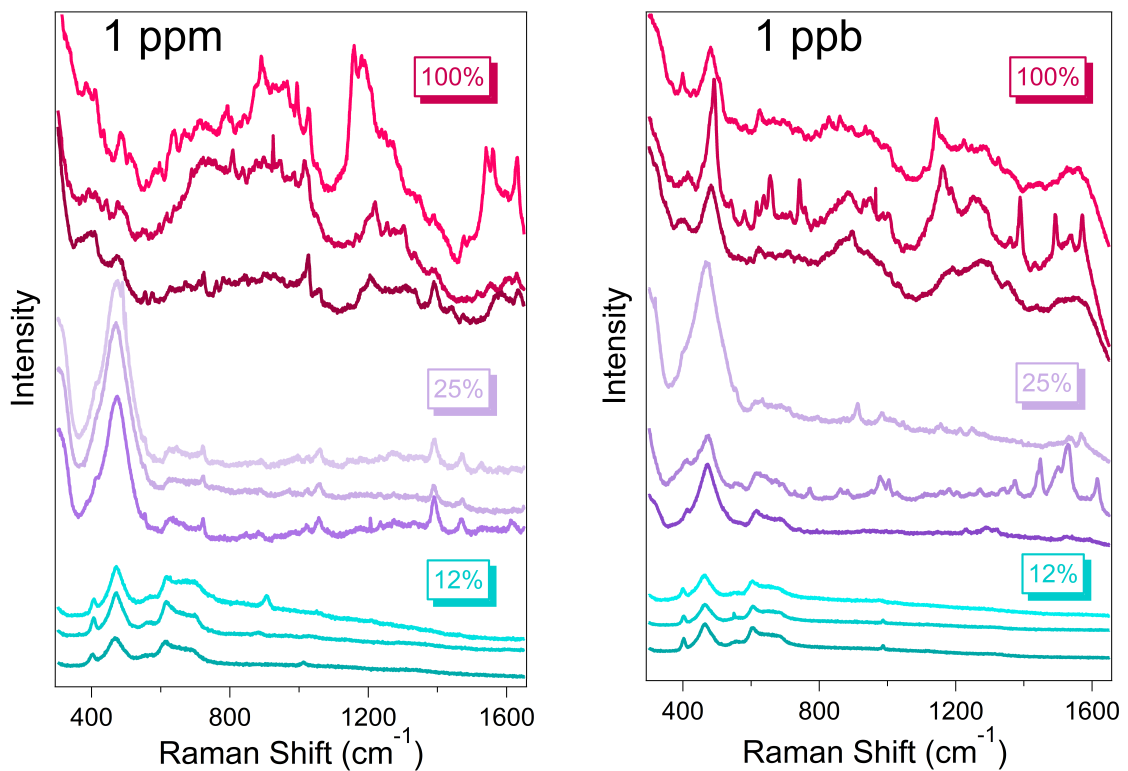


Figure 5.12: SERS performance of substrates made with the various scales of CFNPs, exposed to phenanthrene. Both the 1 ppm (left) and 1 ppb (right) tests show differences in SERS enhancement between the various synthesis products, where the 100%-scale crystals provide the best enhancing environment for each concentration of PAH tested.

with an SNR of 3.56 dB. These averages for 1 ppb were the same magnitude across all substrates, with a maximum SERS peak from the 100%-scale substrate at 4.33 dB.

There are a few variables that contribute to these differences in SERS performance. Referring back to Table 5.1, the 100%-scale and 25%-scale CFs exhibit the same geometries with some similar distributions - many small nanospheres making up 50%-60% of the sample, with the remainder being large octahedra and disks. The 25%-scale, however, has a higher proportion of large disks than octahedra, and the average disk size is also larger than that of the 100%-sample at 700 nm. These samples also differ in maximum particle size, where the 100%-scale product has octahedra upwards of 1 μm in size, while the max size in the 25% product are disks around 850 nm.

It is well-known that geometry plays a very important role in plasmonic enhancement, as shapes with angular components (cubes, stars, octahedron, etc.) allow for greater electron density at edges or points.³⁷⁻³⁹ With this in mind, it follows that the edges of the octahedra provide hot-spots, as compared to the rounded surfaces of the disks or spheres.

5.3.5 Magnetic field application during spectral acquisition

Along with geometry differences, the difference in permanent magnetism (M_R between the 100%-scale products and the 25%- and 12%-scale products) is a significant factor in the observed SERS performance. Figure 5.14 shows the calculated SNR values plotted against the magnetic characteristics of the CFNPs used in the sensor, to determine if any clear correlation can be noted. No clear trends are seen through all samples, though there may be some correlation between high remanence, high coercivity, and high SNRs when a magnetic field is applied. The error bars associated with the calculated SNR statistics clearly show that more data needs to be acquired for conclusions to be drawn. While further replicate and mechanistic studies are war-

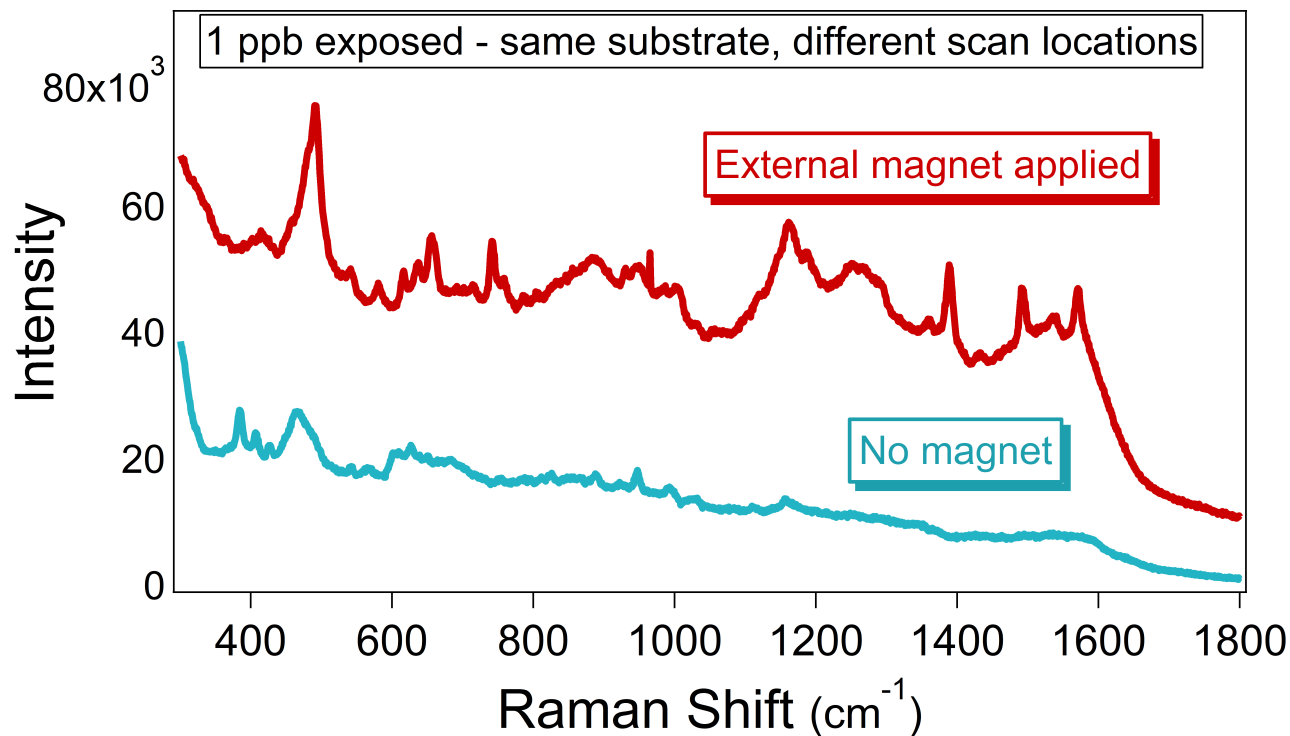


Figure 5.13: Raman spectra showing the effects of applying a magnetic field during spectral acquisition. The bottom spectrum shows un-assisted SERS enhancement of 1 ppb phenanthrene on a sensor made with 100%-scale CFNPs, while the top spectrum shows enhancement from the same substrate with a magnet applied to the underside of the sensing substrate during collection.

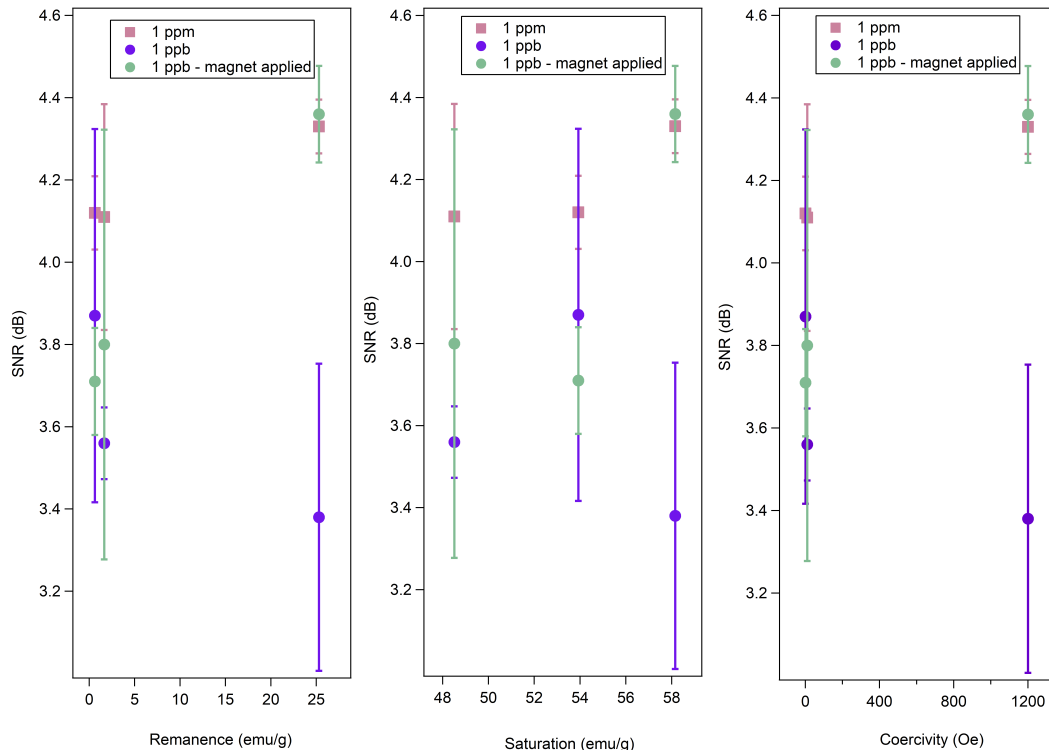


Figure 5.14: When comparing resulting SNRs against magnetic characteristics M_R , M_S , and H_C of the CFNP particles, no trends in the data are apparent. Given the associated error bars for each calculated SNR value, it is clear that more data is required before anything conclusive could be said.

ranted to explore this overall interaction more for uses in plasmonic sensing, principle proof-of-concept tests in applying this external field were performed to assess such a magnetic contribution.

Figure 5.13 shows a spectrum from a 1 ppb exposed CFNP substrate displaying SERS enhancement (bottom), and the same substrate with a magnet applied during spectral acquisition (top). These are necessarily in different locations on the surface, as adding the magnet requires moving the sample. When an external field is applied, the intensity triples in number of counts, indicating increased enhancement over that of the plasmonic surface alone. There is a notable increase in SNRs for most substrates under these conditions, with the average from the 100%-scale substrate in-

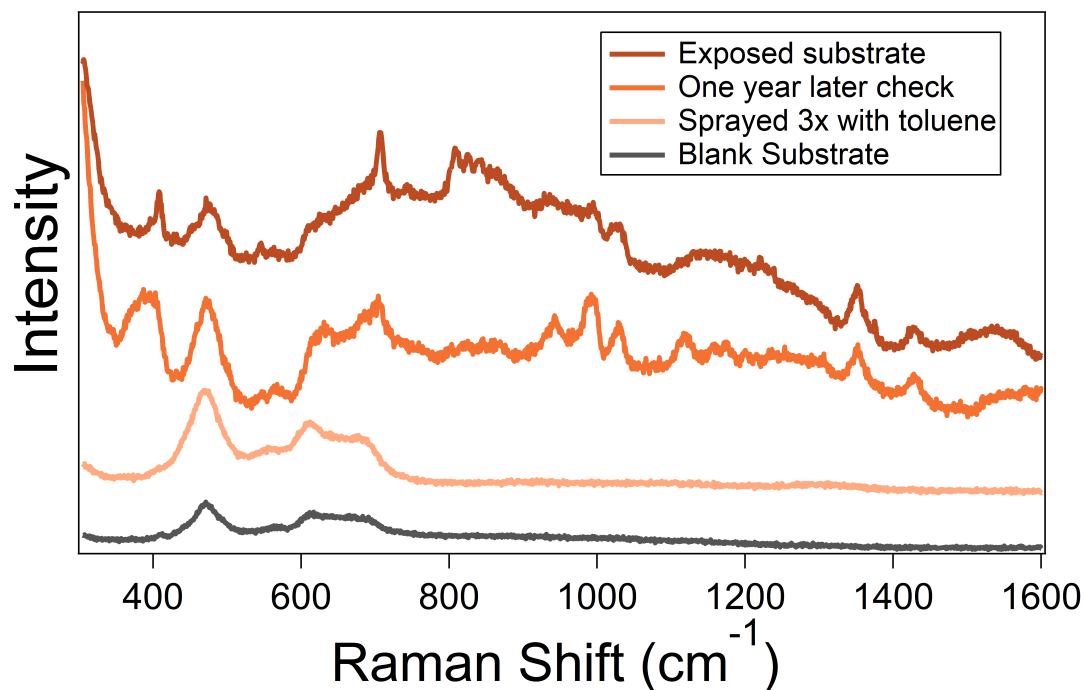


Figure 5.15: Comparison of freshly-exposed CFNP substrate (1 ppm phenanthrene; top) to the same surface checked one year later (2nd from top), showing surface activity which compares to a fresh exposure. The second last spectrum shows the one-year-later exposed substrate after washing with toluene (x3), showing removal of all detectable analyte.

creasing from 3.38 to 4.36 dB. Not all of those increases are statistically significant, as determined from pair-wise t-tests comparing performance with and without the applied magnetic field. The only statistically significant difference with and without the magnet was for the 100%-scale substrate, the one with the largest remanence and coercivity. An external magnetic field alone enhanced the SERS response by a full order of magnitude, as no other changes occurred between acquisitions.

Reusability and archival use

With practical sensing in mind, assessing metrics like archival nature and reusability of a substrate are important for future usage. Reliable surfaces are important for record-keeping, with assurance materials will not degrade in a period of time and lose

function, while reusability is important regarding costs and environmental impact.

Figure 5.15 shows spectra of a new substrate exposed to analyte compared to the same surface one year later (top two spectra, respectively), in order to assess longevity of the surface as an enhancing environment, stored under ambient conditions with no specialized environment. After a year, enhancement is comparable to that of the freshly-exposed substrate, indicating that the surface is very stable and reliable.

To assess reusability (for at least one cycle), the exposed substrate was actively washed in triplicate with pure toluene. After washing, a spectrum of the surface collected was compared to that of a newly fabricated substrate, showing that analyte peaks were no longer present on the surface.

5.4 Conclusions

We synthesized four different scaled products of cobalt ferrite nanoparticles, through pH-mediated precipitation. In characterizing the materials, it was determined that changing the reaction scale alters particle geometries and magnetic characteristics, due to changes in crystal growth conditions and metal ion occupancies in the crystal structure.

The products were then integrated into a plasmonic sensing surface design for SERS, using magnetic patterning to create a hierarchical multi-layer of the NPs. Performance of the sensors were assessed and compared, using the PAH phenanthrene as an analyte of interest. The scale with the biggest maximum particle size and largest magnetic remanence provided the largest amount of enhancement, with a max SNR of 4.49 dB. A proof-of-concept test was also performed to test impact of an applied magnetic field on the sensing surface during Raman collection, where intensity was found to increase threefold with with the additional field, and SNRs increased by a

full order of magnitude with statistically-significant difference when compared to the same sensor without the field applied.

Additional tests were performed to assess viability of archival use of these sensors, along with reusability. The surfaces are stable for at least one year, performing comparably with newly fabricated sensors without having to be stored under special environmental conditions. The substrates are also reusable, following simple rinsing using a non-polar solvent.

The implications of magnetic influence towards significant plasmonic enhancement, particularly when involving magnetic materials within the design, are highly important and require further study. As well, the overall variety of geometries, along with presence of angular disk shapes and elongated octahedra into prisms, gives insight into the crystal growth mechanism which can be explored in future experimentation.

5.5 Acknowledgement

This research was conducted on the island of Newfoundland, the ancestral homeland of the Beothuk and the unceded ancestral and current land of the Mi'kmaq. The authors thank the Natural Science and Engineering Council of Canada (NSERC, DG program) for operating funds, The Canada Foundation for Innovation (CFI) for instrumentation funding, and the School of Graduate Studies of Memorial University of Newfoundland for a stipend for SMVG. We also thank Prof. K. Poduska (Physics) for VSM access, and Dr. W. Aylward (CREAIT) for SEM and EDX access, sample preparation for SEM, EDX and pXRD, and for operation of the XRD facility.

Bibliography

- [1] Abd Elrahman, A. A.; Mansour, F. R. Targeted magnetic iron oxide nanoparti-

- cles: Preparation, functionalization and biomedical application. *J. Drug Deliv. Sci. Technol.* **2019**, *52*, 702–712.
- [2] Kabe, Y.; Sakamoto, S.; Hatakeyama, M.; Yamaguchi, Y.; Suematsu, M.; Itonaga, M.; Handa, H. Application of high-performance magnetic nanobeads to biological sensing devices. *Anal. Bioanal. Chem.* **2019**, *411*, 1825–1837.
- [3] Zhang, H.; Wu, J. R.; Wang, X.; Li, X. S.; Wu, M. X.; Liang, F.; Yang, Y. W. One-pot solvothermal synthesis of Carboxylatopillar[5]arene-modified Fe₃O₄ magnetic nanoparticles for ultrafast separation of cationic dyes. *Dye. Pigment.* **2019**, *162*, 512–516.
- [4] Puente-Santiago, A. R. *Surface-modified Nanobiomaterials Electrochem. Biomed. Appl.*; 2020; pp 49–91.
- [5] Wu, W.; Wu, Z.; Yu, T.; Jiang, C.; Kim, W.-S. Recent progress on magnetic iron oxide nanoparticles: synthesis, surface functional strategies and biomedical applications. *Sci. Technol. Adv. Mater.* **2015**, *16*, 023501.
- [6] Nguyen, T. T.; Mammeri, F.; Ammar, S. Iron oxide and gold based magnetoplasmonic nanostructures for medical applications: A review. *Nanomaterials* **2018**, *8*, 149.
- [7] Fahmy, H. M.; Abd El-Daim, T. M.; Ali, O. A.; Hassan, A. A.; Mohammed, F. F.; Fathy, M. M. Surface modifications affect iron oxide nanoparticles' biodistribution after multiple-dose administration in rats. *J. Biochem. Mol. Toxicol.* **2021**, *35*, 1–10.
- [8] Hou, Z.; Liu, Y.; Xu, J.; Zhu, J. Surface engineering of magnetic iron oxide nanoparticles by polymer grafting: Synthesis progress and biomedical applications. *Nanoscale* **2020**, *12*, 14957–14975.

- [9] Karaagac, O.; Bilir, B.; Köçkar, H. The influence of synthesis parameters on one-step synthesized superparamagnetic cobalt ferrite nanoparticles with high saturation magnetization. *J. Magn. Magn. Mater.* **2019**, *473*, 262–267.
- [10] Khanra, S.; Mamun, A.-a.; Ferreira, F. F.; Ghosh, K.; Guha, S. Functionalized Self-Assembled Peptide Nanotubes with Cobalt Ferrite Nanoparticles for Applications in Organic Electronics. *Appl. Nano Mater.* **2018**, *1*, 1175–1187.
- [11] Mumtaz, M.; Hassan, M.; Ahmad, Z. Nanohybrids of multi-walled carbon nanotubes and cobalt ferrite nanoparticles : High performance anode material for lithium-ion batteries. *Carbon N. Y.* **2021**, *171*, 179–187.
- [12] Joshi, S.; Kamble, V. B.; Kumar, M.; Umarji, A. M.; Srivastava, G. Nickel substitution induced effects on gas sensing properties of cobalt ferrite nanoparticles. *J. Alloys Compd.* **2016**, *654*, 460–466.
- [13] Reza, A.; Naseri, M.; Mohamed, H. Surface plasmon resonance sensor for detecting of arsenic in aqueous solution using polypyrrole-chitosan-cobalt ferrite nanoparticles composite layer. *Opt. Commun.* **2017**, *383*, 132–137.
- [14] Liu, X.; Yang, X.; Li, K.; Liu, H.; Xiao, R.; Wang, W.; Wang, C.; Wang, S. Sensors and Actuators B: Chemical Fe₃O₄@Au SERS tags-based lateral flow assay for simultaneous detection of serum amyloid A and C-reactive protein in unprocessed blood sample. *Sensors Actuators B. Chem.* **2020**, *320*, 128350.
- [15] Colom, R.; Devilez, A.; Bonod, N.; Stout, B. Optimal interactions of light with magnetic and electric resonant particles. *Phys. Rev. B* **2016**, 1–8.
- [16] Guclu, C.; Veysi, M.; Darvishzadeh-Vercheie, M.; Capolino, F. Optical nanoantennas as magnetic nanoprobles for enhancing light-matter interaction. 2016 10th

International Congress on Advanced Electromagnetic Materials in Microwaves and Optics (METAMATERIALS). 2016; pp 391–393.

- [17] Massart, R. Preparation of Aqueous Magnetic Liquids in Alkaline and Acidic Media. *IEEE Trans. Magn.* **1981**, *17*, 1247–1248.
- [18] V. Chandekar, K.; Mohan Kant, K. Synthesis and characterization of low temperature superparamagnetic cobalt ferrite nanoparticles. *Adv. Mater. Lett.* **2017**, *8*, 435–443.
- [19] Jovanović, S.; Spreitzer, M.; Tramšek, M.; Trontelj, Z.; Suvorov, D. Effect of oleic acid concentration on the physicochemical properties of cobalt ferrite nanoparticles. *J. Phys. Chem. C* **2014**, *118*, 13844–13856.
- [20] Alloyeau, D.; Prévot, G.; Le Bouar, Y.; Oikawa, T.; Langlois, C.; Loiseau, A.; Ricolleau, C. Ostwald ripening in nanoalloys: When thermodynamics drives a size-dependent particle composition. *Phys. Rev. Lett.* **2010**, *105*, 1–4.
- [21] Kumar, L.; Kumar, P.; Narayan, A.; Kar, M. Rietveld analysis of XRD patterns of different sizes of nanocrystalline cobalt ferrite. *Int. Nano Lett.* **2013**, *3*, 1–12.
- [22] Kharat, P. B.; Somvanshi, S. B.; Khirade, P. P.; Jadhav, K. M. Effect of magnetic field on thermal conductivity of the cobalt ferrite magnetic nanofluids. *J. Phys. Conf. Ser.* **2020**, *1644*.
- [23] Wang, P.; Toledo, D.; Zhang, E.; Telusma, M.; McDaniel, D.; Liang, P.; Khizroev, S. Scanning probe microscopy study of cobalt ferrite-barium titanate coreshell magnetoelectric nanoparticles. *J. Magn. Magn. Mater.* **2020**, *516*, 167329.

- [24] Gates-Rector, S.; Blanton, T. The Powder Diffraction File: a quality materials characterization database. *Powder Diffraction* **2019**, *34*, 352–360.
- [25] Fan, X.; Guan, J.; Cao, X.; Wang, W.; Mou, F. Low-temperature synthesis, magnetic and microwave electromagnetic properties of substoichiometric spinel cobalt ferrite octahedra. *Eur. J. Inorg. Chem.* **2010**, 419–426.
- [26] Stodt, M. F.; Liu, C.; Li, S.; Mädler, L.; Fritsching, U.; Kiefer, J. Phase-selective laser-induced breakdown spectroscopy in flame spray pyrolysis for iron oxide nanoparticle synthesis. *Proc. Combust. Inst.* **2021**, *38*, 1711–1718.
- [27] Cui, H.; Liu, Y.; Ren, W. Structure switch between α -Fe₂O₃, γ -Fe₂O₃ and Fe₃O₄ during the large scale and low temperature sol-gel synthesis of nearly monodispersed iron oxide nanoparticles. *Adv. Powder Technol.* **2013**, *24*, 93–97.
- [28] Chandramohan, P.; Srinivasan, M. P.; Velmurugan, S.; Narasimhan, S. V. Cation distribution and particle size effect on Raman spectrum of CoFe₂O₄, volume = 184, year = 2011,. *J. Solid State Chem.* 89–96.
- [29] Puli, V. S.; Adireddy, S.; Ramana, C. V. Chemical bonding and magnetic properties of gadolinium (Gd) substituted cobalt ferrite. *J. Alloys Compd.* **2015**, *644*, 470–475.
- [30] Silva, M. D.; Silva, F. C.; Sinfrônio, F. S.; Paschoal, A. R.; Silva, E. N.; Paschoal, C. W. The effect of cobalt substitution in crystal structure and vibrational modes of CuFe₂O₄ powders obtained by polymeric precursor method. *J. Alloys Compd.* **2014**, *584*, 573–580.
- [31] Anjum, S.; Tufail, R.; Saleem, H.; Zia, R.; Riaz, S. Investigation of Stability and Magnetic Properties of Ni- and Co-Doped Iron Oxide Nano-particles. *J. Supercond. Nov. Magn.* **2017**, *30*, 2291–2301.

- [32] Pang, Y. L.; Lim, S.; Ong, H. C.; Chong, W. T. Research progress on iron oxide-based magnetic materials: Synthesis techniques and photocatalytic applications. *Ceram. Int.* **2016**, *42*, 9–34.
- [33] Aneesh-Kumar, K. S.; Bhowmik, R. N. Micro-structural characterization and magnetic study of $\text{Ni}_{1.5}\text{Fe}_{1.5}\text{O}_4$ ferrite synthesized through coprecipitation route at different pH values. *Mater. Chem. Phys.* **2014**, *146*, 159–169.
- [34] Rabe, K. M. *Functional Metal Oxides*; John Wiley & Sons, Ltd, 2013; Chapter 7, pp 221–244.
- [35] Houshiar, M.; Zebhi, F.; Razi, Z. J.; Alidoust, A.; Askari, Z. Synthesis of cobalt ferrite (CoFe_2O_4) nanoparticles using combustion, coprecipitation, and precipitation methods: A comparison study of size, structural, and magnetic properties. *J. Magn. Magn. Mater.* **2014**, *371*, 43–48.
- [36] Kodama, R. H. Magnetic nanoparticles. *J. Magn. Magn. Mater.* **1999**, *200*, 359–372.
- [37] Tahghighi, M.; Janner, D.; Ignés-Mullol, J. Optimizing gold nanoparticle size and shape for the fabrication of SERS substrates by means of the Langmuir–Blodgett technique. *Nanomaterials* **2020**, *10*, 1–11.
- [38] Li, X.; Lin, X.; Zhao, X.; Wang, H.; Liu, Y.; Lin, S.; Wang, L.; Cong, S. Self-assembled monolayer film of concave star-shaped Au nanocrystals as highly efficient SERS substrates. *Appl. Surf. Sci.* **2020**, *518*, 146217.
- [39] Nguyen, T. T.; Lau-Truong, S.; Mammeri, F.; Ammar, S. Star-Shaped $\text{Fe}_{3-x}\text{O}_4$ –Au Core-Shell Nanoparticles: From Synthesis to SERS Application. *Nanomaterials* **2020**, *10*.

Chapter 6

Conclusions and Future Directions

6.1 Conclusions of reported works

The whole of this thesis has aimed to approach SERS-sensing with a new and unconventional design, exploring magnetic materials as primary sensor components for the first time in the field. The IONPs and CFNPs reported here have been thus-far ignored in their contribution to optoelectronic sensing platforms when they have been used, demoted to use as a moveable handle for other main materials of interest.

Both the IONPs and CFNPs synthesized proved to be valuable contributors to surface enhancement when patterned onto Au thin films, where the surface performance was lost if patterned NPs were not present on the surface. This patterned multi-layer is complex in topography, especially for that of the CFNPs with mixed-geometry products, providing both enhancement and adhesion sites for the analytes. The CFNPs with large angular geometries (octahedra of 400+ nm) and a significant proportion of nanospheres (60 nm), along with the largest magnetic coercivity of 1200 Oe, provided the most significant enhancement with SNRs of almost 5 dB.

Scaling the synthesis of these CFNPs began as a practical measure, but resulted

in significant changes of the properties and geometries of the crystals obtained. Scaling the reaction mixture down resulted in a loss of the octahedral shapes, leaving only rounded disks and spheres, and also resulted in superparamagnetic behaviour instead of permanent magnetism with coercivity. The changes in reaction kinetics by scaling altered the nucleation (and subsequent growth) of NPs, resulting in the geometry changes and differences in size distributions/maximum particle sizes. These differences also provide insight into the enhancement mechanism occurring, with implications that the permanent magnetism found in certain scaled products significantly contributes to the overall signal enhancement observed.

To further begin to address this, proof-of-concept tests were performed where a magnet was applied to the patterned surface during spectral acquisition, and this was compared to the same substrate without a magnet applied. The signal intensity increased over 3x in counts with the application of the magnetic field, implying a significant contribution of the magnetic properties of the NPs to the enhancement observed.

6.2 Future directions

There are numerous directions in which this project could continue, with all avenues leading to optimized sensors for various applications. Regarding the work reported thus far in this thesis, further studies into the contributions of NP geometry and magnetism would help in understanding the enhancement mechanism, and therefore the contributions both of these parameters provide.

Specific CFNP geometries (octahedra, disks, spheres) synthesized through methods which allow for more size-control, such as thermal decomposition,¹ would allow for equivalent patterned sensors to be fabricated with single geometries or highly con-

trolled mixtures. By comparing sensors made only with octahedra, disks, spheres, or mixtures, there may be a clear quantifiable enhancement associated with a particular shape or mixing ratio.

In answering these questions regarding the CFNP sensors, the next step is to look at the use of similar ferrites with different 2+ metals, such as NiFe_2O_4 . Such variations of inverse spinel structures will result in changes of magnetic characteristics like remanence, coercivity, and saturation, as changing the 2+ metal will result in new lattice parameters and distances which directly impacts magnetic properties.² In addition to this, swapping the 2+ metal in the synthesis creates potential for other crystal morphologies,³ which will aid in understanding all of these magnetic metal oxides as an enhancing component. Doping ferrites with other metals will also alter aforementioned magnetic properties, which may be more advantageous for use in these optoelectronic sensors.^{4,5} Use of such materials with varied saturation, remanence, and coercivity values in the patterned surface will help in our deeper understanding of the enhancement mechanism, and how performance relates to the various measures of magnetism.

As the reported versions of our sensor work well for PAHs, which are highly symmetric and conjugated molecules, other molecules with similar attributes would likely behave similarly with the current design. Beyond this, the powerful sensing abilities of this surface has potential to be used with a number of other analyte types with some modifications.

As nanoparticles are highly customizable with a large surface area, many things can be added or changed on the surface to create selectivity for particular analytes. By decorating the NP surface with antibodies of various pathogenic viruses or bacteria, this would allow for sensing of antigens in a quick confirmational test from saliva, urine, or blood samples. Similarly, food safety testing could be targeted by sensing

for food-borne pathogens or pesticides by addition of antibodies or polar surface components on the NPs, respectively. This list of future target molecules or sensor versions are non-exhaustive, as the patterned NPs offer the needed versatility and therefore have potential for many future uses.

Bibliography

- [1] Tomar, D.; Jeevanandam, P. Synthesis of cobalt ferrite nanoparticles with different morphologies via thermal decomposition approach and studies on their magnetic properties. *J. Alloys Compd.* **2020**, *843*, 155815.
- [2] Ati, A. A.; Othaman, Z.; Samavati, A. Influence of cobalt on structural and magnetic properties of nickel ferrite nanoparticles. *J. Mol. Struct.* **2013**, *1052*, 177–182.
- [3] Sattar, A. A.; El-Sayed, H. M.; Alsuqia, I. Structural and magnetic properties of $\text{CoFe}_2\text{O}_4/\text{NiFe}_2\text{O}_4$ core/shell nanocomposite prepared by the hydrothermal method. *J. Magn. Magn. Mater.* **2015**, *395*, 89–96.
- [4] Sharifianjazi, F.; Moradi, M.; Parvin, N.; Nemati, A.; Jafari Rad, A.; Sheysi, N.; Abouchenari, A.; Mohammadi, A.; Karbasi, S.; Ahmadi, Z.; Esmaeilkhani, A.; Irani, M.; Pakseresht, A.; Sahmani, S.; Shahedi Asl, M. Magnetic CoFe_2O_4 nanoparticles doped with metal ions: A review. *Ceram. Int.* **2020**, *46*, 18391–18412.
- [5] Tangcharoen, T.; Ruangphanit, A.; Pecharapa, W. Structural and magnetic properties of nanocrystalline zinc-doped metal ferrites (metal=Ni; Mn; Cu) prepared by sol-gel combustion method. *Ceram. Int.* **2013**, *39*, S239–S243.

Appendix A

Supplementary information for Hierarchical magnetic films for high-performing plasmonic sensors, Chapter 2

A.1 Energy-dispersive X-ray (EDX) data

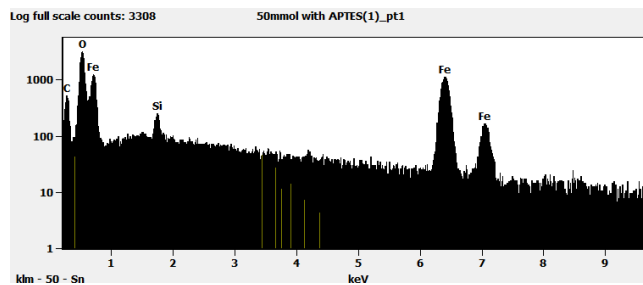


Figure A.1: EDX spectroscopy confirms removal of counter ions and the presence of iron oxides.

A.2 Sizing via Dynamic Light Scattering (DLS)

Sizing of synthesized NPs was attempted numerous times using DLS, but results were inconclusive. The agglomeration of particles meant that diffusion constants did not reflect the individual NP size. Furthermore, the mixed $\text{Fe}_3\text{O}_4/\gamma\text{-Fe}_2\text{O}_3$ crystal made the permittivity value difficult to estimate. Due to these factors, DLS analysis was discontinued in favour of sizing info via SEM imaging.

A.3 Atomic Force Microscopy data

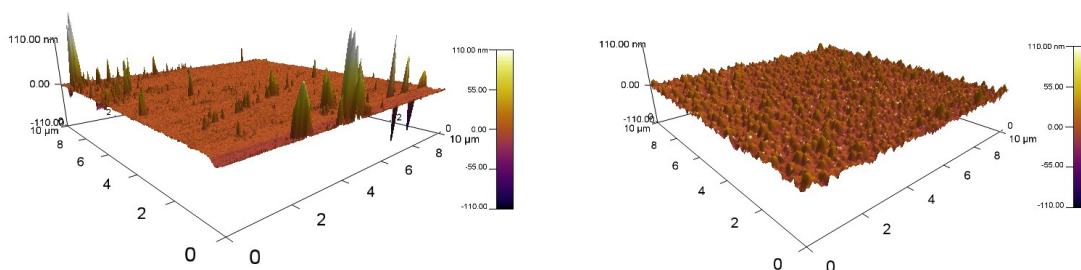


Figure A.2: Atomic force micrographs of the surface of a freshly-deposited ~ 5 nm gold layer (left), created via magnetron sputtering, and a gold layer after annealing (right). The surface is initially largely smooth (the large spikes are noise associated with Au deposits 50-100 nm in height). After annealing, in preparation for use in the sensor design, the sputtered gold layer has become roughened.

A.4 Supplementary Raman data

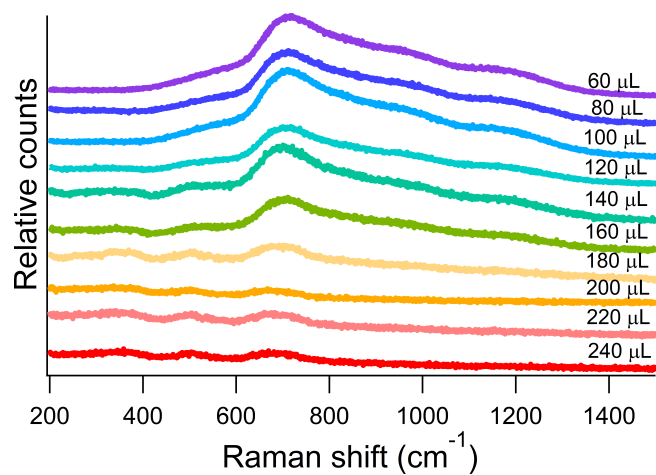


Figure A.3: Spectra acquired after each successive nanoparticle layer addition of 20 μL , showing fluorescence being quenched with sufficient layers.

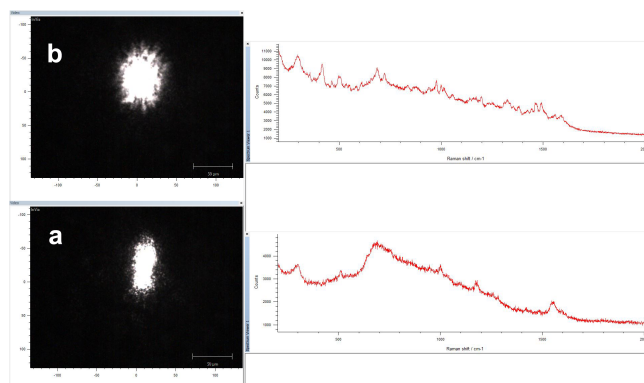


Figure A.4: Spectra acquired when focused within the nanoparticle multi-layer (top) allows for excellent enhancement of the analyte, while focusing on the reflective gold surface (bottom) largely results in fluorescence with very few enhancement peaks.

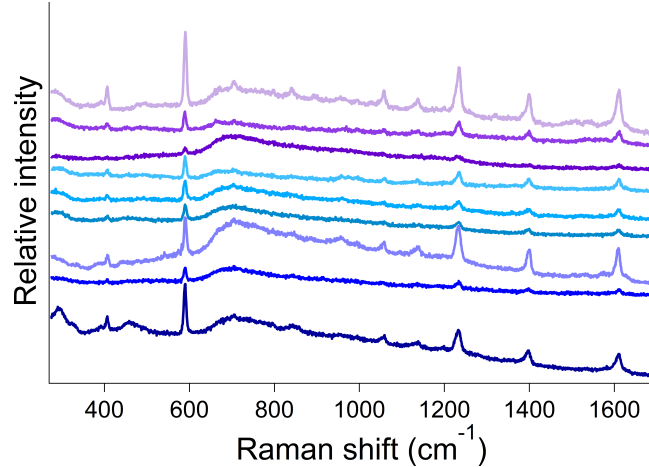


Figure A.5: Spectra acquired from different surface locations on patterned substrates show reproducible Raman signals and intensities from the exposed analyte

A.5 Signal-to-Noise (SNR) Calculations

SNR calculations were performed to assess the signal of plasmonically-enhanced Raman peaks compared to the baseline noise of the same spectrum.

To calculate this ratio, a section of the baseline, comprising of around 500 data points, was compared to peaks at 808 cm^{-1} and 906 cm^{-1} .

First a simple, zeroth order baseline subtraction was performed, because the spectra often are offset from zero (the baseline and all peaks have counts values well above zero). This was done by taking the mean of the baseline values and subtracting that from each point in the spectrum. This offsets the the spectrum so that the baseline consists of noise around zero counts. The peaks are of course likewise lowered from the initial offset.

The average baseline value was zero, with the noise consisting of positive and negative values. Baseline values were each squared, then averaged, to provide the “noise” level. The intensities at the peaks (already offset as indicated above) were also squared, and this provided the “signal”.

Each signal value was divided by the noise value (average squared baseline) to

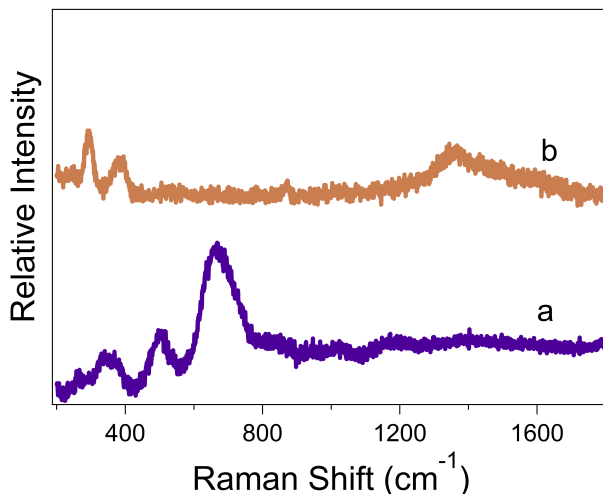


Figure A.6: The spectrum in (a) shows the Raman modes for ferrimagnetic $\text{Fe}_3\text{O}_4/\gamma\text{-Fe}_2\text{O}_3$, as per a freshly patterned substrate. Spectrum (b) shows the same surface after 4 years of slow oxidizing under ambient storage conditions, after being freshly exposed to analyte. The iron oxide form has changed to an oxy-hydroxide, $\gamma\text{-FeO(OH)}$, and these are the only modes visible in the spectrum. No analyte peaks are detectable.

obtain the ratio of SNR. The logarithm of this value provides the SNR in units of dB.

For example, for the peak at 808 cm^{-1} the SNR would be calculated as follows:

$$\text{SNR} = \log \left(\frac{I_{808}^2}{\sum(I_{\text{baseline}}^2)/N} \right) \quad (\text{A.1})$$

where I_{808} is the intensity in counts at 808 cm^{-1} after baseline subtraction, I_{baseline} are the intensity values of the baseline after baseline subtraction, and N is the number of points in the baseline.

A.6 Produced Water sampling

Before sampling, a 4 L glass bottle was cleaned using soap and water and then rinsed with ultrapure water. The bottle was then soaked in a solution of 0.81 M KOH in 80/20 isopropyl alcohol/ultrapure water, and then rinsed with ethanol and ultrapure

water. The bottle was then soaked in 6 M HCl followed by a thorough rinse with ultrapure water.

Produced water (PW) samples were taken from a holding tank aboard an oil platform off the shore of Newfoundland. In short, 4 L of produced water was collected into a cleaned glass bottle. After sampling was completed, the bottle and its contents were allowed to cool to room temperature, and then were placed in a beverage cooler with ice packs to keep the water cool. The cooler and its contents were transported via helicopter to the Cougar Helicopter terminal of St. John's International Airport where the research team collected the water samples.

To inhibit bacterial growth and/or bacterial degradation of the water samples, upon return to the laboratory at Memorial University, the pH of the produced water was adjusted to approximately 2 using concentrated H_2SO_4 . This sample was then exposed to the substrate for SERS measurements.

A.7 Gas Chromatography-Mass Spectrometry (GC-MS) procedure

Produced water samples were analyzed using Gas Chromatography-Mass Spectrometry (GC-MS) for qualitative analysis of its components, as well as quantitatively analyzed to determine the Total Organic Carbon of the water. These results were then used to verify the presence of PAHs noted in the Raman Spectroscopy data.

A.7.1 Organic Extraction of Produced Water

All glassware used in the extraction and analysis of produced water samples were cleaned in the same manner as the glass bottle used to collect the water samples, as outlined in Section A.6.

A.7.2 Dispersive Liquid-Liquid Microextraction (DLLME)

A 10 mL aliquot of Produced water was placed into a 50 mL centrifuge tube. A 1.5 mL volume of 2:1 ethanol/chloroform was rapidly injected into the produced water using a Hamilton syringe, resulting in a cloudy mixture being formed. The tube was then spun in a centrifuge at 2500 rpm for 3 minutes. After centrifugation, 2 distinct layers had formed in the tube. The organic layer was removed using a syringe, and concentrated under a constant flow of filtered, dried air. Before GC-MS analysis, the concentrated extract was re-diluted with 1.5 mL HPLC grade-chloroform, filtered through #5 filter paper, and transferred to a GC-MS vial for analysis.

A.7.3 GC-MS Analysis

Gas Chromatography-Mass Spectrometry was performed with a quadrupole mass spectrometer and an Agilent 6890N GC system using a 30 m DB-5 capillary column with Helium carrier gas. Samples were taken using an autosampler with split/split-less injections of 1.0 μL using an automatic injector temperature set to 285 °C. The GC oven was programmed from 60 °C to 300 °C (20 °C/minute), and then held at 300 °C for 10 minutes. Peaks were identified using the National Institute of Standards and Technology (NIST) mass spectral database. For quantification of components, external standards were used to create a calibration curve.

A.8 GCMS results

Table A.1 presents a breakdown of components of produced water detected by GC-MS.

Table A.1: GC-MS data for produced water, sampled from an offshore oil platform.

| retention time (min) | peak area | NIST database results | database probability (%) | concentration (ppm) |
|-------------------------|-----------|---|-----------------------------|------------------------|
| 4.308 | 144744 | hexachloroethane | 53.3 | 0.2656* |
| 4.674 | 2187728 | cyclohexanecarboxylic acid | 71.3 | 0.7763 |
| 5.120 | 5253321 | 4-methylcyclohexanecarboxylic acid | 65.0 | 1.5427 |
| 5.325 | 193337 | 10-undecenoic acid, methyl ester | 66.4 | 0.2777 |
| | | cyclohexanebutanoic acid | 65.3 | |
| 5.417 | 215660 | undecylenic acid | 68.9 | 0.2833 |
| 5.474 | 492258 | 1,5,5-trimethyl-6-methylenecyclohexene | 72.1 | 0.3524 |
| 5.817 | 3678663 | 1,5,5-trimethyl-6-methylenecyclohexene | 69.4 | 1.1490 |
| 5.954 | 958694 | 2-ethenyl-1,3,3-trimethylcyclohexene | 73.2 | 0.4690 |
| 6.103 | 533199 | 2-ethylidene-6-methyl-3,5-heptadienal | 71.5 | 0.3627 |
| | | 2-(2-butynyl)cyclohexanone | 69.7 | |
| 6.331 | 734787 | 4-(2,5-dihydro-3-methoxyphenyl)butylamide | 73.4 | 0.4131 |
| 6.451 | 794754 | 2-ethylidene-6-methyl-3,5-heptadienal | 68.0 | 0.4281 |
| 6.623 | 1222636 | 2,6,10-triethyltetradecane | 72.9 | 0.5350 |

* From solvent † No structure ‡Based off of standards

Continued on next page

Table A.1 – continued from previous page

| retention time (min) | peak area | NIST database results | database probability (%) | concentration (ppm) |
|---|----------------|---|-----------------------------|------------------------|
| 6.703 | 1442310 | 2,4,7,9-tetramethyl-5-decyn-4,7-diol | 73.5 | 0.5899 |
| 6.794 | 402810 | 1,3-dimethylnaphthalene | 59.8 | 0.3301 |
| 6.880 | 641793 | 1,3-dimethylnaphthalene | 70.1 | 0.3898 |
| | | 1,7-dimethylnaphthalene | 70.0 | |
| 7.034 | 1257407 | 6-(ethylamino)-1,3,5-triazine-2,4-(1H,3H)-dione | 63.8 | 0.5437 |
| | | 1,3-dimethylnaphthalene | 60.6 | |
| 7.269 | 2457807 | 2,6,10-trimethyltetradecane | 80.6 | 0.8438 |
| | | Pentadecane | 79.2 | |
| 7.434 | 257854 | 6-(1,3-dimethyl-buta-1,3-dienyl)-1,5,5-trimethyl-7-oxa- bicyclo[4.1.0]hept-2-ene | 67.1 | 0.2938 |
| | | chlorodehydromethyltestosterone | 66.4 | |
| 7.556 | 876434 | cis-3-octyloxiraneoctanoic acid | 63.4 | 0.4485 |
| | | 4-(3-methyl-2-butenyl)-1H-indole | 61.4 | |
| * From solvent † No structure ‡Based off of standards | | | Continued on next page | |

Table A.1 – continued from previous page

| retention time (min) | peak area | NIST database results | database probability (%) | concentration (ppm) |
|-------------------------|-----------|---|-----------------------------|------------------------|
| 7.811 | 731875 | 6-(1,3-dimethyl-buta-1,3-dienyl)-1,5,5-trimethyl-7-oxa- bicyclo[4.1.0]hept-2-ene | 66.7 | 0.4123 |
| | | chlorodehydromethyltestosterone | 65.3 | |
| 7.866 | 2764150 | 2,6,10-trimethyltetradecane | 77.9 | 0.9204 |
| | | Hexadecane | 77.8 | |
| 7.949 | 993298 | 5-Hydroxy-8,8-dimethyl-3,3a,4,5,6,7,8,8b-octahydroindeno[1,2- b]furan-2-one | 63.7 | 0.4777 [†] |
| 8.160 | 1520041 | 2-Myristynoyl pantetheine | 68.3 | 0.6094 |
| | | 7-Methyl-Z-tetradecen-1-ol acetate | 68.0 | |
| | | 2-hexadecanol | 67.1 | |
| 8.263 | 607013 | methyl-11,14-eicosadienoate | 69.3 | 0.3811 |
| 8.389 | 303197 | Retinol | 69.6 | 0.3052 |
| | | 1,1,4,6-tetramethylperhydrocyclopropa[e]azulene-4,5,6-triol | 69.3 | |

* From solvent † No structure ‡Based off of standards

Continued on next page

Table A.1 – continued from previous page

| retention time (min) | peak area | NIST database results | database probability (%) | concentration (ppm) |
|-------------------------|----------------|--|-----------------------------|---------------------------|
| 8.469 | 6108405 | 2,6,10-trimethyltetradecane | 86.0 | 1.7565 |
| | | Heptadecane | 78.7 | |
| 8.863 | 917329 | 17-acetoxy-3-methoxy-4,4-dimethyl-8,14-Seco-3,19- epoxyandrostane-8,14-dione | 66.0 | 0.4587 [†] |
| | | 2-methyl-cis-7,8-epoxynonadecane | 65.6 | |
| 8.972 | 357997 | Ursodeoxycholic acid | 70.8 | 0.3189 |
| 9.023 | 13769694 | N-butylbenzenesulfonamide | 70.2 | 3.6718 |
| 9.126 | 1663616 | Phenanthrene | | 0.6453[‡] |
| 9.246 | 1207876 | 10-Acetoxy-2-hydroxy-1,2,6a,6b,9,9,12a-heptamethyl- 1,3,4,5,6,6a,6b,7,8,8a,9,10,11,12,12a,12b,13,14b-octadecahydro- 2H-picene-4a-carboxylic acid, methyl ester | 70.3 | 0.5313 |
| 9.360 | 245962 | 10-Acetoxy-2-hydroxy-1,2,6a,6b,9,9,12a-heptamethyl- 1,3,4,5,6,6a,6b,7,8,8a,9,10,11,12,12a,12b,13,14b-octadecahydro- 2H-picene-4a-carboxylic acid, methyl ester | 70.2 | 0.2909 |

* From solvent † No structure ‡Based off of standards

Continued on next page

Table A.1 – continued from previous page

| retention time (min) | peak area | NIST database results | database probability (%) | concentration (ppm) |
|---|-----------|--|-----------------------------|------------------------|
| 9.418 | 540948 | 17-acetoxy-3-methoxy-4,4-dimethyl-8,14-Seco-3,19- epoxyandrostane-8,14-dione | 67.8 | |
| | | 2-bromooctadecanal | 66.5 | 0.2294 |
| 9.492 | 469204 | 10-Acetoxy-2-hydroxy-1,2,6a,6b,9,9,12a-heptamethyl- 1,3,4,5,6,6a,6b,7,8,8a,9,10,11,12,12a,12b,13,14b-octadecahydro- 2H-picene-4a-carboxylic acid, methyl ester | 70.2 | 0.3467 |
| 9.755 | 4681389 | 10-Acetoxy-2-hydroxy-1,2,6a,6b,9,9,12a-heptamethyl- 1,3,4,5,6,6a,6b,7,8,8a,9,10,11,12,12a,12b,13,14b-octadecahydro- 2H-picene-4a-carboxylic acid, methyl ester | 69.5 | 1.3997 |
| | | methyl-11,14-eicosadienoate | 66.1 | |
| 10.018 | *369181 | 1-Heptatriacotanol | 72.2 | 0.3217 |
| | | Oleic acid, eicosyl ester | 70.8 | |
| 10.058 | 4871673 | 3-ethyl-5-(2-ethylbutyl)octadecane | 73.8 | 1.4473 |
| | | 9-hexylheptadecane | 72.8 | |
| * From solvent † No structure ‡Based off of standards | | | Continued on next page | |

Table A.1 – continued from previous page

| retention time (min) | peak area | NIST database results | database probability (%) | concentration (ppm) |
|---|-----------|--|-----------------------------|------------------------|
| 10.246 | 3649907 | dihydro-3-octadecyl-2,5-furandione | 71.2 | 1.1418 |
| 10.326 | 562805 | 1-Heptatriacontanol | 71.7 | 0.3701 |
| 10.406 | 1708469 | 10-Acetoxy-2-hydroxy-1,2,6a,6b,9,9,12a-heptamethyl- 1,3,4,5,6,6a,6b,7,8,8a,9,10,11,12,12a,12b,13,14b-octadecahydro- 2H-picene-4a-carboxylic acid, methyl ester | 69.4 | 0.6565 |
| | | Dihydroxanthin | 69.2 | |
| 10.538 | 3818562 | 3-ethyl-5-(2-ethylbutyl)octadecane | 73.9 | 1.1840 |
| | | 17-pentatriacontene | 73.8 | |
| 10.715 | 1701717 | Oleic acid, eicosyl ester | 72.5 | 0.6548 |
| 10.995 | 3104254 | 17-pentatriacontene | 75.9 | 1.0054 |
| 11.161 | 2060196 | Oleic acid, eicosyl ester | 72.6 | 0.7444 |
| 11.441 | 5463042 | 3-ethyl-5-(2-ethylbutyl)octadecane | 75.4 | 1.5951 |
| * From solvent † No structure ‡Based off of standards | | | Continued on next page | |

Table A.1 – continued from previous page

| retention time (min) | peak area | NIST database results | database probability (%) | concentration (ppm) |
|-------------------------|-----------|--|-----------------------------|------------------------|
| 11.595 | 1701978 | Dodecanoic acid, 1a,2,5,5a,6,9,10,10a-octahydro-5a-hydroxy-4-(hydroxymethyl)-1,1,7,9-tetramethyl-6,11-dioxo-1H-2,8a-methanocyclopenta[a]cyclopropa[e]cyclodecen-5-yl ester, [1aR-(1a,2,5,5a,8a,9,10a)]- | 72.2 | 0.6549 |
| 11.732 | 4041227 | Oleic acid, eicosyl ester | 72.4 | 1.2397 |
| 11.864 | 4134897 | 3-ethyl-5-(2-ethylbutyl)octadecane | 77.9 | 1.2631 |
| 11.955 | 2250541 | Butanoic acid, 4-chloro-, 1,1a,1b,4,4a,5,7a,7b,8,9-decahydro-4a,7b-dihydroxy-3-(hydroxymethyl)-1,1,6,8-tetramethyl-5-oxo-9aH-cyclopropa[3,4]benz[1,2-e]azulene-9,9a-diyl ester, [1aR-(1a,1b,4a,7a,7b,8,9,9a)]- | 71.5 | 0.7920 |
| 12.092 | 228346 | 3-acetoxy-7,8-epoxylanostan | 74.9 | 0.2865 |
| 12.275 | 3781510 | 3-ethyl-5-(2-ethylbutyl)octadecane | 75.2 | 1.1747 |
| | | 17-pentatriacontene | 74.4 | |
| 12.412 | 620435 | 3-acetoxy-7,8-epoxylanostan-11-ol | 75.0 | 0.3845 |

* From solvent † No structure ‡Based off of standards

Continued on next page

Table A.1 – continued from previous page

| retention time (min) | peak area | NIST database results | database probability (%) | concentration (ppm) |
|-------------------------|-----------|------------------------------------|-----------------------------|------------------------|
| 12.664 | 3031038 | 3-ethyl-5-(2-ethylbutyl)octadecane | 74.1 | 0.9871 |
| 12.790 | 1077356 | 3-acetoxy-7,8-epoxy lanostan-11-ol | 76.3 | 0.4987 |
| 13.047 | 2861076 | 3-acetoxy-7,8-epoxy lanostan-11-ol | 72.3 | 0.9446 |
| 13.167 | 506604 | 3-acetoxy-7,8-epoxy lanostan-11-ol | 75.7 | 0.3560 |
| 13.289 | 105228 | 3-acetoxy-7,8-epoxy lanostan-11-ol | 76.2 | 0.2557 |
| 13.447 | 2909408 | 3-acetoxy-7,8-epoxy lanostan-11-ol | 74.6 | 0.9567 |
| | | | TOTAL | 41.9650 |
| | | | PAH Total | 1.9089 |

* From solvent † No structure ‡Based off of standards

Appendix B

MPTMS Capping of IONPs, experiments related to Chapter 2

When preparing capped IONPs, I tried two capping agents: APTES and (3-mercaptopropyl)-trimethoxysilane (MPTMS). The MPTMS-capped nanoparticles showed many peaks beyond the test analyte, and these peaks changed upon changing laser power. I concluded that the capping agent itself was reacting with the surface in some way, and additionally perhaps with moisture/air. Therefore this capping agent was discontinued in development of the sensors described in Chapter 2.

MPTMS capping was performed exactly as described in section 2.2.2, using 100 μL of MPTMS in place of APTES.

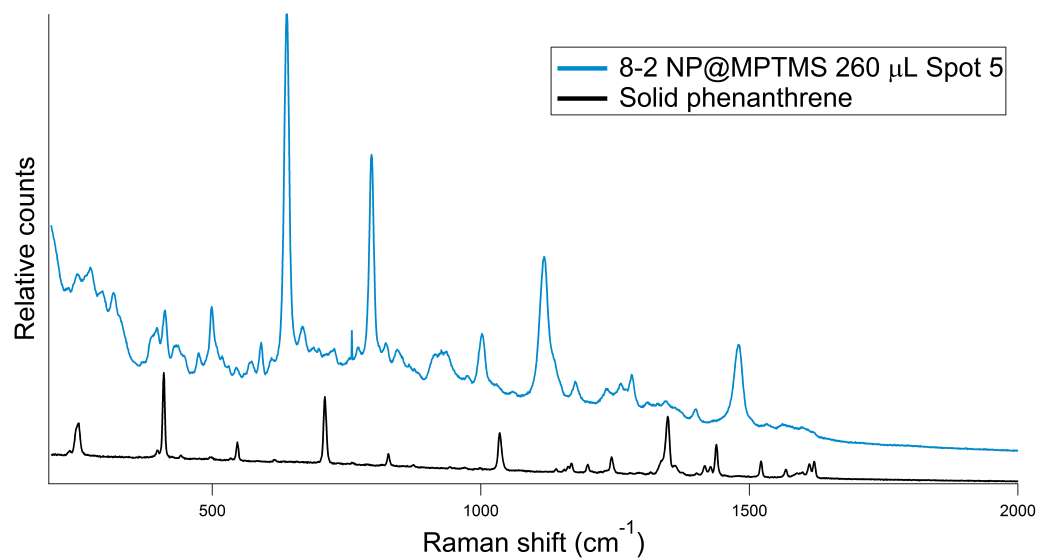


Figure B.1: Substrate 8-2 made with patterned IONP@MPTMS exhibits significant enhancement of 1 ppm phenanthrene.

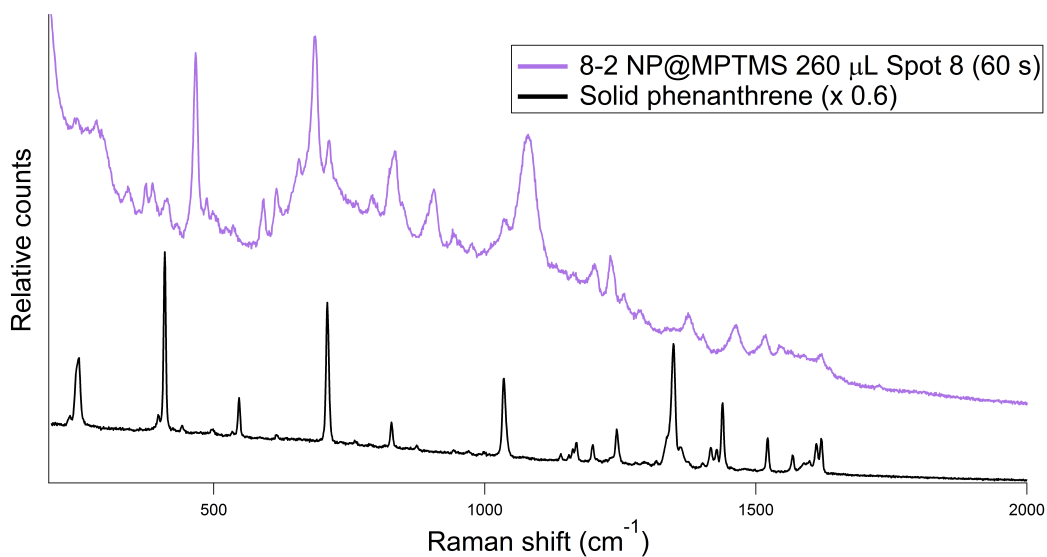


Figure B.2: Substrate 8-2 (different sensing spot from above figure) again displaying significant enhancement of 1 ppm phenanthrene.

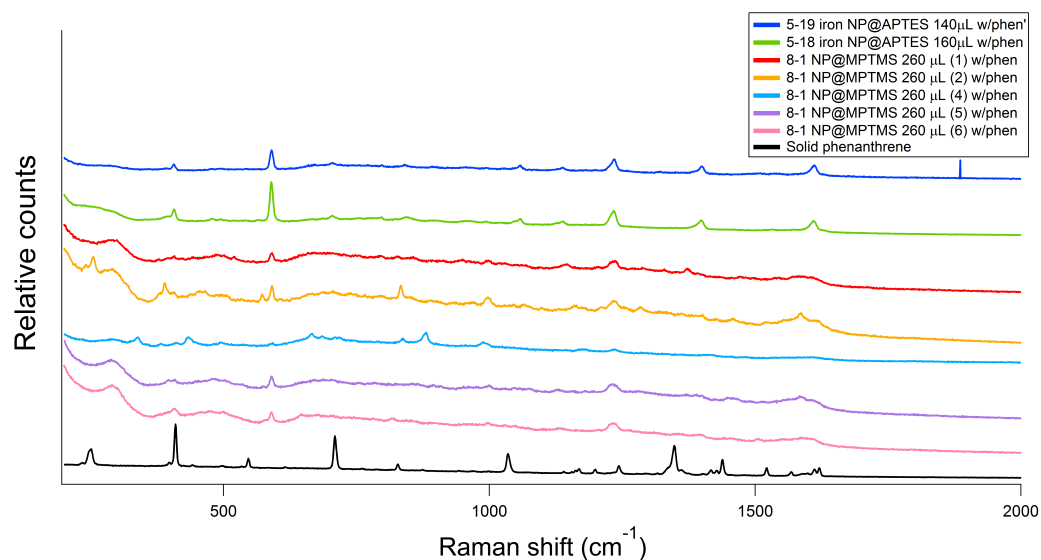


Figure B.3: Comparison of sensors made with MPTMS-coated IONPs compared to the APTES-coated equivalent. Major peaks of phenanthrene on the surfaces remain consistent, exhibiting strong enhancement throughout.

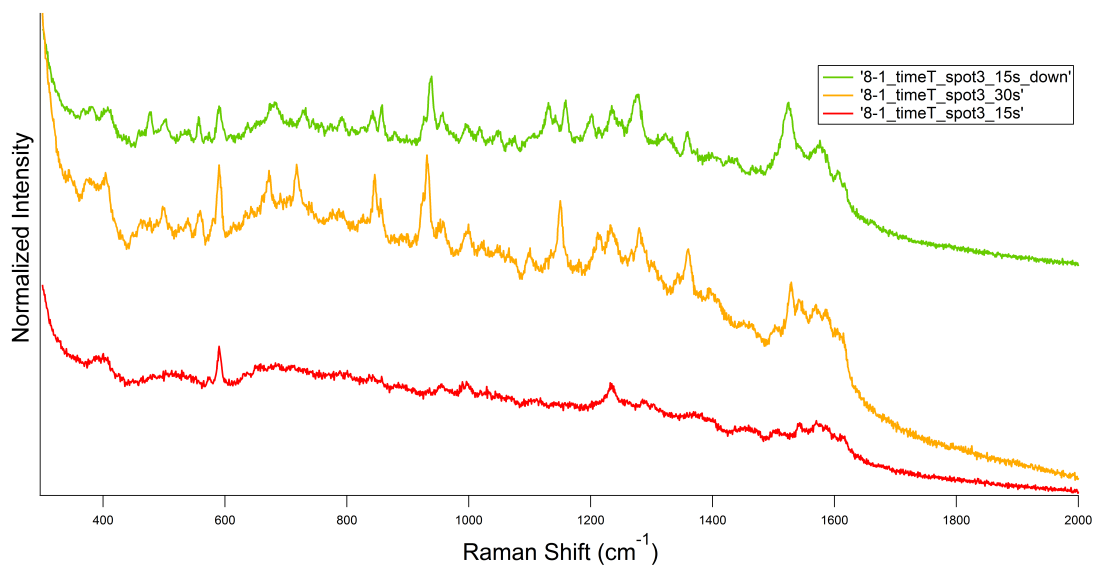


Figure B.4: Sequential laser exposures (15 second acquisition, followed by 30 s and 15 s again) results in changes of the IONP@MPTMS sensing surface, exposed to 1 ppm phenanthrene.

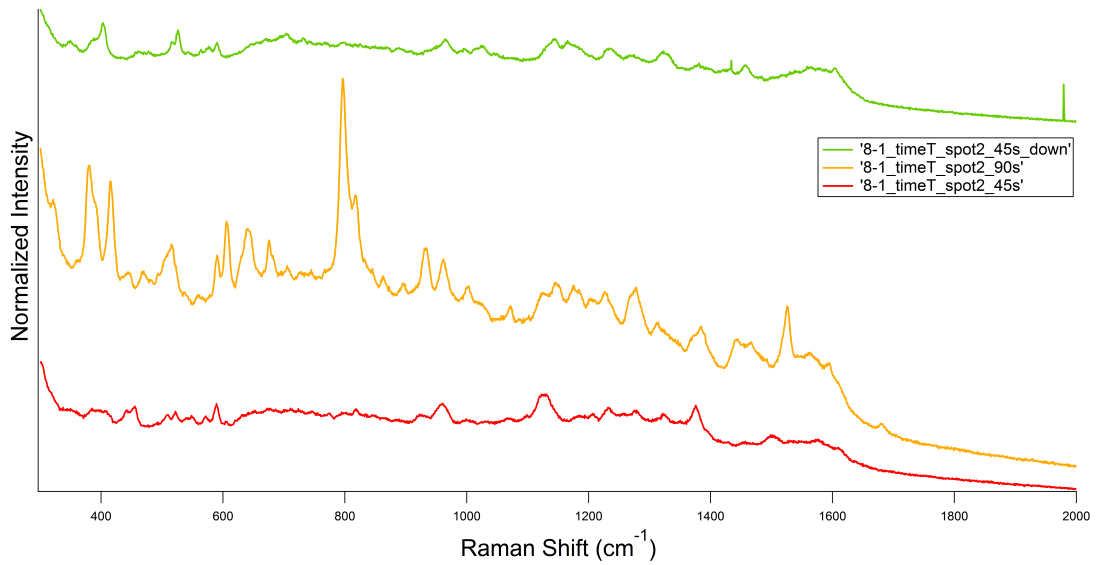


Figure B.5: Sequential laser exposures (45 second acquisition, followed by 90 s and 45 s again) results in changes of the IONP@MPTMS sensing surface, exposed to 1 ppm phenanthrene.

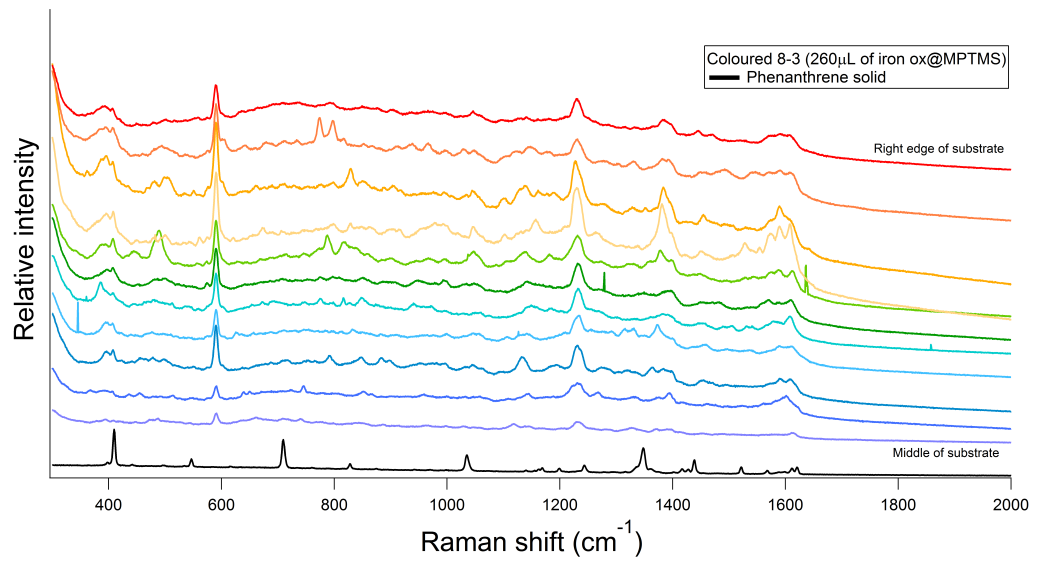


Figure B.6: Scanning across the patterned surface (middle to edge) shows comparable enhancement at all locations.

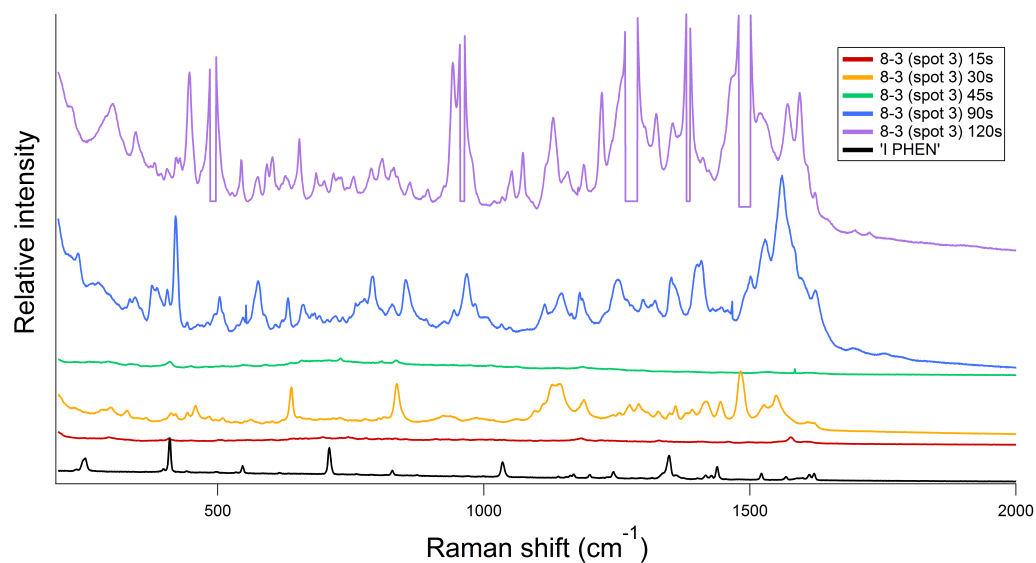


Figure B.7: Increasing laser exposure time before spectrum acquisition results in increasing amounts of activity on the surface, seemingly as a result of laser power. The square gaps in the 120 s spectrum (purple, top) are due to photon saturation of the detector.

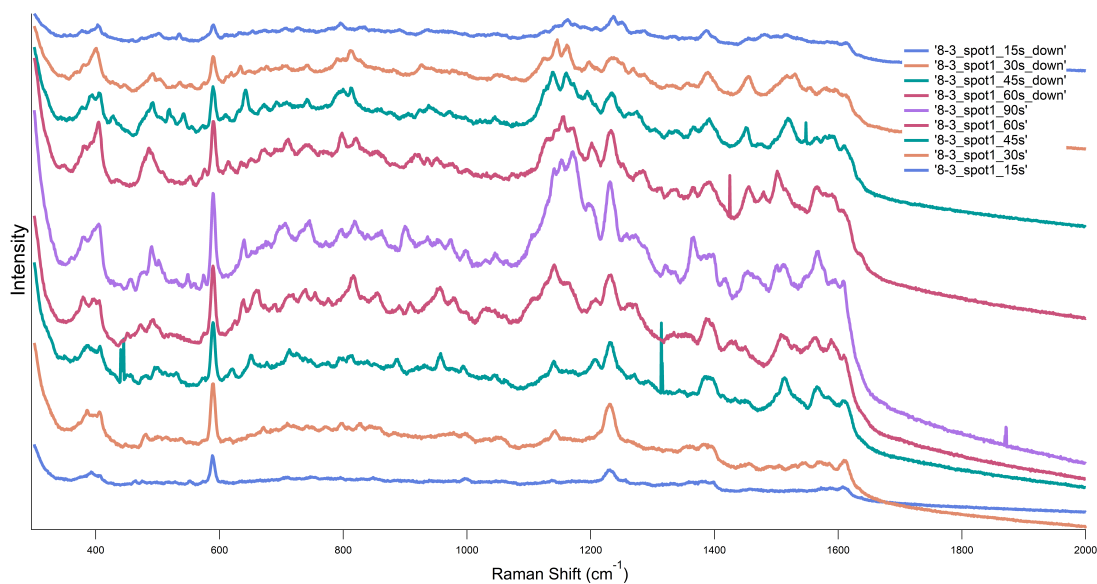


Figure B.8: Increasing the laser exposure time results in irreversible changes of the surface, exposed to 1 ppm of phenanthrene.

Appendix C

Supplementary information for Powerful electromagnetic field enhancement via complex cobalt ferrite surfaces for plasmonic sensing, Chapter 4

C.1 Archival use and Reusability

Archivable samples are important to meet some regulatory guidelines and are often desired by users. These films show excellent longevity on their own, and they also maintain the sample in its original state for at least 9 months without special storage conditions (see Figure C.1).

Washing procedures were performed on the substrate surface to assess their potential reusability. Previously exposed samples were re-tested after ≈ 1 year under

ambient conditions, and analyte peaks were still prevalent after this time.

Ethanol was employed as the first washing solvent, first via passive beaker loading, where analyte peaks were still present after this wash. An active rinsing was then tried, where the substrate was held perpendicular as ethanol was sprayed in quick intervals onto the surface (1 mL per rinse). After this active washing, Raman data collected indicated these washing steps were not successful for this analyte.

To address the solubility issues of phenanthrene in ethanol, these procedures were repeated exactly with toluene. The passive beaker load method was again unsuccessful, but active rinsing with toluene in intervals succeeded in removal of all analyte on the surface.

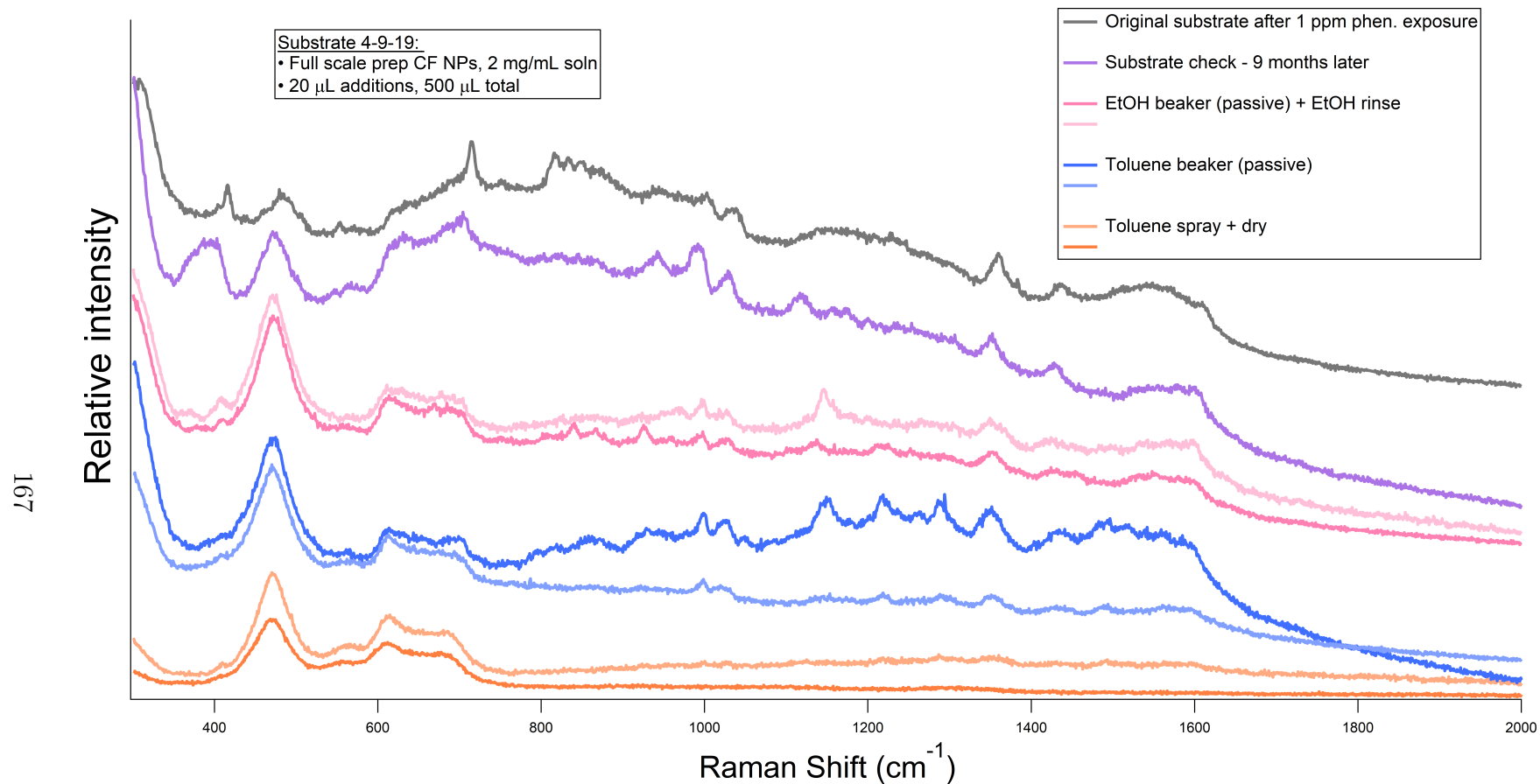


Figure C.1: Raman spectra were collected from a 1-year stored substrate, comparing with the original spectrum acquired from the same surface when freshly exposed (top two lines). As there was comparable enhancement in both, this indicates that the substrate can be relied on for long periods of time for archival usage. Regarding potential reusability, ethanol and toluene were used as washing solvents to remove all presence of analyte. While all use of ethanol was unsuccessful, toluene in an active spray onto the surface successfully removed all analyte, making the substrate reusable for at least one cycle.

C.2 Experimental Details

C.2.1 Materials

Cobalt (II) chloride hexahydrate ($\geq 99\%$) and iron (III) chloride hexahydrate ($\geq 99\%$) were purchased from Sigma Aldrich (Oakville, Ontario, Canada). Concentrated hydrochloric acid and sulfuric acid were purchased from Fisher Scientific (Ottawa, Ontario, Canada). Concentrated ammonium hydroxide solution was purchased from ACP Chemicals (Montreal, Quebec, Canada). Ar (ultra-high purity) was purchased from Praxair Canada. Distilled and filtered nanopure water was obtained from a Barnstead 18.2 M Ω ·cm system. All chemicals were used without further purification.

C.2.2 Nanoparticle Synthesis

Magnetic NPs were prepared via the Massart¹ precipitation method. NPs were created by mixing 37.8 g of FeCl₃·6H₂O and 16.6 g of CoCl₂·6H₂O into 100 mL of nanopure water at around 80 °C under constant stirring. The salts dissolved readily, resulting in a clear dark pink solution, after which concentrated NH₄OH was added slowly (around 0.5 mL/sec) to the mixture until the reaction reached a pH of 11. Upon addition of base, brown solids immediately began to form. The mixture was heated and stirred for around 1.5 hrs, after which it was removed from heat and, once cooled to room temperature, neutralized with dilute HCl (1 M).

After reaching a neutral pH, the NPs were washed in triplicate with nanopure water to remove all counter ions, with centrifuging and decanting of the supernatant between each wash.

The solid was then dried overnight in an oven at 80 °C. Then the solids were finely ground using a mortar and pestle and annealed for 9 hours at 600 °C, resulting in the final magnetic product.

C.2.3 Characterization

Powder X-ray diffraction (pXRD) data were collected from 20° to 80° 2θ using a Rigaku Ultima IV X-Ray diffractometer with a Cu-K α source. **Scanning electron microscopy (SEM)**, used for size and shape analysis of the products, was performed on a JEOL JSM-7100F Scanning Electron Microscope, where particle elemental analysis was also performed at the same time with **energy-dispersive X-ray spectroscopy (EDX)**. Samples were prepared for electron beam analysis by carbon coating a 2 nm layer, and probe voltages were kept at 15 kV during imaging with a working distance of 12 mm. **Raman spectroscopy** of all products and substrates were performed using a Renishaw InVia confocal Raman system equipped with an 830 nm diode laser source, also with a Leica DM2700 microscope, the camera of which also provided the optical micrographs. All Raman spectra were collected at 3.0 ± 0.3 mW (1% power). To study magnetic properties, **Vibrating sample magnetometry (VSM)** was performed using a MicroSense EZ vibrating sample magnetometer (VSM), and data was collected from ± 20 kOe at around 25 °C.

C.2.4 Substrate Fabrication Method

For the substrate base, glass microscope slides (Technologist ChoiceTM, 75 mm \times 26 mm \times 1 mm) were cut into three equal pieces using a diamond scribe (SPI Supplies). These slides were then acid-washed, first sitting in a warmed (40 °C) concentrated HCl bath for 5-10 mins and then in a concentrated H₂SO₄ bath at the same temperature for another 5-10 mins. Nanopure water was used to rinse in between, and ethanol was used to do final rinsing. The cleaned substrates were then submerged in ethanol until use.

The washed slides were then rinsed with ethanol and dried with compressed air

to prepare for addition of the plasmonic layer. The substrates were arranged in a single layer on the stage of a Quorum Technologies K550X Sputter Coater fit with a gold target (Soquelec model number K550X Au target: 60 mm diameter Au disk, 0.1 mm thickness), where argon was then pumped through. The slides were coated for 1 minute at 20 mA, leading to a deposited gold thickness of around 5 nm. After this, the gold slides were placed in a Thermo Scientific Lindberg Blue M tube furnace and annealed at 300 °C for 2 hours.

The coated substrates were then placed on a stack of disk magnets (neodymium alloy, stack of three disks, each with dimensions 18 mm × 3 mm), and successive layers of the NPs in solution were added. NPs were sonicated (Fisher Scientific FS20) for about 30 minutes prior to use, to ensure the particles were well dispersed. Layers of a 2 mg/mL NP suspension were added 20 μ L at a time, allowing the solvent to evaporate in between each addition. This was repeated until cobalt ferrite peaks became dominant over glass fluorescence.

C.2.5 Substrate Testing Method

Once fabricated, the finished substrate was exposed to analyte solution. Substrates were submerged in a beaker containing the analyte and allowed to sit for 30 minutes, after which they were removed and allowed to dry. The substrate was then immediately analyzed via Raman spectroscopy.

C.2.6 Area of Surface Measured via Raman Spectroscopy

Bibliography

- [1] Massart, R. Preparation of Aqueous Magnetic Liquids in Alkaline and Acidic Media. *IEEE Trans. Magn.* **1981**, *17*, 1247–1248.

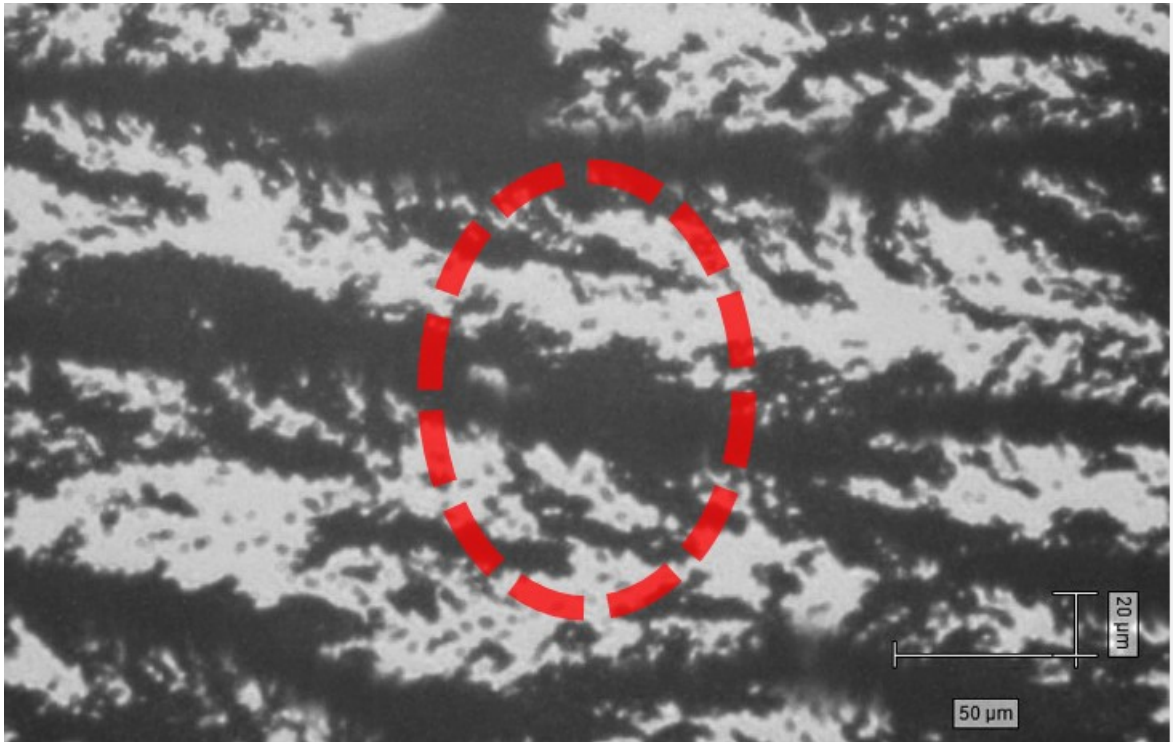


Figure C.2: Overlay of laser spot size (red dashed oval) on an optical micrograph of the SERS surface, showing the area encompassed when collecting Raman data.